

Title page:

**Investigation of Bulk Defects in *p*-type
Silicon Wafers and Solar Cells**

Saman Jafari

A thesis in fulfillment of the requirements for the degree of
Doctor of Philosophy



School of Photovoltaic and Renewable Energy Engineering
Faculty of Engineering

January 2022

Wishing is not enough, one day is too short
Action and patience, you need them both

Abstract

While solar energy is already one of the cheapest methods for generating electricity, further improvements to solar cell efficiencies are needed to continue reducing the cost of photovoltaic (PV)-based energy along its current learning curve. Further improvements to the bulk lifetime of silicon wafers and cells are necessary, to keep up with rapid developments in the remaining regions of the solar cells i.e., surfaces and contacts. To achieve this, better identification of bulk defects in the dominant *p*-type silicon material is required. In this thesis, various characterization methods are developed and utilized to study two types of *p*-type bulk defects: recombination-active defects and minority carrier traps (traps).

Photoconductance decay (PCD) measurements are used to investigate the boron-oxygen (BO)-related traps in boron (B)-doped Czochralski (Cz) silicon wafers. It is found that these traps are acting as the precursor of BO-related defects which cause light-induced degradation (LID) in B-doped Cz wafers. For the first time, the PCD measurement method is introduced as a potential method to investigate defects in their non-recombination-active form. The results from doping- and temperature-dependent PCD measurements suggest that the investigated BO-related traps have more than one energy level.

The PCD method is also used to investigate traps in B-doped multicrystalline silicon wafers. It is shown that a set of slow traps are present in these wafers. These traps are temporarily removed after firing and they are re-generated by keeping the samples in the dark for several days or by dark annealing (DA) them for a short time. Further investigation of these traps shows that they are annihilated with laser annealing, and likely irreversible. However, no connection between removal of these traps and generation of light- and elevated temperature-induced degradation (LeTID)-related defects is observed. A deeper investigation of the observed traps suggests that grain boundaries are likely to be the cause.

Newly emergent gallium (Ga)- as well as indium (In)-doped Cz silicon wafers are investigated. First, the presence of LID in these wafers is studied, suggesting that degradation happens at two stages for Ga-doped wafers and in a single stage for In-doped wafers. Moreover, defect annihilation with DA happens in two stages for both materials. The defect formation and annihilation activation energies for both Ga- and In-doped

wafers are measured. The parameters of LID-related defects in Ga-doped wafers are extracted, suggesting that LeTID-related defects might be the source of degradation in this material. Traps in Ga-doped wafers are also studied. It is shown that these traps are removed with light soaking and re-generated with DA. However, they are not related to the observed LID in Ga-doped wafers.

A new method for the extraction of defect parameters from completed and fully metalized solar cells is developed based on temperature-dependent Suns- V_{oc} measurements, Suns- $V_{oc}(T)$. This Suns- $V_{oc}(T)$ method is validated by extracting the parameters of the well-known BO-related defects and comparing them to defect parameters extracted from lifetime structure and values published in the literature. The new Suns- $V_{oc}(T)$ method is then used to extract the parameters of the defect causing LID in Ga-doped cells and the results are compared with the reported results in prior chapters and literature. A sensitivity analysis is performed for the Suns- $V_{oc}(T)$ method, suggesting that the limited temperature range of the measurement system does not cause a systematic error in the extracted parameters of the two investigated defects.

Acknowledgment

First and foremost, I want to thank my supervisor, Ziv Hameiri. It was a great and unique experience to work under your supervision and learn from you firsthand. Thank you for your patience when I was trying to find my way at the start of my PhD, thank you for believing in me when I had doubts, and for always asking the right questions. Going into more details would need tens of pages, but in short, thanks Boss for teaching me about science and life.

A big thank you to my joint supervisor, Thorsten Trupke, and my co-supervisor, Fiacre Rougieux. I am very grateful to you for sharing your knowledge and time with me. Your feedback has always helped me to look at my projects from a new angle. I would also like to thank my unofficial supervisor, Yan Zhu. Your guidance and comments were always spot on and had a huge impact on improving the quality of my research.

I want to thank everyone in the ACDC group for the great times we spent together. For the group dinners, the game nights, the picnics, and for the many meetings and the constructive feedback I got in these meetings. I will always be proud of being part of this team comprised of these great people. I also want to thank everyone in the PL group for the many productive discussions we had during my PhD. This is the best spot to thank another collaborator, Malcolm Abbott, for his great ideas, comments, and suggestions, which made Chapter 6 possible.

A huge thank you goes to the people at SIRC who helped me with sample preparation and measurements. Especially to the operation team who always went beyond their duties to help me prepare my samples at the last moment! This thesis would not be possible without your help. Thank you, Huy, Vy, Thu, and An. Many thanks to Ute Schubert from ANFF who helped me with several AlO_x depositions. I want to thank Moonyong Kim for helping with the degradation of samples for Chapter 3, Simon Hager for helping with the EBSD measurements presented in Chapter 4, Mieka Figg for helping with lifetime measurements used in Chapter 5, and Tsun Hang Fung for helping with the degradation of cells used for Chapter 6.

I want to thank everyone in the LDOT team for keeping the labs safe and operational, and for accepting many of my last-minute requests to enter the lab! A special thank you goes to Kian Chin, Nick Shaw, and Alan Yee for always answering my questions and requests with enormous patience.

I had the pleasure of working with several external collaborators throughout my thesis. I would like to thank Joyce Ann De Guzman, Vladimir Markevich, and Anthony Peaker from the University of Manchester, and Thien Truong from Australian National University.

The process of writing this thesis has not been easy, but having great reviewers made it possible. Many thanks to Yan, uRob, Arman, and Malcolm for the huge help improving this thesis. A very special thank you to John Rodriguez who accepted to read my whole thesis and gave me valuable feedback until the last second!

I had the privilege of having great friends here in Sydney. I want to thank Arman for the many short and very long chats and discussions, especially in the final phase of my PhD. Thanks a lot “DADA”. I also want to thank Yoann. Thank you for being my math buddy and helping me evaluate my ideas, and for always asking me to join different events and parties. I want to thank the members of the pre-Covid lunch group, Arastoo, Yasaman, Ali, and Farzaneh. It was a great break from work to meet you and have a chat in Farsi. A special thank you goes to Yasaman and Arastoo as they were a huge help at the start of my journey when I needed the guidance of a friend the most. Many thanks to my friends and housemates, Ashkan and Siroos, for all the fun times we had together. I also want to thank my friend (and soon-to-be housemate) Hamid for the Saturday chats about life and work.

Back home, I want to thank my dear friends Amir and Parham, whose friendship is of the best things to happen in my life.

Last but certainly not least, I want to thank my family. Thanks a lot to my sister Sonia, for always caring about her little brother, and thanks to mom and dad, for your unconditional love and support throughout my whole life. It is great to be your child.

Contents

Abstract	iii
Acknowledgment	v
Contents	vii
Abbreviations and Symbols	x
Abbreviations	x
Roman symbols	xi
Greek symbols	xiii
List of Publications	xv
Journal publications	xv
Conference publications	xv
Chapter 1 Introduction	17
1.1 Motivation	17
1.2 Thesis objectives	19
1.3 Thesis outline	20
Chapter 2 Literature Review	22
2.1 Bulk recombination and lifetime	22
2.1.1 Radiative recombination	23
2.1.2 Auger recombination	24
2.1.3 SRH recombination	25
2.1.4 Bulk lifetime calculation	27
2.1.5 Lifetime measurement	28
2.2 Temperature- and injection-dependent lifetime spectroscopy	31
2.3 Minority carrier traps	36

2.4	Light-induced degradation	39
2.4.1	LID in B-doped Cz silicon wafers.....	40
2.4.2	LeTID in p-type mc-Si wafers.....	41
2.4.3	LID in Ga- and In-doped Cz silicon wafers	43
2.5	Chapter summary	44
Chapter 3	Investigation of Traps in Boron-Doped Czochralski Silicon.....	46
3.1	Traps in B-doped Cz silicon	46
3.2	Materials and methods.....	47
3.3	Results and discussion.....	52
3.3.1	Presence of traps in the annealed state	52
3.3.2	Correlation between trap density and defect density.....	58
3.3.3	Doping- and temperature-dependent PCD measurements	62
3.4	Chapter summary	68
Chapter 4	Investigation of Traps in Boron-Doped Multicrystalline Silicon	71
4.1	Traps in B-doped mc-Si	71
4.2	Materials and methods.....	72
4.3	Results and discussion.....	75
4.3.1	Presence of trap-related long PCD time constant.....	75
4.3.2	Effect of firing on traps	78
4.3.3	Effect of laser annealing on traps	82
4.3.4	Impurity-related defects as a trapping center source.....	86
4.3.5	Structural defects as a trapping center source	87
4.4	Chapter summary	91
Chapter 5	Investigation of Light-Induced Degradation in Gallium- and Indium-Doped Czochralski Silicon	94
5.1	Materials and methods.....	95
5.2	Results and discussion.....	96

5.2.1	Kinetics of LID in Ga- and In-doped Cz silicon	96
5.2.2	Analysis of LID-related defects in Ga-doped Cz silicon.....	101
5.2.3	Traps in Ga-doped Cz silicon	104
5.3	Chapter summary	110
Chapter 6	Bulk Defect Characterization in Metalized Solar Cells Using Temperature-Dependent Suns- V_{oc} Measurements	113
6.1	Materials and methods.....	114
6.2	Results and discussion.....	116
6.2.1	Investigation of BO-related defects in cells	116
6.2.2	Investigation of LID in Ga-doped cells	119
6.2.3	Sensitivity analysis	121
6.3	Chapter summary	131
Chapter 7	Summary and Outlook	134
7.1	Conclusions	134
7.2	Future work	136
References	137

Abbreviations and Symbols

Abbreviations

Al	Aluminum
ALD	Atomic layer deposition
AlO _x	Aluminum oxide
B	Boron
BO	Boron-oxygen complex
CH ₄	Methane
c _n	Electron capture
CO ₂	Carbon dioxide
c _p	Hole capture
Cz	Czochralski
DA	Dark annealing
DLTS	Deep-level transient spectroscopy
DPSS	Defect parameter solution surface
DRM	Depletion region modulation
e _n	Electron emission
e _p	Hole emission
Fe	Iron
FTIR	Fourier transform infrared spectroscopy
FZ	Float zone
Ga	Gallium
HF	Hydrofluoric acid
HNO ₃	Nitric acid
IDLS	Injection-dependent lifetime spectroscopy
In	indium
LCOE	Levelized cost of electricity
LED	Light emitting diode

LeTID	Light- and elevated temperature-induced degradation
LID	Light-induced degradation
mc-Si	Multicrystalline silicon
ND	Neutral density
NDD	Normalized defect density
N_{dop} -IDLS	Doping- and injection-dependent lifetime spectroscopy
Ni	Nickle
NTD	Normalized trap density
O	Oxygen
O _i	Interstitial oxygen
P	Phosphorous
PC	Photoconductance
PCD	Photoconductance decay
PECVD	Plasma-enhanced chemical vapor deposition
PERC	Passivated emitter and rear cell
PL	Photoluminescence
PV	Photovoltaic
QSS	Quasi-steady state
SiN _x	Silicon nitride
SiN _x :H	Hydrogenated silicon nitride
SiO _x	Silicon oxide
SNR	Signal-to-noise ratio
SRH	Shockley-Read-Hall
Suns- $V_{oc}(T)$	Temperature-dependent Suns- V_{oc}
TDD	Thermal double donor
TIDLS	Temperature- and injection-dependent lifetime spectroscopy
TOPCon	Tunnel oxide passivated carrier-selective contacts
TTL	Through the lens

Roman symbols

A	Pre-exponential factor (siemens)
B	Radiative recombination coefficient ($\text{cm}^3 \cdot \text{s}^{-1}$)
C_n	Auger coefficient for the eeh process ($\text{cm}^6 \cdot \text{s}^{-1}$)

C_p	Auger coefficient for the ehh process ($\text{cm}^6 \cdot \text{s}^{-1}$)
C_{PL}	Photoluminescence calibration constant ($\text{cm}^3 \cdot \text{s} \cdot \text{V}$)
E_a	Activation energy (eV)
E_c	Conduction band edge (eV)
ER_k	Error in the extracted capture cross-section ratio (%)
E_t	Energy level of recombination-active defect (eV)
E_T	Energy level of minority carrier trap (eV)
E_v	Valence band edge (eV)
f_i	Occupancy ratio
f_{i0}	Occupancy ratio in the dark
G	Generation rate ($\text{cm}^{-3} \cdot \text{s}^{-1}$)
g_{eeh}	Enhancement factor for the eeh process
g_{ehh}	Enhancement factor for the ehh process
k	Capture cross-section ratio
k_B	Boltzmann constant ($\text{eV} \cdot \text{K}^{-1}$)
n	Electron density in the conduction band (cm^{-3})
N	Number of data points
n_0	Hole density in the conduction band at thermal equilibrium (cm^{-3})
n_l	Shockley-Read-Hall electron density (cm^{-3})
N_A	Acceptor density (cm^{-3})
N_c	Effective density of states in the conduction band (cm^{-3})
n_i	Intrinsic carrier density (cm^{-3})
N_t	Defect density (cm^{-3})
N_v	Effective density of states in the valence band (cm^{-3})
p	Hole density in the valence band (cm^{-3})
p_0	Hole density in the valence band at thermal equilibrium (cm^{-3})
p_l	Shockley-Read-Hall hole density (cm^{-3})
q	Elementary charge (C)
S_{PL}	Photoluminescence signal (V)
T	Temperature (K)
t	Time (s)
$t_{excitation}$	Excitation time (s)
U	Recombination rate ($\text{cm}^{-3} \cdot \text{s}^{-1}$)

U_{Auger}	Auger recombination rate ($\text{cm}^{-3}\cdot\text{s}^{-1}$)
U_{bulk}	Bulk recombination rate ($\text{cm}^{-3}\cdot\text{s}^{-1}$)
U_{eeh}	Auger recombination rate in the case of having an electron as the third particle ($\text{cm}^{-3}\cdot\text{s}^{-1}$)
U_{ehh}	Auger recombination rate in the case of having a hole as the third particle ($\text{cm}^{-3}\cdot\text{s}^{-1}$)
$U_{intrinsic}$	Intrinsic recombination rate ($\text{cm}^{-3}\cdot\text{s}^{-1}$)
U_{rad}	Radiative recombination rate ($\text{cm}^{-3}\cdot\text{s}^{-1}$)
U_{SRH}	Shockley-Read-Hall recombination rate ($\text{cm}^{-3}\cdot\text{s}^{-1}$)
U_{Total}	Total recombination rate ($\text{cm}^{-3}\cdot\text{s}^{-1}$)
w	Thickness (cm)
X	Ratio of electron and hole densities
Δn	Excess electron density (cm^{-3})
Δn_{app}	Apparent carrier density (cm^{-3})
Δn_{max}	Maximum excess electron density (cm^{-3})
Δn_t	Change in the density of traps filled with electron (cm^{-3})
Δp	Excess hole density (cm^{-3})

Greek symbols

$\Delta\sigma$	Photoconductance (siemens)
ε	Random noise
μ_n	Electron mobility ($\text{cm}^2\cdot\text{V}^{-1}\cdot\text{s}^{-1}$)
μ_p	Hole mobility ($\text{cm}^2\cdot\text{V}^{-1}\cdot\text{s}^{-1}$)
v_n	Electron thermal velocity ($\text{cm}\cdot\text{s}^{-1}$)
v_p	Hole thermal velocity ($\text{cm}\cdot\text{s}^{-1}$)
σ_n	Electron capture cross-section (cm^2)
σ_p	Hole capture cross-section (cm^2)
τ	Lifetime of carriers (s)
τ_{Auger}	Auger lifetime of carriers (s)
τ_{bulk}	Bulk lifetime of carriers (s)
τ_{DA}	Effective lifetime of carriers after dark annealing (s)
τ_{decay}	Decay time constant (s)

$\tau_{deg(t)}$	Effective lifetime of carriers after light-induced degradation for t minutes (s)
τ_{eff}	Effective lifetime of carriers (s)
$\tau_{eff(with_defect)}$	Effective lifetime of carriers with the presence of the defect under investigation (s)
$\tau_{eff(without-defect)}$	Effective lifetime of carriers without the presence of the defect under investigation (s)
τ_{SRH}^{HLI}	Shockley-Read-Hall lifetime of carriers at high injection level (s)
$\tau_{intrinsic}$	Intrinsic lifetime of carriers (s)
τ_{SRH}^{LLI}	Shockley-Read-Hall lifetime of carriers at low injection level (s)
τ_{LID}	Light-induced degradation-related Shockley-Read-Hall lifetime of carriers (s)
τ_{n0}	Electron capture time constant (s)
τ_{other}	Lifetime of carriers related to factors except for investigated Shockley-Read-Hall defect, intrinsic, and surface recombination (s)
τ_{p0}	Hole capture time constant (s)
τ_{rad}	Radiative lifetime of carriers (s)
τ_{SRH}	Shockley-Read-Hall lifetime of carriers (s)
$\tau_{surface}$	Surface lifetime of carriers (s)

List of Publications

Journal publications

1. M. Umair, D. Chen, **S. Jafari**, T. Ohshima, H. Abe, Z. Hameiri, C. M. Chong, and M. Abbott, “Degradation and regeneration of radiation-induced defects in silicon: A study of vacancy-hydrogen interactions”, *Sol. Energy Mater. Sol. Cells*, vol. 200, pp.109990, 2019.
2. **S. Jafari**, Y. Zhu, F. Rougieux, J. Du Guzman, V. Markevich, A. Peaker, and Z. Hameiri, “On the correlation between light-induced degradation and minority carrier traps in boron-doped Czochralski silicon”, *ACS Appl. Mater. Interfaces*, vol. 13, pp. 6140-6146, 2021.
3. **S. Jafari** and Z. Hameiri, “Investigation of minority carrier traps in *p*-type mc-Si: Effect of firing and laser annealing”, *Sol. Energy Mater. Sol. Cells*, vol. 232, pp. 111341, 2021.
4. **S. Jafari**, M. Abbott, D. Zhang, J. Wu, F. Jiang, and Z. Hameiri, “Bulk defect characterization in metalized solar cells using temperature-dependent Suns- V_{oc} measurements”, *Sol. Energy Mater. Sol. Cells*, vol. 236, pp. 111530, 2022.
5. **S. Jafari**, M. Figg, and Z. Hameiri, “Investigation of light-induced degradation in gallium- and indium-doped Czochralski silicon wafers”, Under preparation.

Conference publications

1. **S. Jafari**, Y. Zhu, F. Rougieux, and Z. Hameiri, “Trapping in multi-crystalline silicon wafers: Impact of laser treatment and firing”, in *36th European Photovoltaic Solar Energy Conference and Exhibition (EUPVSEC)*, 2019.
2. **S. Jafari**, Y. Zhu, F. Rougieux, and Z. Hameiri, “Trapping in multi-crystalline silicon wafers: The impact of firing and laser treatment”, in *Asia-Pacific Solar Research Conference (APSRC)*, 2019.
3. **S. Jafari**, Y. Zhu, F. Rougieux, J. Du Guzman, V. Markevich, A. Peaker, and Z. Hameiri, “Boron-oxygen related light-induced degradation of Si solar cells:

- Transformation between minority carrier traps and recombination active centers”, in *47th IEEE Photovoltaic Specialist Conference (PVSC)*, 2020. (**Won the Best Student Award**)
4. **S. Jafari**, Y. Zhu, F. Rougieux, J. Du Guzman, V. Markevich, A. Peaker, and Z. Hameiri, “Boron-oxygen-related traps in Czochralski grown silicon”, in *Asia-Pacific Solar Research Conference (APSRC)*, 2020.
 5. **S. Jafari**, and Z. Hameiri, “Investigation of light-induced degradation in Ga- and In-doped Cz silicon”, in *48th IEEE Photovoltaic Specialist Conference (PVSC)*, 2021.

Chapter 1

Introduction

1.1 Motivation

There is more than 99% agreement in the published literature regarding the impact of human activities on the emergence of *climate change* [1]. The main impact induced by humans is the emission of greenhouse gases, which results in an increase in the earth's average temperature [2], via the *greenhouse effect* [2]. A representation of this effect is shown in Fig. 1.1. Without any greenhouse gasses, the absorption of solar radiation is balanced with the earth's surface emission which is proportional to the fourth power of surface temperature. With the presence of greenhouse gasses, they absorb a part of the emitted heat from the earth's surface. Some of this absorbed heat is emitted back to the earth in the infrared range. To maintain the balance between heat absorption and emission, the earth's surface temperature increases to emit even more heat [3]. With an increased level of greenhouse gases, this phenomenon is amplified leading to a further increase in the earth's temperature [3, 4]. This effect has been denoted as *global warming*. The average increase in the northern hemisphere's temperature with time is shown in Fig. 1.2. The average temperature shows a significant and abrupt increase in the past hundred years, after ~ 1,000 years of slight decrease [4]. The very important impact of this global warming is a change in the global climate pattern, thus, the expression "climate change" is more suitable than "global warming" to describe this problem [5].

The two main greenhouse gases are carbon dioxide (CO₂) and methane (CH₄) with CO₂ having the higher global emission of the two comprising ~ 76% of the total greenhouse gas emissions [6]. A significant portion of this emitted greenhouse gas (~ 73%) is due to energy needs [7] with burning fossil fuels being the greatest contributor [4]. Reducing greenhouse gas emissions is the cornerstone of every proposal to battle against climate change [8, 9], thus, substituting fossil fuels with clean renewable energies is a crucial step in this battle. Solar energy is renewable energy which is projected to be the largest source of energy production by 2050 [10]. The annual solar energy received

by the emerged continents is $\sim 23,000$ TWy, which is $\sim 1,500$ times the amount of the total annual energy consumption by humans [11]. The two main solar energy types are photovoltaic (PV) and solar thermal with the first one having the larger energy market by far [12].

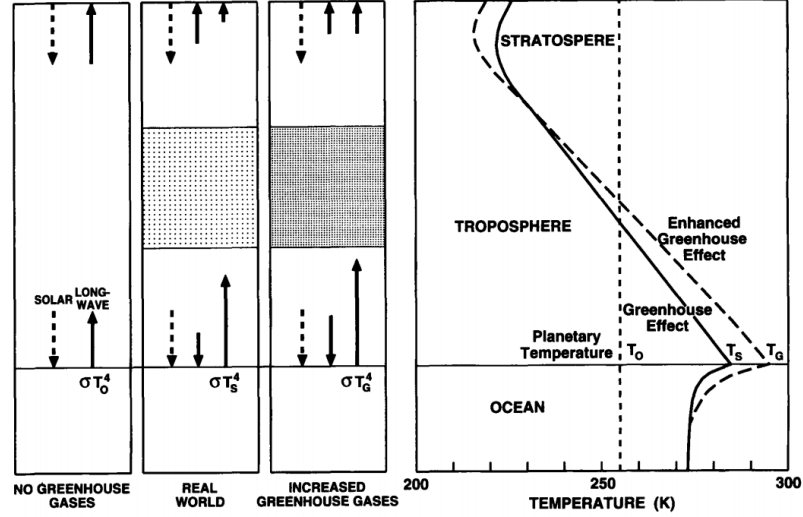


Fig. 1.1. A representation of the greenhouse effect and its impact on the earth's temperature [3].

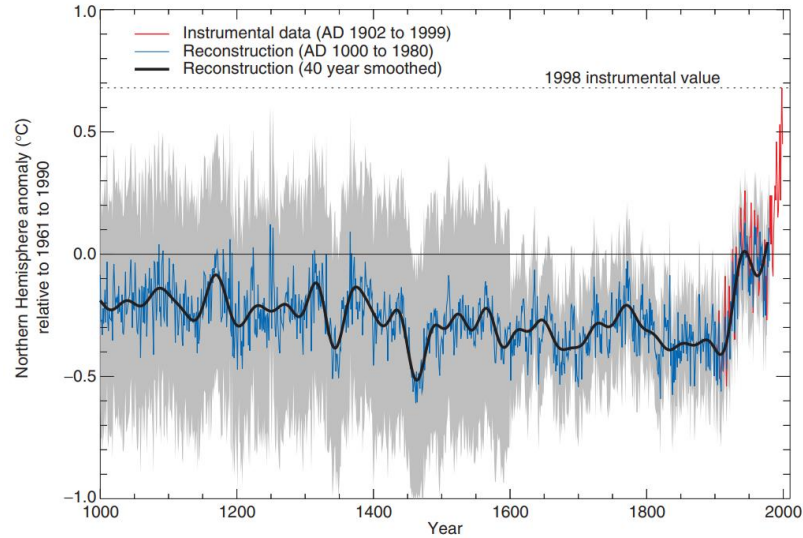


Fig. 1.2. The millennial temperature of the northern hemisphere as a function of time, relative to the average temperature in the 1961 to 1990 period. The grey area is a two standard error limit [6].

Besides being clean, renewable, and abundant, the rapid reduction in its levelized cost of electricity (LCOE) is another driving force behind the shift from fossil fuel-based electricity to solar energy [13]. In Fig. 1.3, the price learning curve of PV-based energy between 1976 to 2019 is shown. The price of PV-based electricity has dropped by more than ~ 500 times making it the cheapest form of electricity production [13, 14]. To continue following this learning curve and further reducing the cost of PV, an increase in the efficiency of solar cells is required.

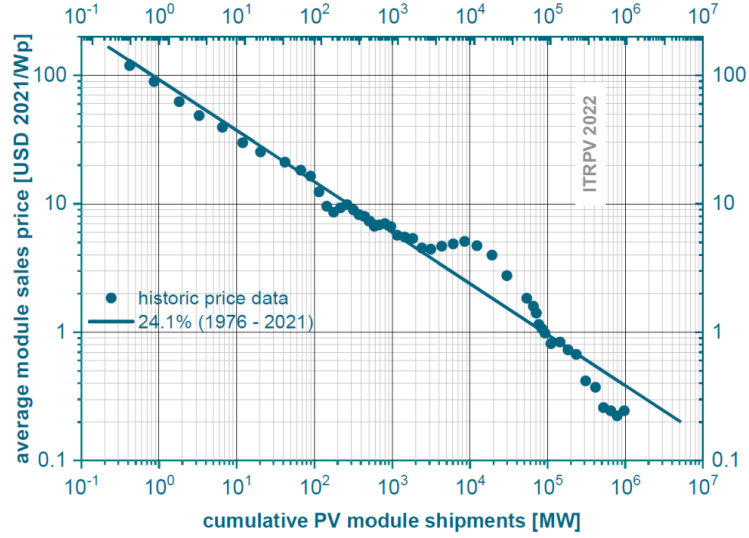


Fig. 1.3. Crystalline silicon PV energy price learning curve. The solid line is a fit to the data [13].

1.2 Thesis objectives

Currently, silicon-based solar cells account for $\sim 96\%$ of the total PV market with monocrystalline silicon solar cells having more than two-thirds of the market share and multicrystalline silicon (mc-Si) having about a third of the share [15]. The efficiencies of these two types of solar cells have been improved over the years and have reached $> 26\%$ for monocrystalline- and $> 23\%$ for mc-Si wafers (research-level efficiencies), with numbers increasing rapidly [16, 17]. To further improve these efficiencies, it is important to enhance their bulk charge carrier lifetime. For this purpose, it is necessary to: 1) develop new methods to investigate bulk defects in silicon wafers; and 2) study the impact of the defects on the lifetime which affect solar cell voltage and, hence, efficiency.

Thus, the objective of this thesis is to investigate two types of bulk defects: recombination-active defects and minority carrier traps (traps) in *p*-type silicon wafers, which is still currently the dominant bulk doping polarity for commercial silicon solar cells. This is done by developing new and targeted bulk characterization methods as well as investigating light-related degradation in *p*-type silicon wafers. The aims of this thesis are:

1. To optimize the photoconductance decay (PCD) measurement method for the investigation of traps;
2. To apply this method to study traps in *p*-type monocrystalline- and mc-Si;
3. To investigate the kinetics of light-induced degradation (LID) in gallium (Ga)-doped silicon wafers;

4. To identify the LID-related defect in Ga-doped Czochralski (Cz) wafers; and
5. To develop a method for the characterization of defects in completed and fully metalized solar cells.

1.3 Thesis outline

In Chapter 2, the basic concepts of bulk recombination and its mechanisms, lifetime, and minority carrier traps are reviewed. Moreover, the temperature- and injection-dependent lifetime spectroscopy (TIDLS) technique for defect characterization is presented. In the last section, a brief overview of LID in three different types of *p*-type silicon wafers is provided.

In Chapter 3, PCD measurements are used to investigate the correlation between traps and boron-oxygen (BO)-related defects in boron (B)-doped Cz silicon wafers. Doping- and temperature-dependent measurements are performed to better understand the nature of the traps.

In Chapter 4, the PCD method is used to investigate traps in B-doped mc-Si wafers. The impact of firing and laser annealing processes on traps is studied. The possible source of the traps is examined in the last section of this chapter by investigating samples with different impurities and structural defects, through contrasting mono-cast silicon wafers.

In Chapter 5, Ga- and indium (In)-doped Cz silicon wafers are investigated and their LID properties are studied. Their defect formation and annihilation activation energies are measured. Furthermore, the parameters of the LID-related defect in Ga-doped wafers are extracted for the first time. Traps in Ga-doped wafers are also studied in this chapter.

In Chapter 6, a new method for the extraction of defect parameters from fully metalized solar cells is developed, based on temperature-dependent Suns- V_{oc} measurements, Suns- $V_{oc}(T)$. This method is validated by extracting the parameters of a well-known defect with known defect parameters. The Suns- $V_{oc}(T)$ method is then used to extract the parameters of the defect causing LID in Ga-doped cells. A sensitivity analysis is performed at the end of the chapter.

Finally, in Chapter 7, the important findings are reviewed and suggestions for future works are given.

Chapter 2

Literature Review

The presence of defects in silicon wafers impacts their electrical properties. Recombination-active defects reduce the carrier lifetime, which in turn affects the efficiency of solar cells. On the other hand, traps cause artificially high lifetime measurements hindering the correct lifetime assessment. The basic concepts of recombination-active defects and traps are presented in this chapter, and a method based on lifetime spectroscopy for defect characterization is also reviewed. Finally, three types of LID (which are investigated in subsequent chapters), are discussed.

2.1 Bulk recombination and lifetime

The creation of electron-hole pairs due to optical (and to a lesser extent, thermal) excitation is called *generation*. This process is the main principle of electricity generation in solar cells. With this process, the electrons are excited to the conduction band, while holes are generated in the valence band, both acting as free carriers. The inverse of the generation is *recombination* which results in the annihilation of electrons and holes [18]. Thus, recombination is considered an unwanted process that decreases the efficiency of solar cells. Recombination can happen in different regions of solar cells [18-21]. This section will review the recombination sources in the bulk of silicon wafers.

Bulk recombination is a result of three mechanisms: radiative recombination [22], Auger recombination [18], and Shockley-Read-Hall (SRH) recombination [23, 24]. The first two recombination mechanisms are referred to as intrinsic recombination as they are present even in pure silicon wafers (with no impurity or structural defects) [25]. Whereas, SRH recombination is classified as extrinsic recombination as it is caused by the presence of defects in silicon wafers [25].

For each recombination mechanism, a minority carrier *lifetime* can be defined. In a *p*-type sample, this lifetime is the average time it takes for an electron (minority carrier in *p*-type silicon wafers) to recombine after it is generated. Thus in a *p*-type sample [25]:

$$\tau = \frac{\Delta n}{U} \quad (2.1)$$

where τ is the carrier lifetime, Δn is the excess electron density (injection) generated due to the excitation, and U is the recombination rate.

2.1.1 Radiative recombination

Radiative recombination is the reverse process of generation via optical excitation. In this process, the electron and hole pairs are directly recombined and as a result, a photon is emitted [see Fig. 2.1 (a)]. Since this mechanism involves one electron and one hole, the rate of this recombination depends on the density of electrons in the conduction band (n), and holes in the valence band (p) [18]:

$$U_{rad} = B(np - n_i^2) \quad (2.2)$$

where U_{rad} is the radiative recombination rate, B is the radiative recombination coefficient, and n_i is the intrinsic carrier density. Moreover, $n = n_0 + \Delta n$ and $p = p_0 + \Delta p$, where n_0 (p_0) is the electron (hole) density in thermal equilibrium and Δp is the excess hole density. B is a measure of the probability of radiative recombination which depends on the band structure of the semiconductor and has been determined in several studies [22, 26-28]. The carrier lifetime corresponding to the radiative recombination is:

$$\tau_{rad} = \frac{\Delta n}{U_{rad}} = \frac{\Delta n}{B(np - n_i^2)} \quad (2.3)$$

where τ_{rad} is the radiative recombination lifetime. Simplifying Eq. (2.3) for a p -type sample ($p_0 \gg n_0$) considering the law of mass action ($n_0 p_0 = n_i^2$) [29]:

$$\tau_{rad} = \frac{1}{B(p_0 + \Delta n)} \quad (2.4)$$

Thus, at low injection levels ($p_0 \gg \Delta n$) the radiative lifetime is independent of the excess carrier concentration and depends only on the doping concentration.

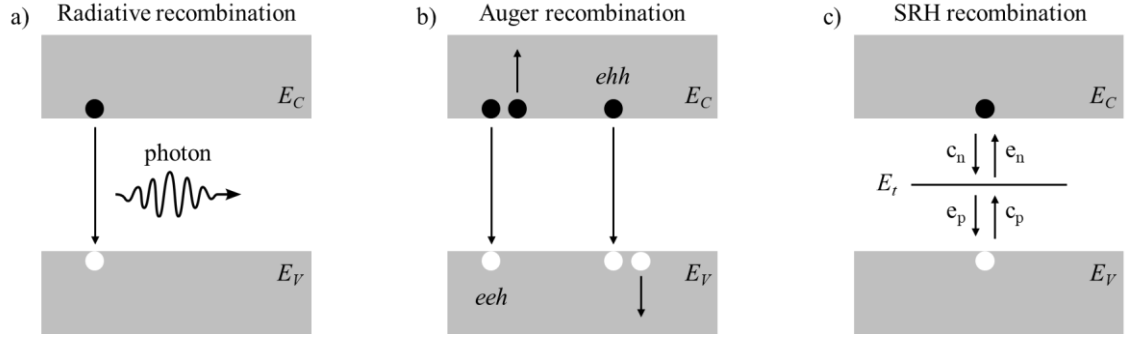


Fig. 2.1. Schematic of: (a) radiative recombination; (b) Auger recombination; and (c) SRH recombination mechanisms.

2.1.2 Auger recombination

The other intrinsic recombination mechanism in silicon wafers is Auger recombination. In this mechanism, the energy released after the recombination of an electron-hole pair is transferred to a third free carrier, resulting in the excitation of this carrier [see Fig. 2.1 (b)]. If this third particle is an electron, the recombination rate is denoted by U_{eeh} while if the third particle is a hole, the recombination rate is named U_{ehh} . In each of the two cases, two particles of one type are present, thus the recombination rate is proportional to n^2p (eeh case) or np^2 (ehh case). The total recombination rate due to the Auger recombination (U_{Auger}) is given by [30]:

$$U_{Auger} = U_{eeh} + U_{ehh} = C_n(n^2p - n_0^2p_0) + C_p(np^2 - n_0p_0^2) \quad (2.5)$$

where C_n (C_p) is the Auger coefficient for the eeh (ehh) process. However, a deviation from Eq. (2.5) is observed in the experimental measurements (especially in samples with low doping density) [31]. It has been suggested that this deviation is connected with the Coulomb interaction between carriers [32]. Thus, modified Auger recombination is defined as Coulomb-enhanced Auger recombination. The enhanced recombination rate is [33]:

$$U_{Auger} = C_n g_{eeh}(n^2p - n_0^2p_0) + C_p g_{ehh}(np^2 - n_0p_0^2) \quad (2.6)$$

with g_{eeh} and g_{ehh} being enhancement factors. Thus, the Auger lifetime for a p -type sample becomes:

$$\tau_{Auger} = \frac{\Delta n}{U_{Auger}} = \frac{1}{C_n g_{eeh} p \Delta n + C_p g_{ehh} p^2} \quad (2.7)$$

Assuming that an equal number of excess electrons and holes are generated in the sample ($\Delta n = \Delta p$):

$$\tau_{Auger} = \frac{\Delta n}{U_{Auger}} = \frac{1}{\Delta n^2 (C_n g_{eeh} p_0 + C_p g_{ehh} p_0^2)} \quad (2.8)$$

As shown in Eq. (2.8), τ_{Auger} is inversely proportional with the square of Δn . Thus, it decreases significantly as Δn increases and is typically the dominant recombination mechanism at high injection levels.

2.1.3 SRH recombination

The presence of impurities and point defects in the silicon lattice can lead to the formation of discrete energy levels in the bandgap. This energy level can act as a recombination channel. As mentioned previously, SRH recombination is extrinsic recombination, meaning that in a wafer without any impurity or structural defects, such energy level does not exist, and this recombination mechanism is not present.

Due to the presence of an energy level in the bandgap, four possible transitions can happen. As shown in Fig. 2.1 (c), these transitions are electron capture (c_n), electron emission (e_n), hole emission (e_p), and hole capture (c_p) [18]. Thus, assuming a defect level initially filled with an electron, three types of two-step processes are possible:

1. **Generation of carriers through defect level ($e_n + e_p$):** This process happens with an electron emission, followed by a hole emission. As a result, an electron-hole pair is generated.
2. **Trapping of carriers ($e_n + c_n$ or $c_p + e_p$):** This happens when the emission of an electron is followed by the capture of an electron or when the capture of a hole is followed by the emission of a hole. In this process, the energy level only has an interaction with one energy band and the total number of carriers in each band does not change (no generation or recombination).
3. **Recombination of carriers ($c_p + c_n$):** This process happens when the capture of a hole is followed by the capture of an electron. As a result, one electron-hole pair has recombined through the defect energy level.

In the case of recombination-active bulk defects, if the assumptions that:

1. The defect has one energy level; and
2. The defect is a point defect (interstitial atoms, substitutional atoms, etc.) and not an extended defect (grain boundaries, stacking faults, etc.),

are satisfied, the total recombination rate through these defects can be described with an equation, derived by Shockley, Read [23], and Hall [24]:

$$U_{SRH} = \frac{np - n_i^2}{\tau_{p0}(n + n_1) + \tau_{n0}(p + p_1)} \quad (2.9)$$

where U_{SRH} is the SRH recombination rate and τ_{p0} and τ_{n0} are hole and electron capture time constants, respectively, and are defined as:

$$\tau_{p0} = \frac{1}{\sigma_p v_p N_t} \quad \text{and} \quad \tau_{n0} = \frac{1}{\sigma_n v_n N_t} \quad (2.10)$$

where σ_p (σ_n) is the hole (electron) capture cross-section, v_p (v_n) is the hole (electron) thermal velocity, and N_t is the defect density. Moreover, n_1 and p_1 are SRH electron and hole densities, respectively, and are defined as:

$$n_1 = N_c \exp\left(-\frac{E_c - E_t}{k_B T}\right) \quad \text{and} \quad p_1 = N_v \exp\left(-\frac{E_t - E_v}{k_B T}\right) \quad (2.11)$$

where N_c (N_v) is the effective density of states in the conduction (valence) band, E_c (E_v) is the energy of conduction (valence) band, E_t is the energy level of the recombination center, k_B is the Boltzmann constant, and T is temperature.

Assuming that an equal number of excess electrons and holes are generated in the sample ($\Delta n = \Delta p$), the corresponding lifetime through SRH defects (SRH lifetime) becomes:

$$\tau_{SRH} = \frac{\Delta n}{U_{SRH}} = \frac{\tau_{n0}(p_0 + p_1 + \Delta n) + \tau_{p0}(n_0 + n_1 + \Delta n)}{n_0 + p_0 + \Delta n} \quad (2.12)$$

where τ_{SRH} is the SRH lifetime. The capture cross-section ratio (k) is defined as $k = \tau_{p0}/\tau_{n0} = \sigma_n/\sigma_p$, which leads to:

$$\tau_{SRH} = \tau_{n0} \left(\frac{p_0 + p_1 + \Delta n}{n_0 + p_0 + \Delta n} + k \frac{n_0 + n_1 + \Delta n}{n_0 + p_0 + \Delta n} \right) \quad (2.13)$$

meaning that the shape of the injection-dependent SRH lifetime curve depends on two unknowns, k and E_t (through p_1 and n_1), while τ_{n0} is a scaling factor that shifts the overall curve up or down but does not have an impact on the shape of the curve.

For a p -type sample, looking at two special cases of low injection and high injection levels, Eq. (2.13) further simplifies to:

$$\tau_{SRH}^{LLI} = \tau_{n0} \left(1 + \frac{p_1}{p_0} + k \frac{n_1}{p_0} \right) \quad (2.14)$$

$$\tau_{SRH}^{HLI} = \tau_{n0} (1 + k) \quad (2.15)$$

where τ_{SRH}^{LLI} and τ_{SRH}^{HLI} are SRH lifetime at low and high injection levels, respectively. This clearly shows that the SRH lifetime at low and high injection levels is independent of Δn .

2.1.4 Bulk lifetime calculation

The net rate of carrier recombination in the bulk (U_{bulk}) of a silicon wafer is the sum of different recombination rates through all the channels:

$$U_{bulk} = (U_{rad} + U_{Auger}) + U_{SRH} = U_{intrinsic} + U_{SRH} \quad (2.16)$$

where $U_{intrinsic}$ is the total recombination rate through intrinsic recombination channels. Thus, the bulk lifetime (τ_{bulk}), corresponding to all bulk recombination channels can be calculated as:

$$\frac{1}{\tau_{bulk}} = \frac{U_{bulk}}{\Delta n} = \frac{1}{\tau_{rad}} + \frac{1}{\tau_{Auger}} + \frac{1}{\tau_{SRH}} = \frac{1}{\tau_{intrinsic}} + \frac{1}{\tau_{SRH}} \quad (2.17)$$

where $\tau_{intrinsic}$ is the intrinsic lifetime. From Eq. (2.17), it can be concluded that the higher bound of the bulk lifetime at each injection level is limited by the lowest lifetime among all the channels.

The radiative, Auger, and SRH injection-dependent lifetime curves of a p -type sample at 30 °C with $1 \times 10^{16} \text{ cm}^{-3}$ acceptor density (N_A) are simulated using Eq. (2.4), Eq. (2.8), and Eq. (2.13) and presented in Fig. 2.2. The defect used for the generation of τ_{SRH} has an energy level in the mid-gap, $k = 50$, $N_t = 1 \times 10^{13} \text{ cm}^{-3}$, and $\sigma_n = 1 \times 10^{-16} \text{ cm}^2$. As stated previously, the radiative, Auger, and SRH lifetime curves are constant at low injection levels. τ_{SRH} is constant at high injection levels as well. Another observation is the higher injection-dependence of Auger recombination compared with radiative recombination. This is because radiative recombination is correlated with Δn , while Auger recombination is correlated with Δn^2 . Moreover, as stated before, the bulk lifetime at each injection level is limited by the lowest lifetime. While in the low injection range, the bulk lifetime is limited by the τ_{SRH} , at the high injection range, τ_{Auger} is the limiting factor. Between these

two regions, a combination of both recombination mechanisms determines the overall bulk lifetime value.

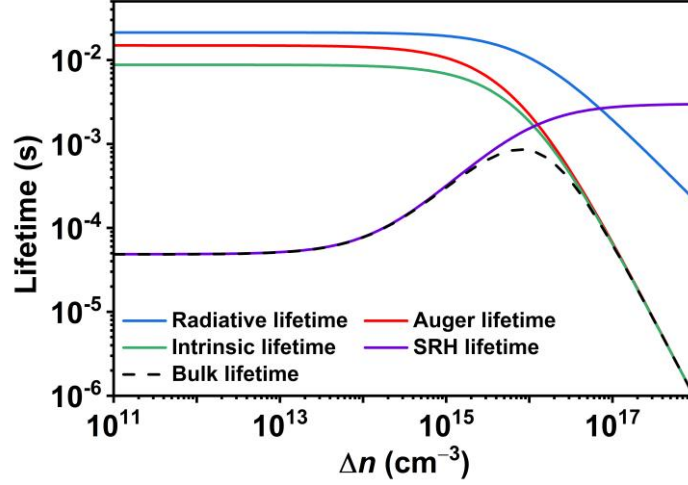


Fig. 2.2. Simulated radiative, Auger, and SRH injection-dependent lifetime curves for p -type silicon with $N_A = 1 \times 10^{16} \text{ cm}^{-3}$ at 30°C with an SRH defect with the energy level in the mid-gap, $k = 50$, $N_t = 1 \times 10^{13} \text{ cm}^{-3}$, and $\sigma_n = 1 \times 10^{-16} \text{ cm}^2$.

2.1.5 Lifetime measurement

In a sample with uniform carrier distribution, the change in the excess electron concentration in the conduction band with time is equal to the generation rate (G) minus total recombination rate (U_{Total}):

$$\frac{d\Delta n}{dt} = G - U_{Total} = G - \frac{\Delta n}{\tau_{eff}} \quad (2.18)$$

where τ_{eff} is the effective lifetime impacted by bulk and surface recombination:

$$\frac{1}{\tau_{eff}} = \frac{1}{\tau_{bulk}} + \frac{1}{\tau_{surface}} \quad (2.19)$$

where $\tau_{surface}$ is the surface lifetime. From Eq. (2.18), the effective lifetime becomes:

$$\tau_{eff} = \frac{\Delta n}{G - \frac{d\Delta n}{dt}} \quad (2.20)$$

meaning that the effective lifetime can be calculated by knowing the generation rate and the excess electron concentration at any given time after the excitation.

To measure the injection-dependent lifetime of wafers, typically, photoconductance (PC)-based measurements are performed [34]. In these measurements, the excess carriers

are generated using a light source, and the change in the conductance due to the excitation is measured using an inductive coil. The measured PC is directly correlated to the sum of the excess majority and minority carriers [35]:

$$\Delta\sigma = qw(\mu_n\Delta n + \mu_p\Delta p) \quad (2.21)$$

where $\Delta\sigma$ is the change in conductance, q is the elementary charge, w is the wafer thickness, and μ_n (μ_p) is the electron (hole) mobility. To calculate the excess minority carrier density from the change in PC using Eq. (2.21), the density of the excess majority and minority carriers are assumed to be equal. Since the mobility of electrons and holes are injection-dependent, an iterative procedure is performed to calculate Δn .

Another method for the measurement of the photogenerated carrier density is the photoluminescence (PL) measurement method [18]. PL is the generated luminescence due to the radiative recombination (see Section 2.1.1) of excess carriers and it is proportional to the excess carrier concentration. Thus, the PL signal (S_{PL}) of a sample, detected with a PL detector, is correlated with the density of excess carriers in the conduction and valence bands [36]:

$$S_{PL} = C_{PL}B(np - n_i^2) \quad (2.22)$$

where C_{PL} is the calibration constant and is equal to the ratio of generated photons in the sample to the detected photons by the system. For a p -type sample ($p_0 \gg n_0$), assuming that doping density is much larger than the density of defects, and considering the law of mass action [29]:

$$S_{PL} = C_{PL}B\Delta n(p_0 + \Delta n) \quad (2.23)$$

The calibration constant C_{PL} depends on the sample as well as the detection system, thus this value should be calculated for each sample separately. This is done by inserting the Δn value measured from PC-based measurement to Eq. (2.23). Since all the other parameters are known, C_{PL} can be determined. The range of Δn chosen for this purpose is the high injection range to minimize the possible impact of traps on the extracted Δn from PC-based measurement. This impact will be discussed in more detail in Section 2.3. Knowing the value for C_{PL} , the minority carrier density can be calculated:

$$(C_{PL}B)\Delta n^2 + (C_{PL}Bp_0)\Delta n - S_{PL} = 0 \quad (2.24)$$

$$\Delta n = \frac{-C_{PL}Bp_0 \pm \sqrt{(C_{PL}Bp_0)^2 + 4C_{PL}B(S_{PL})}}{2C_{PL}Bp_0} \quad (2.25)$$

Since all the parameters in this equation are positive, only one (the positive) solution for Δn is the correct value at each S_{PL} .

The PC- and PL-based lifetime measurements can be done in three conditions: (i) steady-state (SS); (ii) quasi-steady-state (QSS); and (iii) transient. In the first condition, constant illumination is used for the generation of carriers. However, this method is not used widely, as prolonged illumination results in heating the sample. Moreover, with SS excitation, performing an injection-dependent measurement is time-consuming as the illumination intensity should be modified several times to generate different injection levels. In the other two methods, a decaying excitation source is used. Thus, the PC is measured as the illumination decays, meaning that the injection-dependent measurement is done in one step (all the injection levels are swept with one measurement).

In the SS condition, the change in the excess electron concentration is zero, thus Eq. (2.20) becomes:

$$\tau_{eff} = \frac{\Delta n}{G} \quad (2.26)$$

In the case that a decaying light is used for the excitation, if $G \gg d\Delta n/dt$, Eq. (2.26) can still be used. In this case, the lifetime of the sample is much smaller than the decay time constant of the illumination source. This case is referred to as the QSS condition [37]. For this measurement, a light source with a large decay time constant is used for excitation. To determine the generation rate and in turn, the lifetime under the QSS condition, a calibrated photodiode or solar cell can be used [37].

On the other hand, if the lifetime of the sample is much larger than the decay rate of the illumination source, Eq. (2.20) can be simplified to:

$$\tau_{eff} = \frac{\Delta n}{-\frac{d\Delta n}{dt}} \quad (2.27)$$

Therefore no information regarding the generation rate is needed to calculate the lifetime. This condition is denoted as the transient condition [38].

2.2 Temperature- and injection-dependent lifetime spectroscopy

To extract the parameters of recombination-active SRH defects, TIDLS measurement can be used [39]. The extracted parameters are E_t , τ_{n0} (or τ_{p0}), and k . However, the extracted energy level is typically reported with respect to the intrinsic energy level (E_i). In other words, the reported value for the energy level is $E_t - E_i$. In this thesis, a method based on defect parameter solution surface (DPSS) curves is used to extract the defect parameters from TIDLS measurements [40]. The principles of this method are discussed below using simulated temperature- and injection-dependent τ_{SRH} curves.

The injection-dependent τ_{SRH} curve of an SRH defect with $E_t - E_i = -0.32$ eV, $k = 50$, $N_t = 1 \times 10^{13} \text{ cm}^{-3}$, and $\sigma_n = 1 \times 10^{-16} \text{ cm}^2$ at $T = 25^\circ \text{C}$ is simulated using Eq. (2.13) (with added random noise) and presented in Fig. 2.3 (a). Using Eq. (2.13) as the fitting equation, for each E_t in the bandgap range, the τ_{n0} and k that can fit the lifetime curve with the lowest fitting residual are extracted. The fitting residual is calculated by:

$$\text{Fitting residual} = \sqrt{\sum \left(\frac{F(\Delta n) - M(\Delta n)}{M(\Delta n)} \right)^2 / N} \quad (2.28)$$

where $F(\Delta n)$ and $M(\Delta n)$ are fitted and measured (simulated in this case) lifetime values at each Δn , and N is the number of data points.

By sweeping the whole bandgap range, the τ_{n0} and k solutions at each E_t are extracted and shown in Fig. 2.3 (c) and Fig. 2.3 (d), respectively. These two curves are named τ_{n0} -DPSS and k -DPSS curves for the presented lifetime. The fitting residual for each $[E_t, \tau_{n0}, k]$ combination is shown in Fig. 2.3 (b). The fitting residual shows that in a range of E_t , infinite pairs of τ_{n0} and k values can fit the lifetime curve identically. The corresponding lifetime curves for two points (I and II) are presented as an example. Both these points generate identical lifetime curves with identical fits to the simulated data. This means that both sets of $[E_t, \tau_{n0}, k]$ are possible parameters for a defect that generates this lifetime

curve. Thus, a single set of parameters can not be extracted from one injection-dependent lifetime curve.

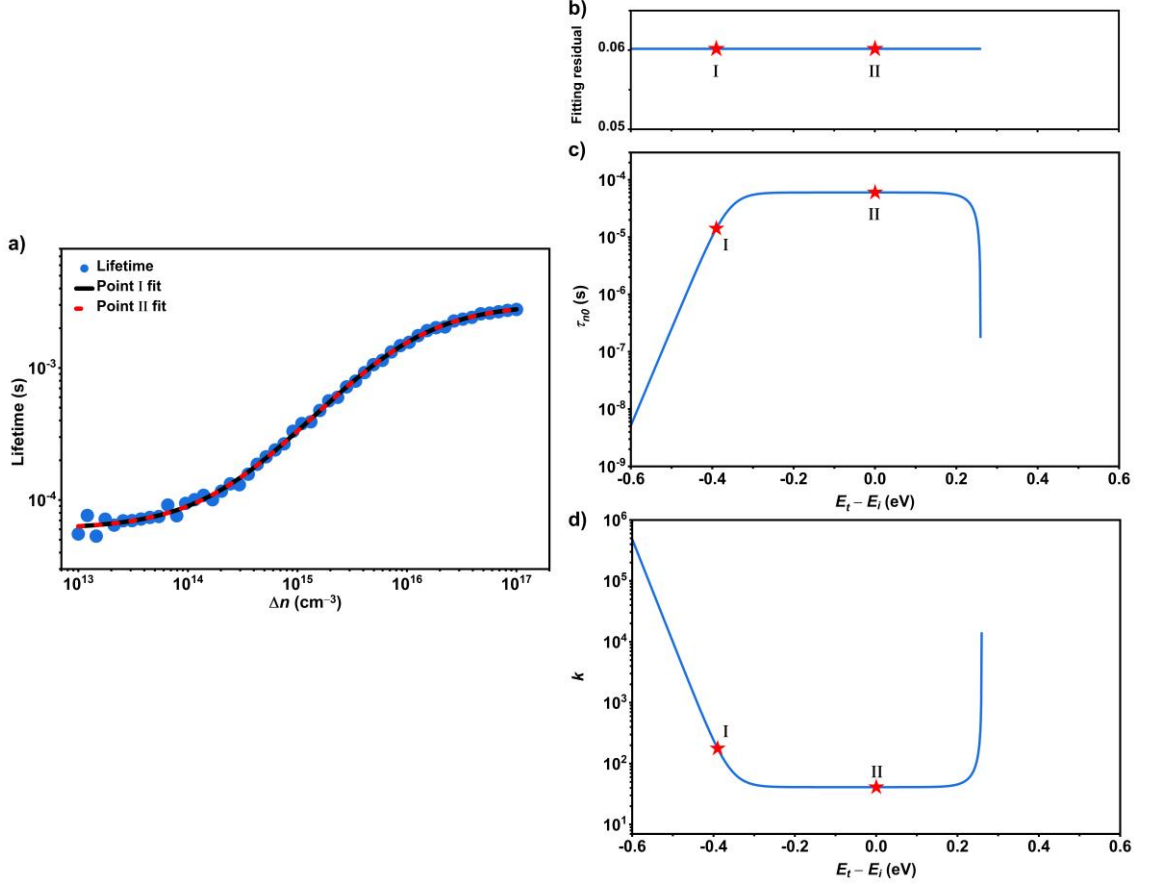


Fig. 2.3. (a) Simulated lifetime (blue dots) of a p -type wafer with $N_A = 1 \times 10^{16} \text{ cm}^{-3}$ at 25°C with an SRH defect with $E_t - E_i = -0.32 \text{ eV}$, $k = 50$, $N_t = 1 \times 10^{13} \text{ cm}^{-3}$, and $\sigma_n = 1 \times 10^{-16} \text{ cm}^2$. The solid black and dashed red lines are the SRH lifetime curves for a defect with parameters indicated by symbols “I” and “II” in (c) and (d). (b) The fitting residual for the fitted lifetime, generated from defect parameter combinations in (c) and (d). (c) The τ_{n0} -DPSS; and (d) k -DPSS curves for the simulated lifetime.

One method to address this problem is to measure the lifetime curve at various temperatures and generate a DPSS curve for each temperature. In Fig. 2.4 (a), the simulated lifetime curves for the same defect at 25°C to 100°C (25°C temperature intervals) and their corresponding fit are shown. A τ_{n0} -DPSS [see Fig. 2.4 (b)] and k -DPSS [see Fig. 2.4 (c)] curve is generated for each temperature. These DPSS curves almost coincide at two E_t values, one below and one above E_i . By generating the standard deviation of DPSS curves at each E_t , these two points can be extracted. This is done for k -DPSS curves and is shown in Fig. 2.4 (d). One of these two points is the correct solution for the investigated defect while the other solution is invalid. Two E_t values are found (one at each bandgap half) because of the symmetrical nature of the SRH equation around the E_t . It should be noted that only E_t and k are unique defect parameters since τ_{n0} is

affected by the defect density, meaning that it can change between samples with similar defects but different defect densities.

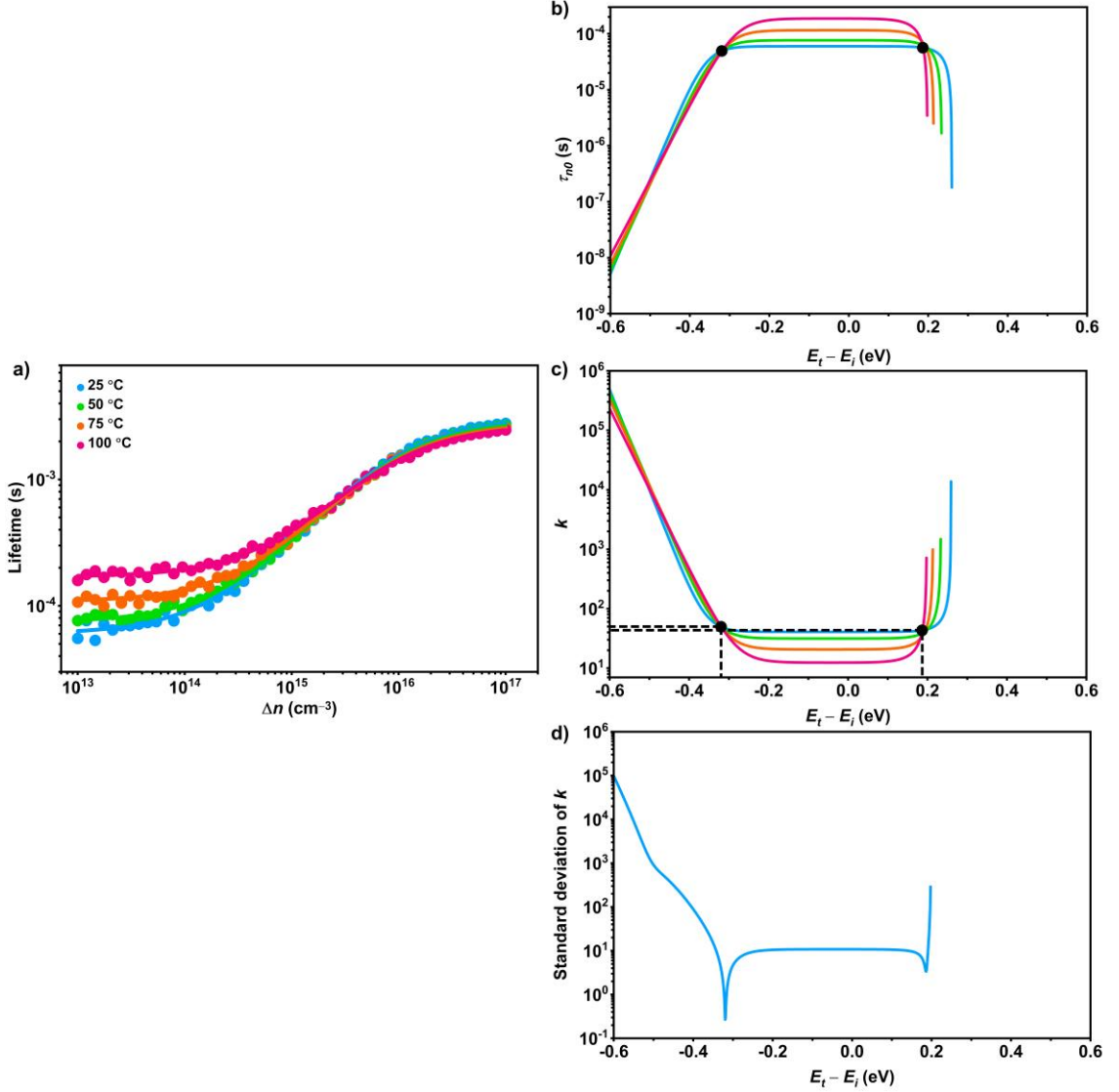


Fig. 2.4. (a) Simulated lifetime of a p -type wafer with $N_A = 1 \times 10^{16} \text{ cm}^{-3}$ at 25 °C to 100 °C temperature range (25 °C temperature intervals) with an SRH defect with $E_t - E_i = -0.32 \text{ eV}$, $k = 50$, $N_t = 1 \times 10^{13} \text{ cm}^{-3}$, and $\sigma_n = 1 \times 10^{-16} \text{ cm}^2$. The solid lines are the SRH lifetime fits. (b) The τ_{n0} -DPSS; and (c) k -DPSS curves for the simulated lifetime as well as; (d) the standard deviation of k -DPSS curves at each E_t .

Typically, the intersection of the DPSS curves generated from experimental data is diffused. One reason for this phenomenon is the presence of noise in the measured lifetime curves. Another possible reason is the temperature-dependence of capture cross-sections which can lead to the change of k with temperature. Thus, the actual k at each temperature is different. One method to overcome this problem is to measure different samples with the same defect but with different doping densities at the same temperature [41]. This method is called doping- and injection-dependent lifetime spectroscopy (N_{dop} -IDLS). Similar to the TIDLS measurement, by generating DPSS curves for each doping

concentration, the E_t and k of the defect are found. However, since samples with different doping concentrations are not always available, TIDLS measurement is a more viable option for the extraction of defect parameters.

While the fitting of lifetime curves with Eq. (2.13) is possible, doing that for numerous energy levels in the bandgap is quite time-consuming, even with current computation power. A method to simplify the fitting procedure is to linearize the lifetime curves by substituting Δn with the variable X ($X = n/p$) as the x -axis, and fit the linearized lifetime curves with a linear function in the form of [42]:

$$\tau_{SRH} = [\tau_{n0} + \frac{\tau_{p0}n_1}{p_0} + \frac{\tau_{n0}p}{p_0} + X(\tau_{p0} - \frac{\tau_{p0}n_1}{p_0} - \frac{\tau_{n0}p_1}{p_0})] \quad (2.29)$$

Thus, the SRH equation becomes a linear function, with the slope and intercept being a function of defect parameters. This linearization is done for the simulated lifetime data in Fig. 2.5 (a) and shown in Fig. 2.5 (b). It should be mentioned that besides changing the x -axis from Δn to X , the y -axis should also be presented in a linear form, in order to have a linear shape for the lifetime curve. Considering the linearized lifetime curve, it is now clear why defect parameters can not be extracted using a single lifetime curve. From each linearized lifetime curve, two parameters can be extracted (slope and intercept) while the SRH equation has three unknowns (E_t , k , τ_{n0}).

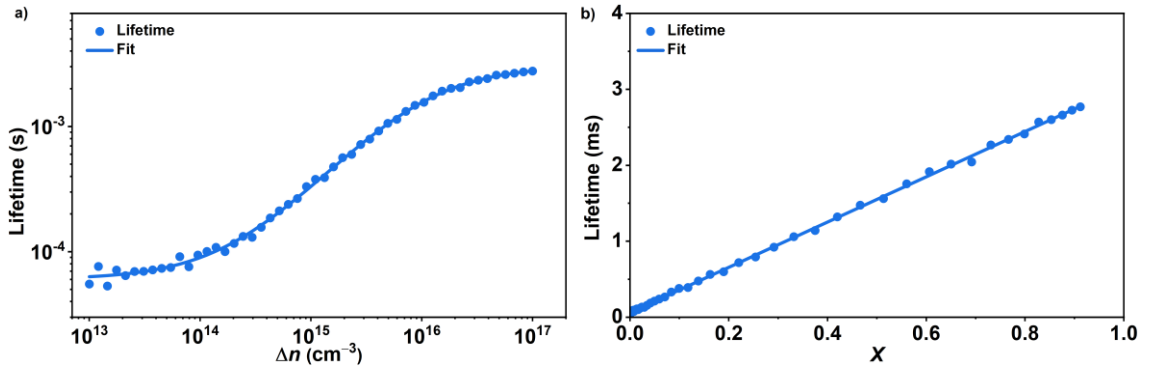


Fig. 2.5. Simulated lifetime (blue dots) of a p -type wafer with $N_A = 1 \times 10^{16} \text{ cm}^{-3}$ at 25°C with an SRH defect with $E_t - E_i = -0.32 \text{ eV}$, $k = 50$, $N_t = 10^{13} \text{ cm}^{-3}$, and $\sigma_n = 1 \times 10^{-16} \text{ cm}^2$ in the (a) standard; and (b) linearized form. The solid lines are the fits to the lifetime curves.

Another benefit of this linearization method is to differentiate between the lifetime curves of one single-level defect and multiple single-level defects (or a defect with multiple energy levels) [42]. In Fig. 2.6, the lifetime curves for two defects, as well as the combined lifetime of these defects, are presented. In the lifetime- Δn (standard) form of representation [see Fig. 2.6 (a)], it is not possible to discuss the number of defects

affecting the overall lifetime curve. However, in the linearized form [see Fig. 2.6 (b)], the non-linearity of the total lifetime suggests that this behavior can not be explained with one single-level defect.

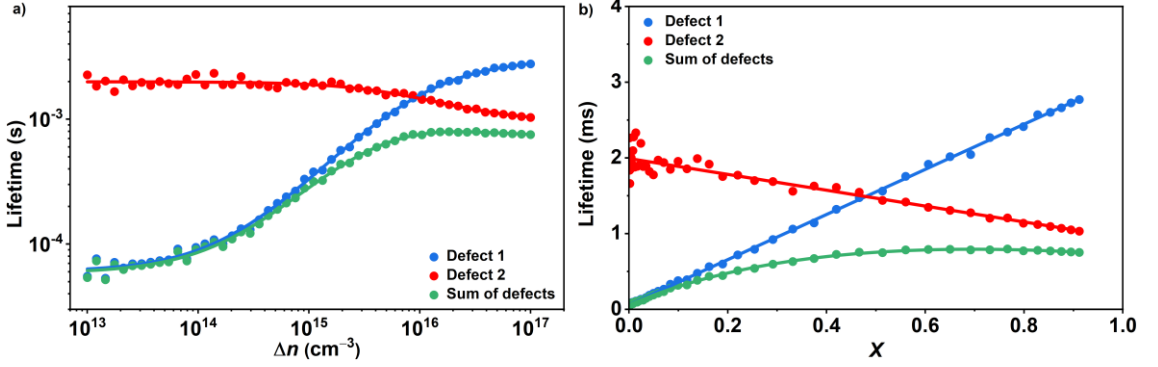


Fig. 2.6. Simulated lifetime of a *p*-type wafer with $N_A = 1 \times 10^{16} \text{ cm}^{-3}$ at 25 °C with two SRH defects with $E_t - E_i = -0.32 \text{ eV}$ and $k = 50$ (blue) and $E_t - E_i = 0.38 \text{ eV}$ and $k = 15$ (red) with $N_t = 10^{13} \text{ cm}^{-3}$, and $\sigma_n = 10^{-16} \text{ cm}^2$ and the combined lifetime (green) in the (a) standard; and (b) linearized form. The solid lines are the fits to the lifetime curves.

Until now, it is assumed that one defect is present in the sample and the τ_{SRH} for this defect is available for DPSS analysis. However, the measured lifetime is the τ_{eff} which is impacted by all of the recombination channels at the surface or in the bulk. Regarding the extraction of τ_{SRH} from τ_{eff} , two cases are possible:

1. The effective lifetime is dominated by the τ_{SRH} . In this case, $\tau_{eff} \approx \tau_{SRH}$ which means that τ_{eff} can be used directly for DPSS analysis.
2. Having two identical samples, one with the defect and one without the defect. By determining the harmonic difference of the measured lifetime from these two samples, the τ_{SRH} can be isolated:

$$\frac{1}{\tau_{eff}(\text{without_defect})} = \frac{1}{\tau_{surface}} + \frac{1}{\tau_{intrinsic}} + \frac{1}{\tau_{other}} \quad (2.30)$$

$$\frac{1}{\tau_{eff}(\text{with_defect})} = \frac{1}{\tau_{surface}} + \frac{1}{\tau_{intrinsic}} + \frac{1}{\tau_{SRH}} + \frac{1}{\tau_{other}} \quad (2.31)$$

where $\tau_{eff}(\text{without-defect})$ ($\tau_{eff}(\text{with-defect})$) is the effective lifetime in the sample without-defect (with-defect) and τ_{other} is the lifetime related to all other factors. It should be noted that the effect of all the other defects (except for the SRH defect being investigated) is considered in the τ_{other} term. For defects that are formed with processing steps like light-soaking, this harmonic difference can be calculated from the same sample by measuring the lifetime before and after the defect formation. In

this method, it is assumed that the other lifetime terms are the same in both samples or after the processing step.

In Chapter 5, based on the method described above, the TIDLS measurement method is used to investigate defects generated after light soaking of Ga-doped Cz wafers. For this purpose, PC-based lifetime measurement was used to extract the lifetime. However, PC-based measurement is not viable for the measurement of metalized cells, meaning that there are limitations to performing TIDLS measurement on complete solar cells. In Chapter 6, a method based on the Suns- V_{oc} measurement method is introduced to overcome this barrier and to extract the defect parameters directly from solar cells.

2.3 Minority carrier traps

Traps are defect centers that cause an artificially high PC signal in silicon wafers [43, 44]. Thus, traps can lead to artificially high lifetimes especially at low and medium injection levels when using PC-based lifetime measurements [45]. Traps are defects that are much more likely to capture minority carriers compared with majority carriers. These captured minority carriers are either: (1) emitted and re-captured several times until recombined with majority carriers (*fast* traps); (2) emitted and then recombined with majority carriers (*slow* traps); or (3) in limited cases, directly recombined through the trapping centers. Thus, the recombination is limited while the minority carriers are trapped and not available for recombination.

The artificial increase in lifetime due to traps can therefore be explained as excess majority carriers which are misinterpreted as excess minority carriers when the minority carriers are trapped [45]. It was mentioned in Section 2.1.5 that for the measurement of excess carrier concentration using the PC-based method, it is assumed that $\Delta n = \Delta p$. However, in a sample impacted by trapping, the excess majority carrier concentration is equal to the sum of the excess minority carriers and the excess trapped minority carriers. Hence, the PC can be written as (for a p -type sample):

$$\Delta\sigma = qw\Delta n(\mu_n + \mu_p) + qw\Delta n_t\mu_p \quad (2.32)$$

where Δn_t is the change in the density of trapped carriers due to the excitation. When affected by traps, the calculated excess carrier density is different from the actual excess carrier density and is termed as the apparent excess carrier density (Δn_{app}). It can be expressed using Eq. (2.21) assuming that $\Delta n_{app} = \Delta n = \Delta p$:

$$\Delta n_{app} = \frac{\Delta \sigma}{qw(\mu_n + \mu_p)} \quad (2.33)$$

Combining Eqs. (2.32) and (2.33), Δn_{app} can be calculated as:

$$\Delta n_{app} = \Delta n + \frac{\mu_p}{\mu_n + \mu_p} \Delta n_t \quad (2.34)$$

When Δn_t in Eq. (2.34) becomes comparable with Δn (commonly at low injection levels), the effect of traps on Δn_{app} becomes prominent and it leads to an overestimation of the actual Δn . It is for this reason that the high-injection range is chosen for the extraction of C_{PL} , as in this range, for a sample impacted by traps, $\Delta n \approx \Delta n_{app}$.

As mentioned before, traps are often divided into two types, slow traps and fast traps. Fast traps are defect centers with minority carrier capture rates faster than the total recombination rate in the wafers. In fast traps, multiple captures and emissions of carriers occur until the carriers are recombined [43, 45]. A schematic of these traps in a p -type sample is shown in Fig. 2.7. Immediately after the flash cut-off, most of the excess carriers recombine through recombination-active defects with an energy level denoted with E_t , while some of the excess carriers have interaction with traps with an energy level denoted with E_T [see Fig. 2.7 (a)]. As stated, these carriers are emitted and re-captured several times until they are recombined through the recombination-active defects [see Fig. 2.7 (b)]. It is also possible to have direct recombination through trapping centers by capturing holes in the traps, shown with a red dashed arrow. However, this is considered negligible in many cases [45] and the rate of these processes is much smaller than the recombination rate. Thus, the free majority carriers are not recombined for an extended period of time and are misinterpreted as minority carriers.

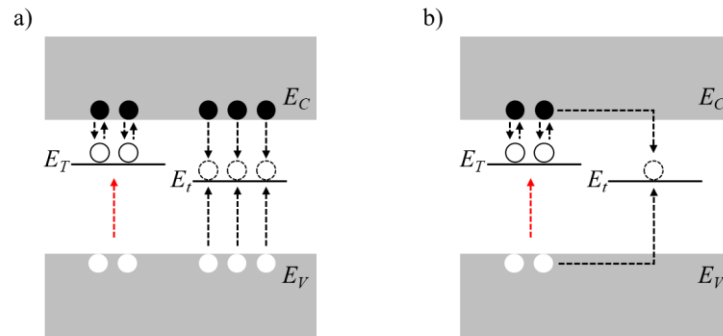


Fig. 2.7. Schematic of a fast trap in a p -type sample: (a) immediately after the flash cut-off; and (b) when most of the excess minority carriers are recombined.

On the other hand, slow traps are defect centers with negligible carrier re-capture and an emission rate slower than the total recombination rate [46]. A schematic of these traps for a p -type sample is shown in Fig. 2.8. Immediately after the flash cut-off, most of the carriers are recombined while some of the carriers are trapped in slow traps [see Fig. 2.8 (a)]. Filling of the traps occurs during the excitation, thus traps are already filled when the flash is turned off. The trapped carriers are then emitted at a rate much lower than the recombination rate, and these carriers are recombined through recombination channels such as recombination-active defects [46, 47]. Similar to fast traps, direct recombination through slow traps is possible but it is a less probable recombination path.

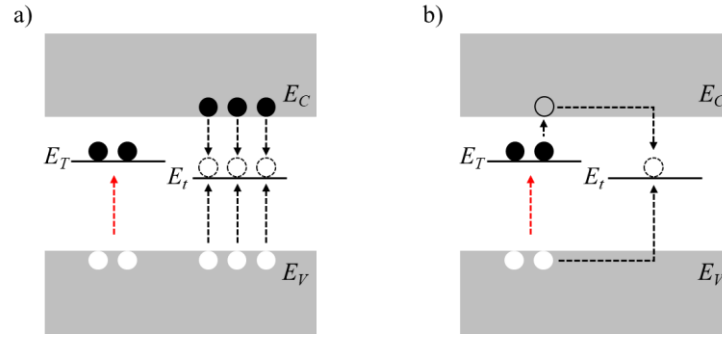


Fig. 2.8. Schematic of a slow trap in a p -type sample: (a) immediately after the flash cut-off; and (b) when most of the excess minority carriers are recombined.

Considering these descriptions, another difference between fast and slow traps becomes clear. In general, the probability of carrier re-capture increases as the number of empty traps increases. Since slow traps have negligible minority carrier re-capture, the rate that traps are emptied does not depend on the number of traps that are empty [46]. On the other hand, for the fast traps with a high probability of carrier re-capture, this means that re-capture probability increases with time after excitation (as more traps are emptied) [43]. Moreover, for a sample with a fast trap, since defects and traps are competing for the capture of minority carriers from the conduction band (in the case of p -type samples), changing the lifetime should cause a change in the rate that fast traps are emptied [44]. These two points will be used in the following chapters to identify the nature of observed traps.

For the investigation of traps in this thesis, PCD measurement is performed. To generate the lifetime curves, the change in the PC data is measured for several milliseconds after the flash. However, the PC measurement can be done for an extended period (several hundred seconds). In this time regime, the phenomena with a time

constant significantly larger than the lifetime dominate the PC. This measurement is referred to as the PCD measurement. The PCD measurement of a sample impacted by traps is shown in Fig. 2.9. The acquired data just after the flash (region “I”) is dominated by the recombination channels, thus, it is used to generate the lifetime curves and study the recombination-active defects. On the other hand, the prolonged PCD region (“II”) is dominated by the de-trapping rate of the traps, which mainly depends on the trap parameters as well as the temperature and doping. Thus, this region can be used for trap studies.

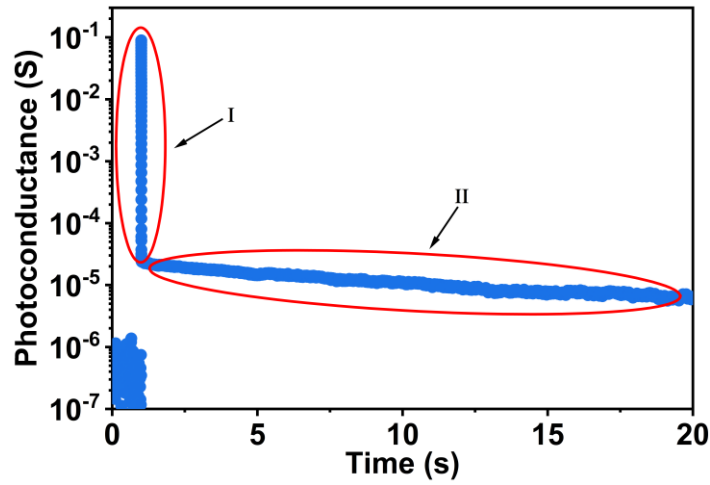


Fig. 2.9. PCD curve of a sample impacted by traps. The marked regions are the region used for the investigation of recombination-active defects (“I”) and the region used for the investigation of traps (“II”).

Aside from their impact on PC-based lifetime measurements, the physical origin of the traps can be of importance when investigating the electrical properties of silicon wafers. In Chapter 3, the possible connection between traps and defects in B-doped Cz silicon wafers is investigated. In Chapter 4, the traps in B-doped mc-Si wafers and their changes after various processing steps are studied, while in Chapter 5, traps in Ga-doped Cz wafers are investigated.

2.4 Light-induced degradation

LID is the reduction in the lifetime (degradation) of silicon wafers due to incident light. In this section, LID in three types of silicon wafers is reviewed. First, LID in B-doped Cz wafers is discussed. Then, light- and elevated temperature-induced degradation (LeTID) in mc-Si wafers is reviewed. Finally, literature regarding the investigation of LID in Ga- and In-doped Cz wafers is surveyed, suggesting that a decisive conclusion regarding the presence of LID in these wafers is not present.

2.4.1 LID in B-doped Cz silicon wafers

LID of solar cells fabricated using B-doped Cz-grown silicon wafers was first observed in 1973, showing a 3–5% absolute reduction in efficiency after illumination for 12 hours [48]. Since the degradation is linked to the simultaneous presence of B and oxygen (O) in the wafers, it is frequently called BO degradation [49, 50]. Studies of the minority carrier lifetime of uncompensated wafers with various boron concentrations ($[B]$) and interstitial oxygen concentrations ($[O_i]$) have shown that the inferred concentration of the BO defect, which is responsible for LID, has a linear dependency on the $[B]$ and a quadratic dependency on the $[O_i]$ [51, 52]. It was found that LID in B-doped float zone (FZ) silicon wafers is negligible unless they are implanted with O [53].

It has been argued that the complex causing BO-related degradation has three states: degraded state, annealed state, and stabilized state [52, 54]. A schematic of these three states is shown in Fig. 2.10. The degraded state is reached via minority carrier injection resulting from exposure to light or from a forward bias current in a solar cell's p - n junction for several hours [55–57]. After this carrier injection, the bulk lifetime is reduced due to the transformation of the BO defect “precursor” to the recombination-active BO defect [58]. The annealed state can be reached by dark annealing (DA) at elevated temperatures (typically around 200 °C) for several minutes. In this state, the recombination-active defects transform back to the precursor form of the BO complex which is non-recombination-active and does not affect the lifetime. However, this state is not stable and minority carrier injection reduces the lifetime again [59]. The stabilized state can be reached via carrier injection at elevated temperatures (around 200 °C) [54, 60]. At this state, the wafer is no longer prone to degradation under typical solar cell operating conditions. Nevertheless, this state is also metastable and can be transformed into the annealed state by a long DA at high temperatures (~ 200 °C) [60, 61].

Only a few studies directly investigated the precursor of the defect causing LID. In a recent study, a precursor of the recombination-active BO defect has been observed in boron-doped Cz silicon samples by means of deep level transient spectroscopy (DLTS) [62, 63]. A hole emission signal due to the BO defect in the annealed state was detected. The signal disappeared from the DLTS spectra after the degradation process [62]. It was argued by the authors that a trap is acting as a precursor for the recombination-active BO defect. Furthermore, it has been suggested that in the degraded state, the enhanced

recombination occurs due to a shallow acceptor defect level through a trap-assisted Auger recombination process [63]. A PC-based measurement for the investigation of defects in their non-recombination-active state is introduced in Chapter 3. With this method, the precursor of BO-related defects is further investigated.

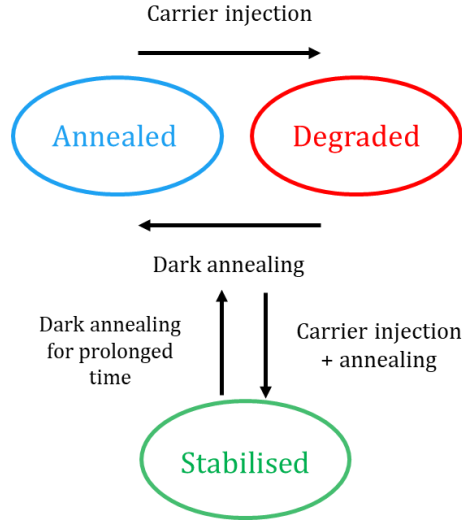


Fig. 2.10. Schematic of the BO-related defect states.

2.4.2 LeTID in *p*-type mc-Si wafers

LeTID in *p*-type mc-Si cells was first reported by Ramspeck *et al.* observing the degradation of cells at 75 °C under illumination [64]. It has been shown that this degradation can cause up to a 16% relative reduction in solar cell efficiency [65]. It was also shown that this degradation has a rate much smaller than LID degradation in B-doped Cz wafers [64]. This degradation was observed in Ga-doped mc-Si cells, suggesting that a BO-related defect is not the cause of the observed degradation [64]. It is also known that oxygen concentration in mc-Si wafers is much lower compared with Cz wafers [66, 67], further suggesting that the nature of LeTID-related and LID-related defects are different.

Several studies have been done to pinpoint the source of LeTID in mc-Si wafers. It has been suggested that a bulk (and not surface) defect is the cause of LeTID [68, 69]. Furthermore, it has been shown that firing is the key processing step for the observation of LeTID in cells and wafers [70]. Besides firing, the presence of a hydrogen-rich dielectric layer on the surface, such as hydrogenated silicon nitride (SiN_x:H) during the firing step is also crucial for the observation of this defect [69] and that the extent of degradation is correlated with hydrogen concentration [69, 71]. Thus, it can be suggested

that while hydrogen is necessary for the formation of this defect, the firing process is needed to diffuse the hydrogen from the dielectric layer to the bulk. To demonstrate this, the evolution of the lifetime of a fired and unfired p -type mc-Si sample as a function of light soaking duration at 0.5 suns and 120 °C is shown in Fig. 2.11 [72].

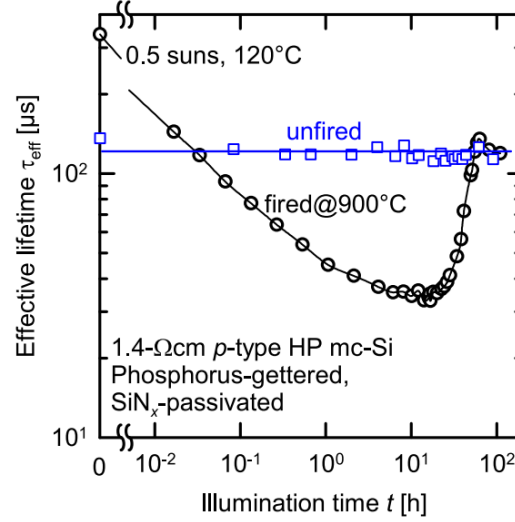


Fig. 2.11. Evolution of lifetime as a function of light-soaking duration at 0.5 suns and 120 °C for fired and unfired p -type mc-Si samples.[72].

It is suggested that the LeTID-related defects have three states [73]. These states are named annealed, degraded, and regenerated states [74]. From the annealed state, by carrier injection at high temperatures, the defects are formed and the lifetime of the sample is dropped, reaching the degraded state. With further illumination at high temperature, the lifetime is recovered, reaching the regenerated state. In the first transition (annealed state to degraded state), regeneration also occurs in parallel with degradation. Further high-temperature illumination after full regeneration does not lead to any more degradation, suggesting that the sample is no longer prone to LeTID. However, this state is metastable and with annealing at 200 °C for 10 min, the defect returns to the annealed state and is again susceptible to LeTID [74]. A four-state kinetic model was also suggested for LeTID-related defects [75]. It has been shown that the extent of LeTID decreases rapidly after consecutive LeTID-DA cycles, suggesting that defects are passivated permanently with prolonged illumination and defect precursors are released from a reservoir state with DA [75]. The schematic of this four-state model is presented in Fig. 2.12 [75].

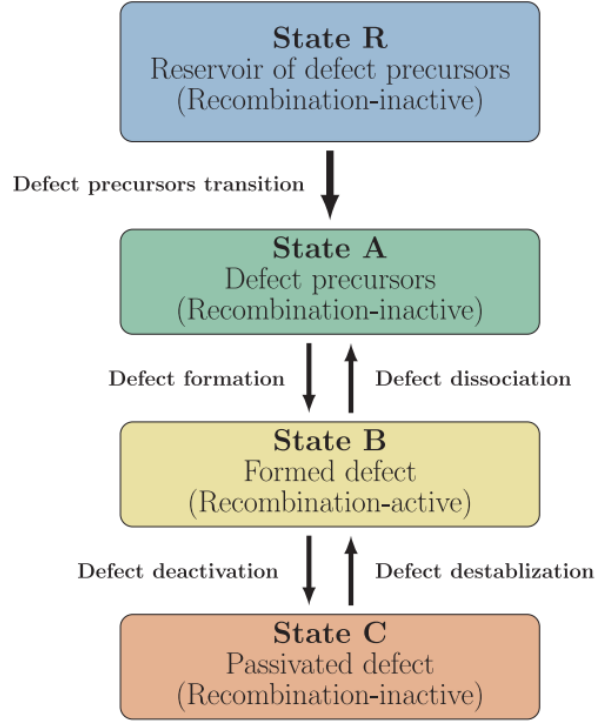


Fig. 2.12. Schematic of the four-state model for the LeTID-related defect states [75].

In Chapter 4, the change in traps after LeTID-related processing steps (firing, high-temperature illumination, and DA) is investigated and the possible connection between traps and LeTID-related defects is studied.

2.4.3 LID in Ga- and In-doped Cz silicon wafers

As discussed in Section 2.4.1, LID in Cz silicon wafers is due to the simultaneous presence of B and O in the bulk of the wafer. Thus, one of the possible solutions to prevent the negative impact of LID on cell efficiencies is to substitute boron with other dopants from Group III, such as aluminum (Al), Ga, or In. The strong recombination activity of the Al-O pair in Cz silicon makes Al a less viable option [76]. However, both Ga and In have been investigated as dopants to produce industrial *p*-type silicon [77, 78]. Ga has a segregation coefficient of 8×10^{-3} and ionization energy of 0.065 eV, while the values for In are 4×10^{-4} and 0.156 eV, respectively [79, 80]. Since a higher segregation coefficient leads to a better uniformity of doping throughout the ingot and as lower ionization energy results in a lower resistivity at the operating temperatures, Ga is preferred over In. Hence, the industry has shifted towards Ga-doped wafers as the best-available solution to solve the LID problem [81].

Previous studies regarding LID in Ga-doped Cz wafers are not conclusive. Some investigations have suggested negligible or no LID in Ga-doped wafers [78, 82]. However, other studies reported degradation after light soaking [83, 84]. It is suggested that the extent of LID in Ga-doped wafers is lower than in B-doped wafers and occurs over longer time scales [83]. It is shown that the firing step is essential to observe LID in Ga-doped silicon wafers [85]. Furthermore, it has been shown that LID behavior depends on the injection level during illumination [86]. While under 1-sun illumination at 75 °C no significant degradation was observed, under 0.1-sun illumination at the same temperature the samples were degraded [86].

The conclusions regarding the presence of LID in In-doped Cz silicon are also divided. Some studies reported LID in In-doped wafers [87], while in others, no degradation has been observed under light soaking [88]. In Chapter 5, LID in Ga- and In-doped Cz wafers will be discussed, with Ga-doped wafers being the primary focus for its greater commercial potential.

2.5 Chapter summary

In this chapter, the basic concepts of recombination mechanisms and lifetime were presented. A method for defect characterization, based on TIDLS measurements and the generation of DPSS curves was discussed. It was shown that measurements at various temperatures are needed in order to extract the parameters of lifetime-limiting defects. This method is utilized in Chapter 5 to investigate the LID-related defects in Ga-doped Cz wafers. An extension of this method (based on Suns- V_{oc} measurement) for the extraction of defect parameters from metalized solar cells is discussed in Chapter 6.

The impact of traps on PC-based measurements was discussed and the two types of traps were briefly introduced. The investigation of traps in B-doped Cz, B-doped mc-Si, and Ga-doped Cz wafers is presented in Chapter 3, Chapter 4, and Chapter 5.

Finally, a brief review of LID in B-doped Cz, LeTID in *p*-type mc-Si, and LID in Ga- and In-doped Cz wafers was presented in preparation for further discussion in the following chapters.

Chapter 3

Investigation of Traps in Boron-Doped Czochralski Silicon¹

Traps are a source of artificially high lifetime values at low injection levels when using PC-based lifetime measurement methods. Although both traps and lifetime limiting defects are present in the bulk of silicon wafers, investigations regarding the possible connection between them have only been done in very few studies.

In this chapter, a method based on PCD measurements is introduced to investigate the traps acting as the precursor of BO-related defects. In Section 3.1, previous findings regarding traps in B-doped Cz wafers are reviewed. In Section 3.2, details regarding the measurement and analysis methods are presented. In Section 3.3, the findings regarding the BO-related traps are presented and discussed. First, the trapping effect in B-doped Cz silicon wafers in the annealed and degraded states is investigated using PCD measurements. Then, the change in the trap density and the density of BO-related defects after various degradation extents are compared. Finally, doping- and temperature-dependent measurements are done to further investigate the trap.

3.1 Traps in B-doped Cz silicon

Hornbeck and Haynes investigated traps in *p*-type B-doped Cz silicon wafers using the PCD measurement method [43]. Two types of traps were detected, one leading to a relatively small PCD time constant (milliseconds) and the other leading to a large (tens

¹ This chapter is partially based on:

S. Jafari, Y. Zhu, F. E. Rougieux, J. T. Du Guzman, V. P. Markevich, A. R. Peaker, and Z. Hameiri, in *47th IEEE Photovoltaics Specialists Conference (PVSC)*, 2020. (Won the Best Student Award)

S. Jafari, Y. Zhu, F. E. Rougieux, J. T. Du Guzman, V. P. Markevich, A. R. Peaker, and Z. Hameiri, in *Asia-Pacific Solar Research Conference (APSRC)*, 2020.

S. Jafari, Y. Zhu, F. E. Rougieux, J. T. Du Guzman, V. P. Markevich, A. R. Peaker, and Z. Hameiri, "On the correlation between light-induced degradation and minority carrier traps in boron-doped Czochralski silicon", *ACS Appl. Mater. Interfaces*, vol. 13, pp. 6140-6146, 2021.

of seconds) time constant. In a study by Schmidt *et al.*, lifetime measurements were used to study traps in B- and Ga-doped Cz silicon wafers [89]. The authors found a correlation between the trap density and $[O_i]$ and suggested that this trap might be correlated with oxygen-related thermal double donors (TDDs). Furthermore, it has been argued that the origin of the trapping centers in their study is probably not identical to the LID-related recombination centers [89]. In a recent study, a precursor of the recombination-active BO-related defects has been observed in B-doped Cz silicon samples by means of DLTS [62, 63]. A hole emission signal due to the BO-related defects in the annealed state was detected. The signal disappeared from the DLTS spectra after the degradation process [62]. It was argued by the authors, that a minority carrier trap is acting as a precursor for the recombination-active BO-related defect [63]. Furthermore, it has been suggested that this BO-related defect is a shallow acceptor defect level with a trap-assisted Auger recombination process [63]. In the following sections, using the PCD measurement method, the presence of traps in B-doped Cz wafers that act as the precursors of the BO-related defects is investigated.

3.2 Materials and methods

Three sets of B-doped Cz silicon wafers with resistivities of $1.30 \pm 0.05 \, \Omega \cdot \text{cm}$ (Set 1), $0.70 \pm 0.02 \, \Omega \cdot \text{cm}$ (Set 2), and $2.01 \pm 0.05 \, \Omega \cdot \text{cm}$ (Set 3) are used in this chapter. All wafers were gettered using phosphorous (P)-diffusion process at $840 \, ^\circ\text{C}$ for 45 min, followed by removal of the diffused layer using a hydrofluoric acid (HF)-nitric acid (HNO_3) solution with a volumetric ratio of 1:10. Samples were then subjected to rapid thermal annealing (peak temperature of $800 \, ^\circ\text{C}$ for 10 sec with a heating rate of $50 \, ^\circ\text{C}/\text{sec}$) to remove TDDs [47]. The $[O_i]$ was then measured using Fourier transform infrared spectroscopy (FTIR) measurement based on the ASTM standard (designations “F1188” and “F1391”) which was modified by A. K. Søliland for thin silicon wafers [90, 91]. The $[O_i]$ was measured to be $7 \times 10^{17} \, \text{cm}^{-3}$ for wafers from Sets 1 and 3 and $8 \times 10^{17} \, \text{cm}^{-3}$ for wafers from Set 2. Samples were then passivated with a 10 nm aluminum oxide (AlO_x) layer using atomic layer deposition (ALD) and capped with a 75 nm silicon nitride (SiN_x) layer (refractive index of 2.08 at 632 nm) deposited using plasma-enhanced chemical vapor deposition (PECVD) [92]. Annealing at $400 \, ^\circ\text{C}$ for 30 min was done after AlO_x deposition (before SiN_x deposition) to activate the surface passivation. The selected surface passivation methods are known to have only a minor impact on the hydrogen content in the bulk [93]. When required, the passivation was etched off using a 5% HF solution.

For the degradation of the samples, two different methods were selected. Samples from Sets 2 and 3 and several samples from Set 1 were degraded at 120 °C using 938 nm laser illumination (96 suns intensity). This method provides a fast degradation rate [94]. The second group of samples from Set 1 were degraded at 60 °C using a set of halogen lamps with a combined intensity of 1 sun. The degradation extent was monitored using PC-based lifetime measurements (WCT-120 from Sinton Instruments). To return the samples to their initial lifetime (annealed state), they were dark annealed at 200 °C for 15 min. Note that the reported temperatures are the actual *sample* temperatures and not the *set* temperatures, determined by direct measurements of a monitor sample using k-type thermocouples. For this purpose, two wire thermocouples (CHAL-005 OMEGA) were attached to a sample from the same set (undergone similar processing steps) using Kapton tape, and the reported temperature is the average of the measured temperatures.

For the PC and PL measurements, a modified system based on WCT-120 lifetime tester is used. A schematic of this system is shown in Fig. 3.1. Three types of illumination sources are integrated into this system: a flash, a light emitting diode (LED, 810 nm), and a Laser (808 nm). The illumination sources used throughout this thesis are the flash and the LED. The flash is similar to the flash used in WCT-120 system (X5DR flash model from Quantum instruments). With this flash, two modes of excitation are possible. The first one is referred to as the QSS flash (TTL mode) which has a decay time constant of around 2.3 ms. The second mode is denoted as the transient flash (1/64 mode) with a decay time constant of around 35 μ s. The profiles of both illumination conditions are presented in Fig. 3.2. To measure the photon flux of the flash, a calibrated reference cell is used, located in the stage. For the LED, the generation profile can be modified based on the measurement condition. For the measurement of the photon flux of the LED, a beam splitter is placed in front of the LED and a known portion of the emitted photons is detected with a reference photodiode. With the flash, it is possible to generate an illumination intensity of ~ 50 suns while with the LED, the maximum illumination intensity is ~ 10 suns.

For PC measurements, a long pass filter is used in front of the flash to cut off the low wavelength region of the flash spectrum. Thus, a more uniform generation profile is achieved with this filter [95]. However, this filter is not suitable for PL measurements as it will result in an interference between the excitation signal and the PL signal. Consequently, for PL measurements, a KG3 filter is used in front of the flash to cut off

the long-wavelength part of the flash. Besides the reference cell, the temperature stage, PC coil, and PL detector are also located in the stage. The sample is placed on the temperature stage, on top of the PC coil. A quartz window is placed in the middle of the lid (on top of the sample) so that the illumination beam reaches the sample. Moreover, there is a quartz window beneath the sample as well, which allows the emitted PL from the sample to reach the PL detector.

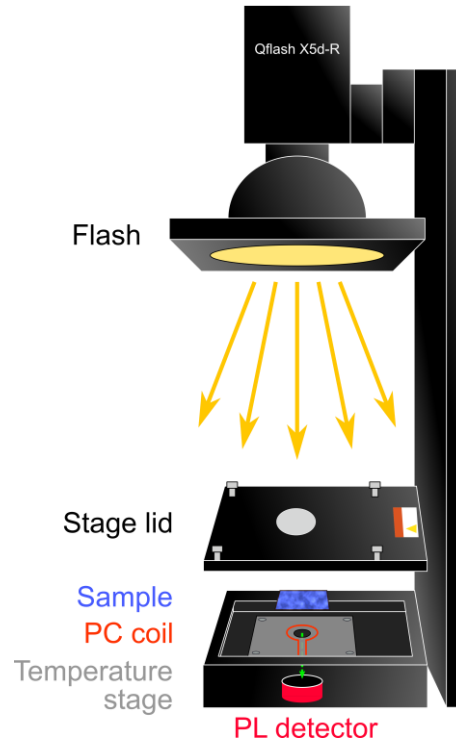


Fig. 3.1. Schematic of the modified temperature-dependent PC and PL measurement system.

With this system, it is possible to perform PC- and PL-based measurements simultaneously in the $-193\text{ }^{\circ}\text{C}$ to $400\text{ }^{\circ}\text{C}$ temperature range [96, 97]. The heating element is inside the temperature stage while the liquid nitrogen cooling system is connected to the temperature stage for sub-room temperature measurements. Due to the thermal resistivity of the sample, the stage (set) temperature and sample temperature are not identical. To measure the actual sample temperature, two k-type thermocouples are attached to a sample similar to the measured sample. Then, the sample temperature is extracted from the average of both values at each set temperature. It should be noted that the reported measurement temperatures throughout the thesis are the set temperatures, while for analysis purposes, the sample temperatures are used.

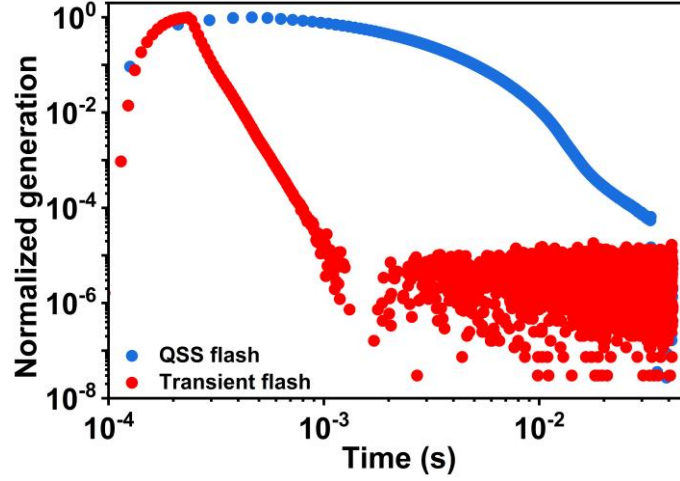


Fig. 3.2. Decay profile of the QSS and transient flash modes.

PCD measurements were carried out at 45 °C using this advanced lifetime tester. Fitting of the PCD curves was done using a mono-exponential decay function in the form of:

$$\Delta\sigma = A \cdot \exp\left(\frac{-t}{\tau_{decay}}\right) \quad (3.1)$$

where A is the pre-exponential factor and it is proportional (for these samples) to the number of filled traps after the flash (see Section 3.3.2), and τ_{decay} is the PCD time constant.

To improve the signal-to-noise ratio (SNR), 500 PCD measurements were averaged to generate each PCD graph. Furthermore, the measurement temperature was selected with the consideration of measurement duration and SNR. For the averaging, sufficient time between two consecutive excitations is needed to ensure the traps are almost empty (> 98% of unfilled traps are empty) before the next excitation (see Section 3.3.1). Considering this point, Fig. 3.3 highlights the reason behind the choice of measurement temperature. The graph presents the PCD curves of a representative sample from Set 1, measured at 25 °C and 45 °C with similar averaging counts. While the PCD time constant of the sample at 25 °C is 30.9 sec, it is 15.4 sec at 45 °C. Thus, when conducting the measurement at 25 °C, double the time is needed to reach the same percentage of empty traps after the excitation. This means that to have sufficiently empty traps, every measurement at 25 °C will take twice the time of the measurement at 45 °C. Thus, considering the high averaging counts, an increase in the measurement temperature significantly reduces the total measurement duration. However, on the negative side,

increasing the measurement temperature to higher values results in a reduction in conductance which in turn leads to lower signal and higher noise in the measurement. This can be due to a possible decrease in the number of trapped carriers at higher temperatures or the decrease in mobility with increasing temperature, which both result in a lower conductivity [98]. The effect of low conductance is partially visible in Fig. 3.3 in the measurement at 45 °C around $t = 20$ sec. Thus, with further increases in the measurement temperature, higher averaging counts are needed to overcome this noise which leads to an increase in the total measurement duration in comparison to the measurement at 45 °C. As a result, 45 °C was chosen as the optimal measurement temperature.

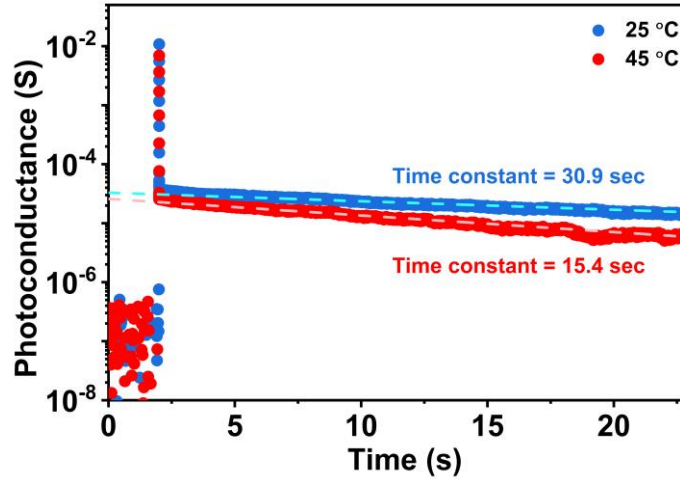


Fig. 3.3. PCD curves measured at 25 °C and 45 °C of a sample from Set 1. Each PCD curve is generated from an average of 500 measurements. The dashed lines are mono-exponential fits to the curves.

For excitation, the flash was used in the 1/64 mode, with a decay time constant of around 35 μ s. This flash mode was selected to minimize the possible measurement-induced degradation, as the flash has a much shorter decay in this mode compared with the TTL mode. To further confirm the stability of the lifetime during the PCD measurements, lifetime measurements at 30 °C (using the same system under QSS conditions) were done before and after each of the PCD measurements.

To monitor the extent of degradation, the normalized defect density (NDD) of the recombination-active BO-related defect was calculated using:

$$NDD = \left(\frac{1}{\tau_{deg(t)}} - \frac{1}{\tau_{DA}} \right) / \left(\frac{1}{\tau_{deg(8h)}} - \frac{1}{\tau_{DA}} \right) \quad (3.2)$$

where $\tau_{deg(t)}$ is the effective lifetime after light soaking for t minutes and τ_{DA} is the effective lifetime after DA. The denominator is the harmonic difference between the lifetimes in the degraded state (light soaking with halogen lamps for eight hours at 60 °C) and the annealed state. All the values are given at Δn of $1.1 \times 10^{15} \text{ cm}^{-3}$ ($0.1 \times N_A$).

3.3 Results and discussion

3.3.1 Presence of traps in the annealed state

In Fig. 3.4 (a), the lifetime curves of a representative sample from Set 1 (at 30 °C) in the annealed and degraded (with the laser-based process) states are shown. The lifetime of the sample is measured after a series of processes: DA, degradation, DA, degradation, and final DA. As expected, the effective lifetime in the annealed state is higher than the effective lifetime after the degradation process. Cycling the sample between the two states (annealed and degraded) results in a shift between the two lifetime curves. In Fig. 3.4 (b), the PCD curves (at 45 °C) for the same sample after each process are presented. Interestingly, the transformation between the two states strongly matches a change in the PCD curves. These curves show that the PC signal increases significantly after the excitation by the flash due to external carrier generation. After this increase, the PC drops considerably due to carrier recombination (marked as “I”). In the annealed state, this initial decrease in the PC is followed by a much slower second decay with a time constant of several seconds (marked as “II”). However, for samples in the degraded state (where the BO-related defects are already formed), the initial decay due to carrier recombination continues until the PC signal returns to its value in the dark, which is within the range of the noise level of the system (marked as “III”).

A possible cause for such long decays is the depletion region modulation (DRM) effect [99]. In silicon samples passivated by layers with a fixed charge similar to the bulk, a depletion region can be formed [100]. With illumination, the thickness of this depletion region decreases (modulates) due to the photo-generated carriers. After the illumination, the stored carriers near the depletion region generate an artificially high conductance which is interpreted as a high lifetime [100]. However, since the investigated samples (p -type wafers) are passivated with a negatively charged dielectric, the long decays cannot be explained by DRM [99, 100]. Thus, it appears that this decay is indeed due to the presence of minority carrier traps in the annealed state. The absence of the long PCD tail

in the degraded state indicates that the traps that exist in the annealed state are removed due to degradation. Moreover, as it is shown in Fig. 3.4 (b), this transformation is reversible. In accordance with the change in lifetime, the traps are formed and annihilated (reduced to less than 5% of their initial density) during the DA-degradation cycles.

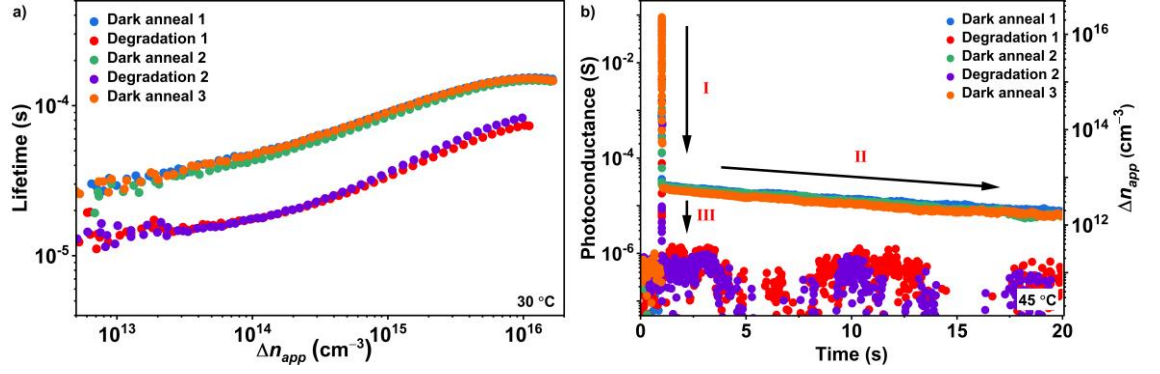


Fig. 3.4. (a) QSSPC lifetime curves measured at 30 °C; and (b) PCD curves measured at 45 °C of a sample from Set 1 cycled between DA and degradation steps.

To verify that the surface passivation quality does not change during the processing steps (DA and degradation), the lifetime of a *p*-type FZ sample (which is known to have a high bulk lifetime) processed identically to Sets 1–3 was measured during laser illumination-DA cycles (see Fig. 3.5). The changes in the measured lifetime at Δn of $1 \times 10^{15} cm^{-3}$ are below 3%. Considering that the lifetime of this sample is significantly higher than the samples in Set 1, it is concluded that the surface passivation is stable under these conditions.

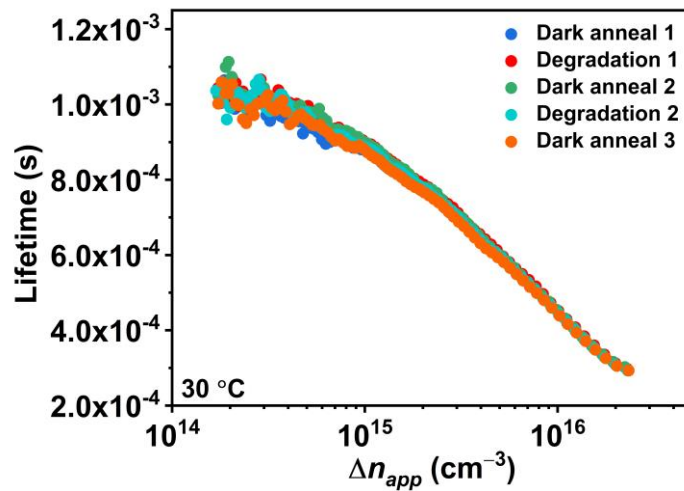


Fig. 3.5. QSSPC lifetime curves measured at 30 °C of a B-doped FZ sample cycled between DA and degradation steps.

The slow decay of the PCD in the annealed state (Region II) is linear (on a log scale), suggesting a mono-exponential decay of the PC signal. It has been shown previously that *fast* traps cannot be fitted with a simple exponential function (with a time-independent

time constant) while *slow* traps can be fitted with such an equation [43, 46]. Thus, it can be suggested that this trap is a *slow* trap. By fitting this section of the curve with Eq. (3.1), the average decay time constant is determined to be 15.9 ± 0.8 sec at 45 °C for the samples from Set 1.

As shown in Fig. 3.4 (a), the trapping effect is not observable in the lifetime curves of this sample, meaning $\Delta n = \Delta n_{app}$ for the range of excess minority carriers shown in this figure. This can be explained in two ways:

1. The trap density is too small to be detected in the common lifetime measurement range. Using constant electron and hole mobility values, Δn_{app} is calculated and displayed on the right y-axis of Fig. 3.4 (b) [101]. An error less than 10% in Δn_{app} due to the simplification of mobility (constant mobility assumption) is estimated, even at the highest injection level. As can be seen, the traps are noticeable only for Δn_{app} below $1 \times 10^{13} \text{ cm}^{-3}$, a region where common lifetime measurements suffer from a high level of noise.
2. Due to the ambient light or short waiting time between consecutive flashes, a considerable portion of traps is still occupied during the following measurement. For instance, the lifetime of the investigated samples is obtained by averaging 10 measurements with 15 sec between consecutive flashes. Considering a PCD time constant of 29 sec at 30 °C (note that the value used in Fig. 3.3 is at 25 °C), almost 60% of the traps are still occupied when the second measurement starts. These occupied traps will be considered as the dark conductance (background) for the following measurements and will be removed by subtraction. In Fig. 3.6, a representation of this effect for a sample from Set 1 measured at 45 °C is shown. As discussed, after the flash, a sudden drop in PC is observed due to the recombination through different channels. This is followed by a slow decay which corresponds to the de-trapping phenomenon. However, when the time between the excitations is only 13 sec, $2.6 \times 10^{12} \text{ cm}^{-3}$ apparent carriers are still present and the conductance generated due to these carriers is considered as the background conductance for the next measurement. As a result, the impact of traps on lifetime curves will be shifted to a lower injection range ($2.6 \times 10^{12} \text{ cm}^{-3}$ lower). Thus, for trap investigation, it is important to wait for a sufficiently long time between flashes so the traps are empty before the next measurement. To make sure that less than 1% of traps are filled before the next excitation, for a trap with mono-exponential decay, a time equal to five times

the PCD time constant should be given between consecutive excitations. It should be mentioned that this effect is not cumulative, meaning that the number of residual filled traps after each excitation is constant and the number of filled traps does not increase with averaging.

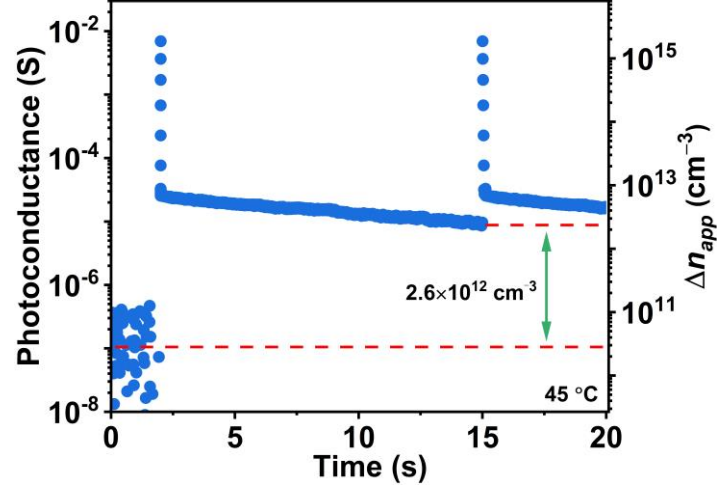


Fig. 3.6. A representation of two consecutive PCD curves measured at 45 °C with 13 sec between excitations of a sample from Set 1.

Impact of TDDs on the PCD curves

It is important to note that the observed trapping effect (persistent PC signal) is not related to TDDs as they were removed in all Set 1 wafers via a TDDs annihilation step. In fact, the removal of TDDs has a significant impact on the decay shape and time constant of PCD curves. In the samples from Set 3 which were not subjected to the TDDs removal step, another trap is observed. In Fig. 3.7, the PCD curves in the annealed and degraded states before TDDs removal of a representative sample from Set 3 are presented. Before the degradation process, the PCD curve exhibits two slopes (marked as “I” and “II”), one presumably related to the BO (“I”) and the other related to the TDDs (“II”). However, the signal corresponding to the trap with the smaller τ_{decay} is removed after degradation. Removing TDDs using the previously mentioned process also removes the second slope, associated with the TDDs.

It is also noted that the time constant of the BO-related trap in the sample with TDDs is smaller than the value extracted from the same sample without TDDs. In Fig. 3.8 (a), the PCD curve of a sample from Set 3 before removing TDDs is presented. Fitting the curve with a two-exponential function (τ_{decay1} and τ_{decay2}), the extracted time constants are 5.0 ± 0.1 sec and 156 ± 7 sec for the BO-related trap and TDD-related trap, respectively. However, fitting only the yellow region in this curve, which corresponds to the BO-

related trap, a time constant of 9.2 ± 0.2 sec is extracted. In Fig. 3.8 (b) the PCD curve of a sample from the same set, after removing TDDs is presented. The extracted PCD time constant from this curve is 17.0 ± 0.2 sec, suggesting that the removal of TDDs is crucial for the correct assessment of the traps. These values are also summarized in Table 3.1.

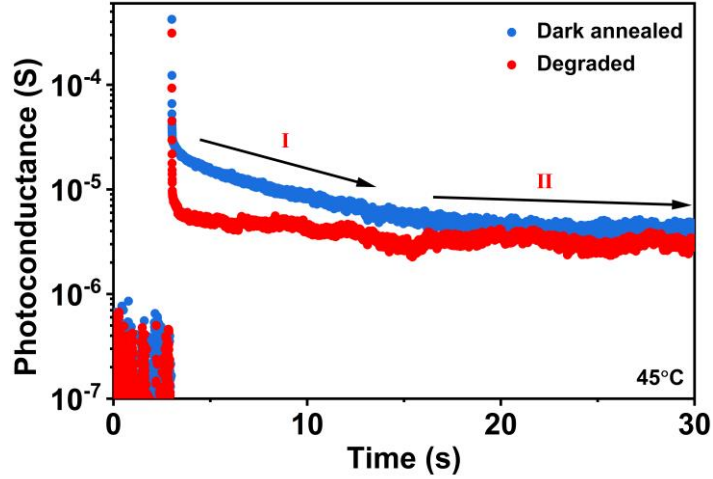


Fig. 3.7. PCD curves measured at 45 °C of a sample from Set 3 with TDDs after DA and after degradation.

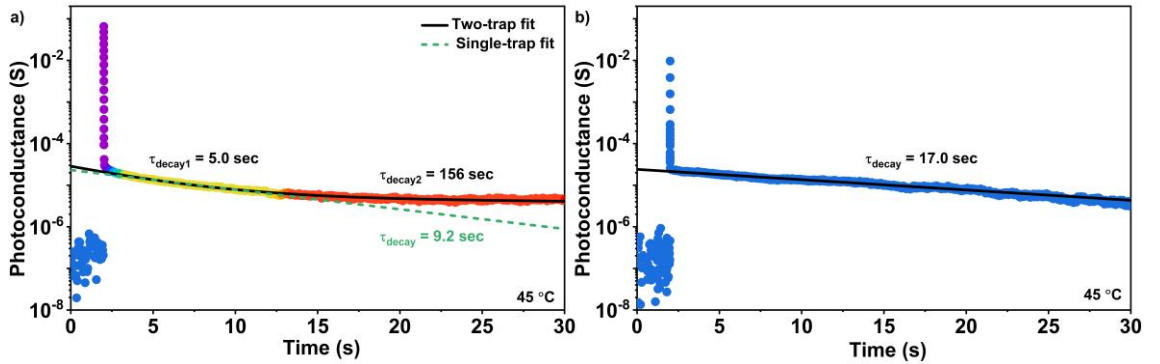


Fig. 3.8. PCD curves measured at 45 °C of two samples from Set 3: (a) with TDDs; and (b) without TDDs. The solid line in (a) is a double-exponential fit. The dashed line in (a) and the solid line in (b) are single-exponential fits.

When fitting the PCD curve in Fig. 3.8 (a) with a double-exponential function, the lower time constant can be due to the presence of more than two traps before removing TDDs. In the case of fitting the curve with a single-exponential function, simultaneous de-trapping of both traps can result in a shorter PCD time constant. Since the PCD (in the de-trapping region) is a measure of the density of majority carriers in the majority carrier band, having two de-trapping processes will lead to faster removal of majority carriers. This, in turn, results in a faster decay of the PC with time. Another important factor in the reported time constant in this case is the chosen data range for the fitting. This observation confirms the importance of TDDs removal for accurate measurement of BO-related traps.

Moreover, this result agrees with the suggestion by Schmidt *et al.* that the traps detected in their O-rich Cz silicon wafers can be possibly related to TDDs [89].

Table 3.1. PCD time constants for samples with and without TDDs fitted with single- and double-exponential decay functions.

Sample	Fitting equation	Decay time constant (s)	
Without TDDs	Single-exponential decay	17.0±0.2	
	Single-exponential decay	9.2±0.2	
With TDDs	Double-exponential decay	τ_{decay1}	τ_{decay2}
		5.0±0.1	156±7

PCD measurements of B-doped FZ and P-doped Cz silicon wafers

As stated, it has been shown that LID in B-doped Cz silicon wafers is connected to the simultaneous presence of B and O in the samples [48, 49]. Thus, if the observed trap is correlated with the BO-related defect, it should not be present in B-doped FZ and P-doped Cz silicon wafers. To check this, two additional sets of wafers were prepared. The first set is B-doped FZ wafers with a resistivity of $0.28 \pm 0.02 \, \Omega \cdot \text{cm}$ and $[\text{O}_i] < 2 \times 10^{16} \, \text{cm}^{-3}$, while the second set is P-doped Cz wafers with a resistivity of $8.2 \pm 0.1 \, \Omega \cdot \text{cm}$ and $[\text{O}_i]$ of $5.4 \times 10^{17} \, \text{cm}^{-3}$. These wafers have gone through the exact same processing steps as Sets 1–3 and the measurements are done following the same procedure. In Fig. 3.9, the PCD curves of representative samples from each set after the DA process are presented. Similar PCD behavior is observed in both cases. The PC signal increases after excitation and drops due to carrier recombination. However, unlike the dark annealed B-doped Cz samples, no apparent slow decay is observable for these two samples. This result further confirms the connection between BO-related defects and the measured traps in B-doped Cz samples.

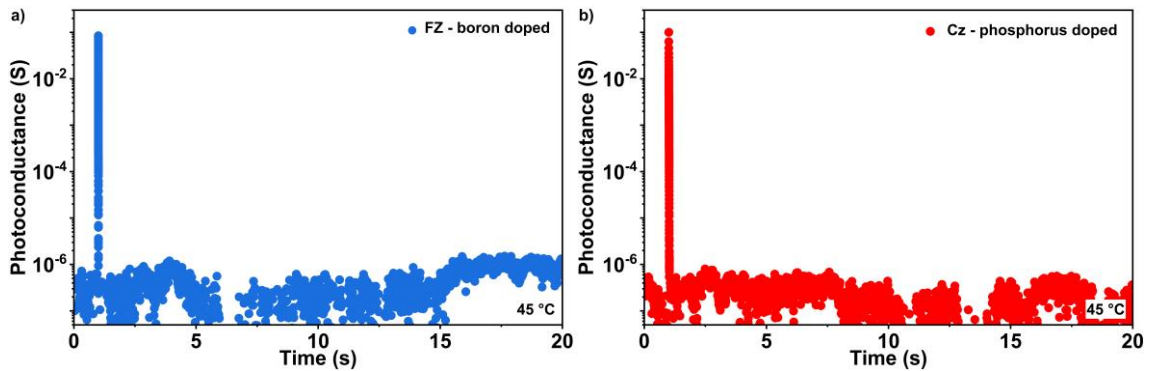


Fig. 3.9. PCD curves measured at 45 °C of dark annealed samples: (a) B-doped FZ wafers; and (b) P-doped Cz wafers.

3.3.2 Correlation between trap density and defect density

The change in trap density and the NDD after partial degradation was investigated to determine whether the trap is related to the recombination-active BO-related defects, or whether its change during the DA-degradation cycle is coincidental. The defect's density is extracted from the lifetime curve using the NDD metric [Eq. (3.2)]. For the trap, it is assumed that the normalized trap density (NTD) is proportional to A of Eq. (3.1). As it is shown in Fig. 3.10, A is extracted by fitting the PCD curve with Eq. (3.1) and finding the intercept of the y-axis at $t = t_{excitation}$ (excitation time).

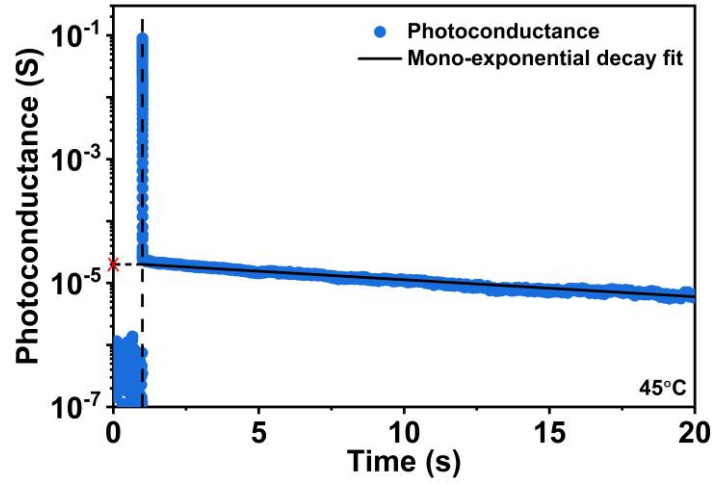


Fig. 3.10. PCD curve measured at 45 °C of a sample from Set 1 after DA. The solid line is a mono-exponential fit to the curve. The “X” marks the extracted pre-exponent value from the fit.

The assumption that the trap density is proportional to A first needs to be verified. At injection levels where $\Delta n_i > \Delta n$:

$$\Delta\sigma = qw(\mu_p\Delta n_t) \quad (3.3)$$

At $t = 0$, Δn_i is proportional to A . The pre-exponential factor is a measure of the density of traps that are filled after excitation. The density of filled traps is a function of the trap occupancy ratio (f_i) and the total number of traps (N_t) [102]:

$$A \propto \Delta n_{trap} = (f_t(\Delta n, T) - f_{t0})N_t \quad (3.4)$$

which means that the change in A can either be due to a change in trap density or occupancy ratio. In this equation, f_{t0} is the occupancy ratio in the dark. As indicated in Eq. (3.4), the occupancy ratio of the traps is a function of Δn and temperature [102]. Since all the PCD measurements are done at the same temperature of 45 °C, T is constant.

However, due to the lower lifetime after degradation, Δn is reduced, possibly impacting A . Hence, it is possible that the variation in A is due to changes in Δn , and not N_t .

It was shown previously that for defects with one or multiple energy levels, the fraction of each energy level filled with electrons, f_t , in the non-equilibrium steady-state situation can be calculated by [102]:

$$f_t = \frac{1}{1 + \frac{kn_1 + p}{kn + p_1}} \quad (3.5)$$

The derivative of f_t with respect to Δn is:

$$\frac{df_t}{d\Delta n} = \frac{d(f_t - f_{t0})}{d\Delta n} = \frac{k^2n_1 + kp_0 - p_1}{(k\Delta n + p_1 + kn_1 + p_0 + \Delta n)^2} \quad (3.6)$$

The sign of this fraction defines the increasing or decreasing nature of the f_t as a function of Δn and it depends only on the sign of the numerator. Since this sign is not injection-dependent, it is concluded that the change of f_t with Δn is monotonic (converging to $k/k+1$ at high injection levels) for a given trap in each sample. For a minority carrier trap in p -type wafers, f_t increases monotonically. This means that for two excess carrier densities Δn_1 and $\Delta n_2 < \Delta n_1$, it can be assumed that $f_{t2} < f_{t1}$.

This relation is also presented in Fig. 3.11 which is generated using Eq. (3.5). This figure presents the change in the occupancy ratio as a function of Δn at 30 °C for a defect in a p -type wafer ($N_A = 10^{16} \text{ cm}^{-3}$) with the energy level at mid-gap and $k = 150$. When Δn is increased, f_t increases until it saturates at high injection levels. If it can be demonstrated that the occupancy ratio has a negligible change at Δn values higher and lower than the Δn in the degraded state, it can be assumed that the measured trap density is not influenced by the trap occupancy ratio.

To investigate this, PCD measurements of a sample in the *annealed* state are acquired in a Δn range significantly lower than Δn of the *degraded* state. This is done using a neutral density (ND) filter in front of the flash. In Fig. 3.12 (a), the PCD measurements of a sample in the annealed state with and without the ND filter, along with the measurement in the degraded state are shown. In Fig. 3.12 (b), the change in Δn_{app} as a function of time for these three measurements is shown. Since the peak of Δn_{app} is at a

high injection level and no effect of traps on the lifetime curve can be observed at this injection level [see Fig. 3.4 (a)], it is assumed that $\Delta n_{app} = \Delta n$. As can be seen, the ND filter reduces the maximum Δn in the annealed sample to a range significantly lower than Δn of the fully degraded state. However, even when the filter is used, the traps remain visible. The determined values for A in the annealed states with and without the ND filter are almost identical at $(2.00 \pm 0.05) \times 10^{-5}$ and $(2.15 \pm 0.05) \times 10^{-5}$ S, respectively. Thus, it is shown that the occupancy ratio has only negligible change at the two Δn values, one higher and one lower than the Δn of degraded state. Therefore, it can be assumed that A is indeed proportional to the trap density.

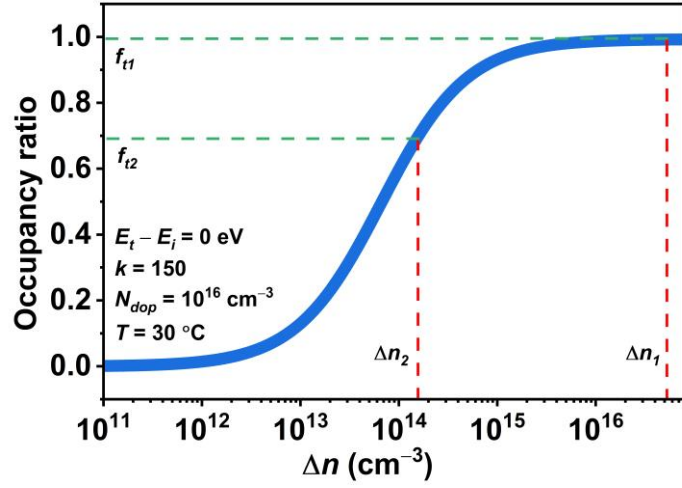


Fig. 3.11. The simulated occupancy ratio as a function of Δn at 30 °C in a p -type sample with a doping density of $1 \times 10^{16} \text{ cm}^{-3}$ for a defect center with $E_t - E_i = 0 \text{ eV}$ and $k = 150$.

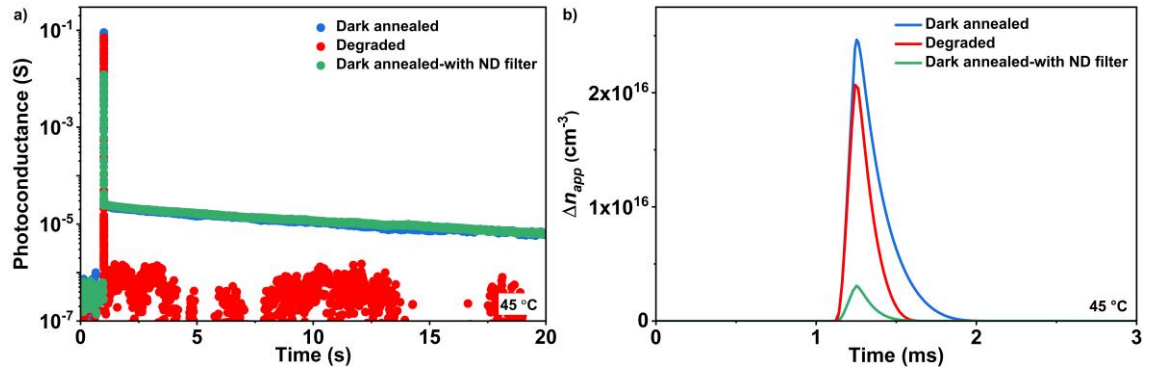


Fig. 3.12. (a) PCD curves measured at 45 °C of a sample from Set 1 in the annealed state with and without an ND filter and in the degraded state without an ND filter. (b) The corresponding apparent carrier density in the sample for each measurement.

After confirming that the pre-exponent is proportional to the trap density, the changes in trap and defect density after partial degradation can be studied further. For this purpose, a representative sample from Set 1 was light-soaked with halogen lamps and the change in lifetime and trap density was monitored after various light soaking durations. The

choice of degradation method (halogen lamps) is due to the slower rate of degradation with this method. Thus, the changes in both defect and trap densities can be investigated with higher resolution of light soaking time intervals. In Fig. 3.13 (a), the change in the lifetime of the sample after various light soaking times is presented. As expected, the lifetime decreases with light soaking and this decrease is faster initially. In Fig. 3.13 (b), the change in the PCD curve of the same sample after the same light soaking durations is demonstrated. The PCD is fitted up to 480 minutes of light soaking since after this time the noise in the measurement hinders a correct assessment of NTD. The traps are annihilated as the BO-related defects are being generated. To further study this correlation, the rate of both changes is calculated.

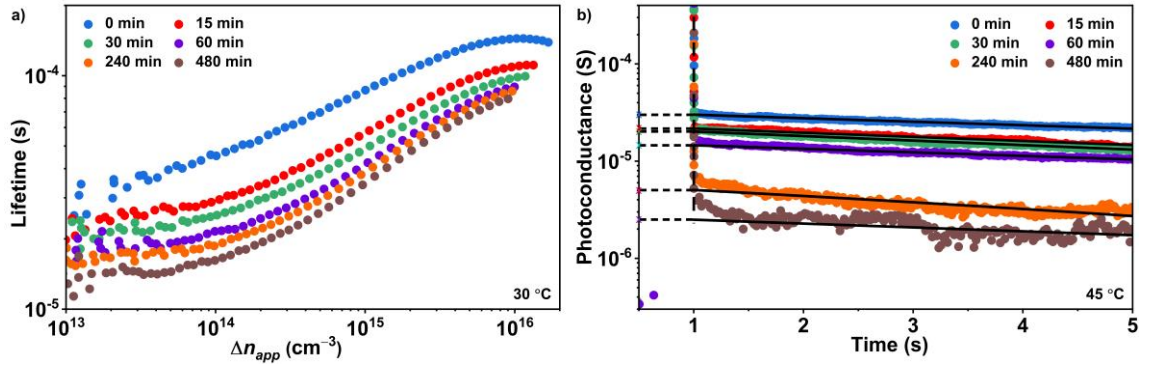


Fig. 3.13. (a) QSSPC lifetime curves measured at 30 °C; and (b) PCD curves measured at 45 °C of a sample from Set 1 sample after various light soaking durations. The solid lines are the mono-exponential fits to the curves and the “X” marks the extracted pre-exponents from the fits.

In Fig. 3.14, the change in NDD and NTD as a function of light soaking duration is shown. A clear anticorrelation can be observed between the generation of BO defects and the annihilation of traps. Both densities demonstrate an exponential dependence on light soaking time. By simultaneous fitting of the experimental data in Fig. 3.14 with a mono-exponential function ($R^2 = 0.98$), a time constant of 54 ± 5 min is determined for the changes of trap density and NDD. This value is in good agreement with the previously reported value of ~ 52 min for the generation rate of slow-formed BO defect centers in a B-doped wafer ($1 \times 10^{16} cm^{-3}$ [B] and $7-8 \times 10^{17} cm^{-3}$ [O_i]) degraded under 0.1 sun illumination at 60 °C [103]. As it has been shown that the degradation rate is almost independent of illumination intensity in the range of 0.01–1 sun [104], the values reported by Bothe *et al.* [103] can be directly compared with the value determined in this study. It should be noted that the sum of NDD and NTD was not fixed to unity and the slight deviations represent the uncertainty associated with the calculations. This result suggests that the traps act as a precursor for the recombination-active BO defect. This means that

the trap transforms to a recombination-active defect with light soaking and with DA, the defect returns to its trapping state. This transformation seems to be repeatable over many cycles. The obtained results agree with the observations of anticorrelation between the densities of minority carrier traps and the recombination-active centers measured with DLTS method in n^+-p and Schottky diodes in B-doped Cz silicon crystals [62, 63].

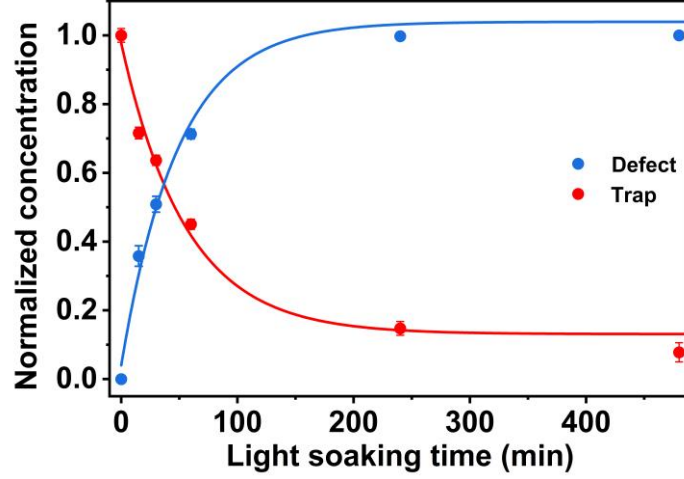


Fig. 3.14. Trap and defect density of a sample from Set 1 as a function of light soaking duration at 60 °C under 1 sun. The solid lines are exponential fits to the data.

3.3.3 Doping- and temperature-dependent PCD measurements

Doping- and temperature-dependent measurements are performed to investigate the physical nature of the trap. A previous study has shown that for a single level trap in a p -type wafer at low injection level ($N_A \gg \Delta n$) with negligible minority carrier recapturing, the relationship between the PCD time constant and trap parameters can be described by [44]:

$$\frac{1}{\tau_{decay}} = \sigma_p v_p p_0 + (\sigma_n v_n n_1 + \sigma_p v_p p_1) \quad (3.7)$$

where σ_p , σ_n , v_p , v_n [105], p_0 , n_1 , p_1 , n_i [106], E_t , E_i , k_B , and T has been defined previously. If the assumptions for Eq. (3.7) are fulfilled (see discussion below), by having samples with different resistivities and plotting $1/\tau_{decay}$ vs. $v_p p_0$ curve, σ_p of the trap can be extracted from the slope [44]. Note that the intercept with the $1/\tau_{decay}$ axis should always be positive since both the second and third terms are always positive. The three assumptions needed for the validity of Eq. (3.7) are [44]:

1. The trap has negligible minority carrier re-capture. In other words, the traps almost only emit minority carriers (de-trapping), emit majority carriers, and capture majority carriers (recombination through traps) during the de-trapping.
2. The density of minority carriers is very small during de-trapping (low injection).
3. It is a single-level trap.

First assumption

Recapturing rates can be tested by comparing PCD time constants of samples with different effective lifetimes. In Fig. 3.15, the effective lifetime and PCD of a representative sample from Set 1 before and after one hour of light soaking are presented. Although the lifetime at Δn of $1.1 \times 10^{15} \text{ cm}^{-3}$ is reduced by more than 50% from its initial value, τ_{decay} changes by less than 5%. This observation indicates that the duration the minority carriers are present in the conduction band does not affect τ_{decay} , meaning that the recapturing of minority carriers is negligible for this trap [44].

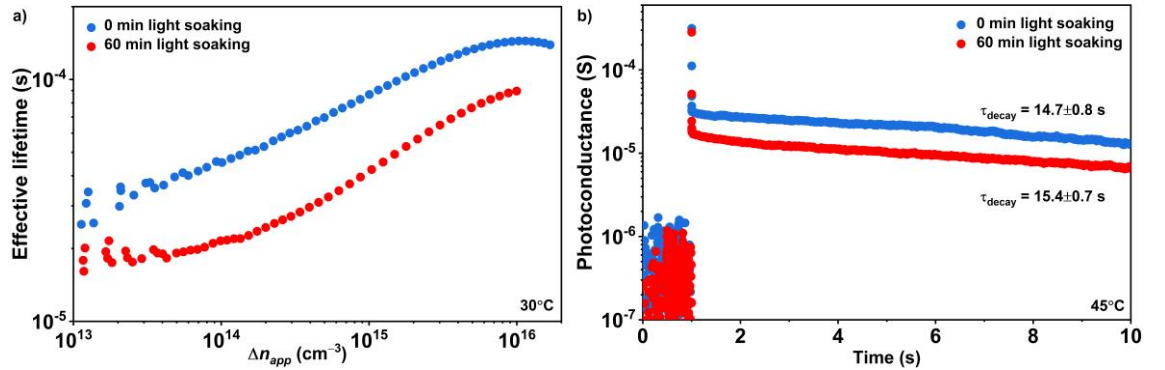


Fig. 3.15. (a) QSSPC lifetime curves measured at 30 °C; and (b) PCD curves measured at 45 °C of a sample from Set 1 before and after light soaking at 60 °C under 1 sun illumination for 60 min.

Another simple method to significantly change the lifetime is to remove the surface passivation. This was done for a sample from Set 2 and the results are shown in Fig. 3.16. While the lifetime drops by almost two orders of magnitude after removing the passivation, the PCD time constant results in a negligible change: 3.86 ± 0.01 sec and 3.84 ± 0.01 sec for samples with and without passivation, respectively. This observation further confirms the assumption that the recapturing of minority carriers by the traps is insignificant. This method is more dependable compared with degradation (see Fig. 3.15) since after partial degradation, the density of traps also reduces which can affect the minority carrier recapture rate of the traps. By removing the passivation, the density of traps is expected to stay unchanged while the average time the minority carriers spend in the conduction band is significantly reduced. The observed negligible carrier recapture by the traps further confirms that the investigated BO-related trap is indeed a *slow* trap.

It should also be noted that the reason that the presence of traps is clear in the lifetime curve of this sample compared with the samples from Set 1 [see Fig. 3.4 (a)] is the higher density of filled traps (factor of ~15) in samples from Set 2.

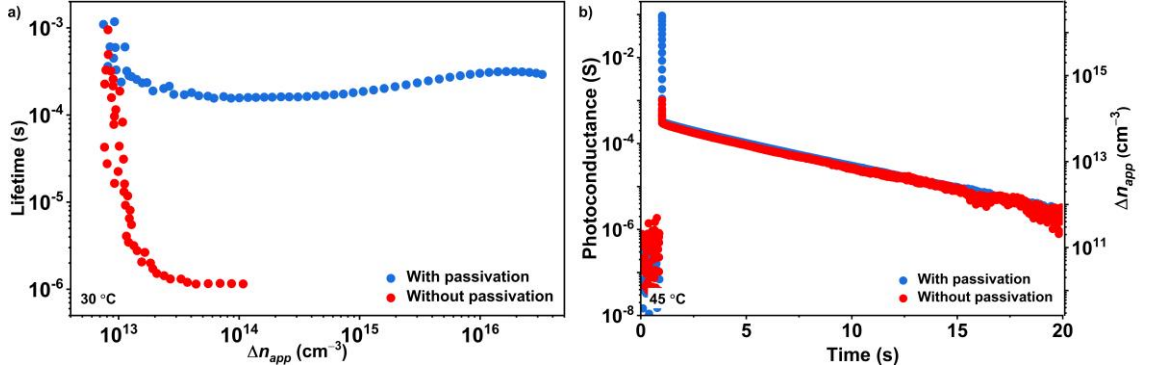


Fig. 3.16. (a) QSSPC lifetime curves measured at 30 °C; and (b) PCD curves measured at 45 °C of a sample from Set 2 with and without passivation.

Second assumption

Previously it was shown that while PC-based measurements are affected by the traps, PL-based QSS measurements are not affected by this phenomenon [35]. This knowledge can be used to investigate the second assumption (low injection) by measuring the real majority and minority carrier densities during PCD measurements. It was shown in Chapter 2 that minority carrier density can be measured from the PL measurement. Using the PC equation and inserting the extracted Δn from PL, Δp can be calculated:

$$\Delta p = \frac{\frac{\Delta \sigma}{qw} - \mu_n \Delta n}{\mu_p} \quad (3.8)$$

It should be noted that μ_p is a function of Δp , thus, an iterative process is needed to extract Δp . Using this method, the change of Δp and Δn as a function of time is shown in Fig. 3.17 for a representative sample from Set 1.

While the majority carrier density remains at high levels for > 10 sec, the minority carrier density returns to its dark value immediately after the flash cut off. This observation confirms that the region that is dominated by the traps is indeed at a low injection level (Δn is very small).

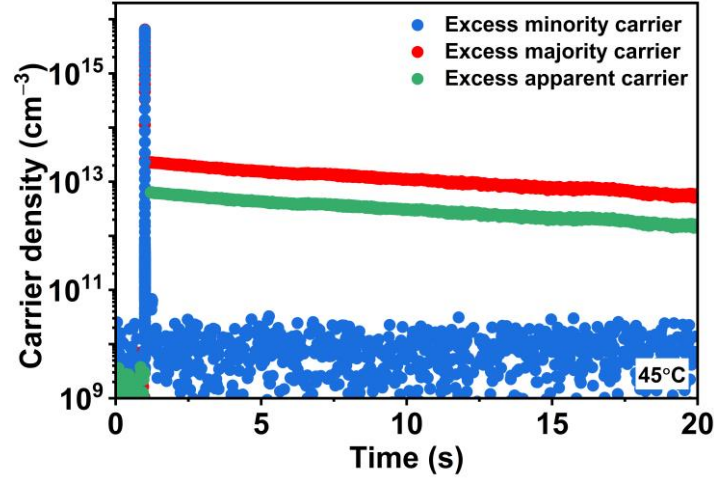


Fig. 3.17. Minority, majority, and apparent carrier densities as a function of time for a sample from Set 1.

It is also noted that in Fig. 3.17, the calculated excess apparent carrier density is lower than the excess majority carrier density. This is because the minority carriers are not participating in generating the conductance, while for the calculation of Δn_{app} , an equal number of excess majority and minority carriers is assumed. This means that in reality, more majority carriers are present to compensate for the trapped minority carriers. For p -type samples, this effect is further amplified due to the difference between the electron and hole carrier mobilities. For the sample investigated here, at a low injection range, the mobility of electrons is ~ 3 times higher than the mobility of holes [101]. This means that ~ 4 times more majority carriers are needed to generate the same conductance in comparison with an equal density of excess majority and minority carriers. For n -type samples, the effect is much smaller but still present.

Until now, the first two assumptions are shown to be valid for the BO-related trap. The third assumption will be discussed in more detail below.

Checking Equation Validity

Using the data obtained for the three samples, Fig. 3.18 presents $1/\tau_{decay}$ (measured at 45 °C) as a function of v_{pp0} after DA. It also shows the linear function that provides the best fit ($R^2 = 0.96$). The fitted curve has a slope of $8.1 \times 10^{-25} \text{ cm}^2$ and a y-intercept of -0.06 s^{-1} . Despite the low-quality fit, it is clear that the intercept value is negative, suggesting that Eq. (3.7) is not suitable to describe the trap investigated here. This means that one of the assumptions is incorrect. As the assumptions of negligible minority carrier re-capture and low injection level have been confirmed, the fact that Eq. (3.7) cannot

describe the doping-dependent measurement result indicates that this trap is *not a single-level trap*.

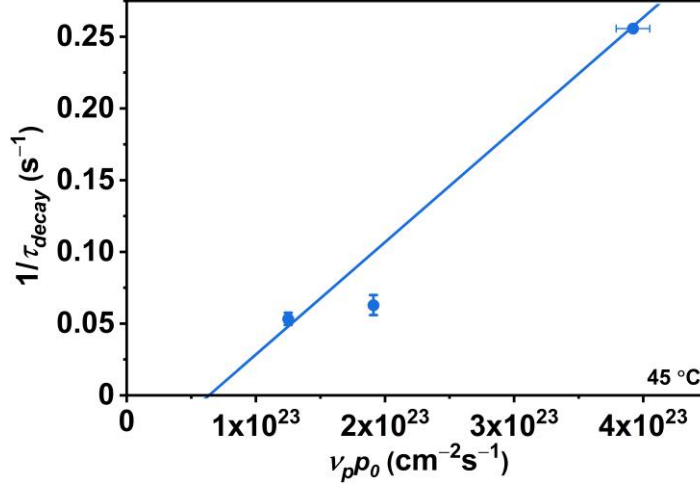


Fig. 3.18. Doping dependence of the PCD time constant for three samples with varying resistivities. The solid line is a linear fit to the data.

To further investigate the validity of Eq. (3.7) and extract the de-trapping activation energies, measurements at various temperatures were done. The activation energies are calculated by fitting a double-exponential decay function in the form of:

$$\frac{1}{\tau} = A_1 \exp\left(-\frac{E_{a1}}{k_B T}\right) + A_2 \exp\left(-\frac{E_{a2}}{k_B T}\right) \quad (3.9)$$

where A_1 and A_2 are the pre-exponential factors and E_{a1} and E_{a2} are the activation energies. In Fig. 3.19, temperature-dependent measurements of a representative sample from Set 2 in the 25 °C to 145 °C temperature range are presented. The initial drop in the PC signal (recombination-related) is removed from the curves. The solid lines are the fitted mono-exponential functions [see Eq. (3.1)] at each temperature. The same fitting process has been performed for a sample from Set 1 in the 25 °C to 105 °C temperature range.

In Fig. 3.20, the Arrhenius plot of the inverse of the PCD time constant for two representative samples from Sets 1 and 2 is presented. These curves are fitted with a double-exponential fit based on Eq. (3.9). Each exponential term is shown with a dashed line, while the total fit is presented with a solid line. Both curves have two slopes in their Arrhenius plot indicating two activation energies, each dominant in one temperature range. The temperature range where the change in the slope occurs shifts to lower temperatures for the sample with higher resistivity. The activation energies extracted for

the sample with $1.3 \Omega\cdot\text{cm}$ resistivity are 1.13 ± 0.05 eV and 0.2 ± 0.1 eV, and for the sample with $0.7 \Omega\cdot\text{cm}$ resistivity, the activation energies are 1.05 ± 0.01 eV and 0.36 ± 0.01 eV.

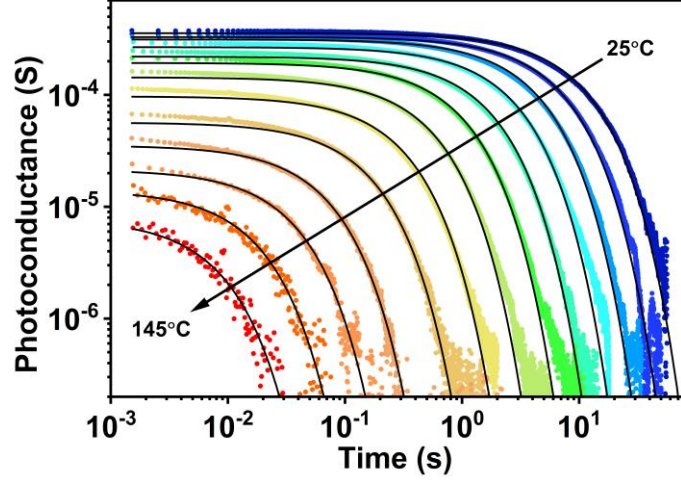


Fig. 3.19. Temperature-dependent PCD curves of a Set 2 sample in the 25 °C to 145 °C temperature range. The solid lines are mono-exponential fits to the curves.

In Eq. (3.7), the difference between the PCD time constants for samples with different doping levels is reflected in the first term. Moreover, the other two terms have a stronger temperature dependency compared with the first term (due to the strong temperature-dependency of n_I and p_I). Thus, by increasing the temperature, the effect of the first term on the PCD time constant becomes less significant. As a result, the time constant of samples with different doping levels becomes closer at higher temperatures. This difference in temperature-dependency of terms can also result in having two activation energies in two ranges of temperatures. These two effects are shown in Fig. 3.21 which demonstrates a simulated Arrhenius plot for a *single-level trap* in three different samples with various doping levels. At lower $1/k_B T$ values, the time constants converge. While increasing temperature can lead to having more similar PCD time constants, the PCD time constant of a sample with a lower doping level can never be higher than a sample with a higher doping level at the same temperature. This is in contrast to the experimental results presented in Fig. 3.20, further suggesting that Eq. (3.7) does not suitably describe this trap which in turn shows that the BO-related trap investigated in this chapter has *more than one* energy level.

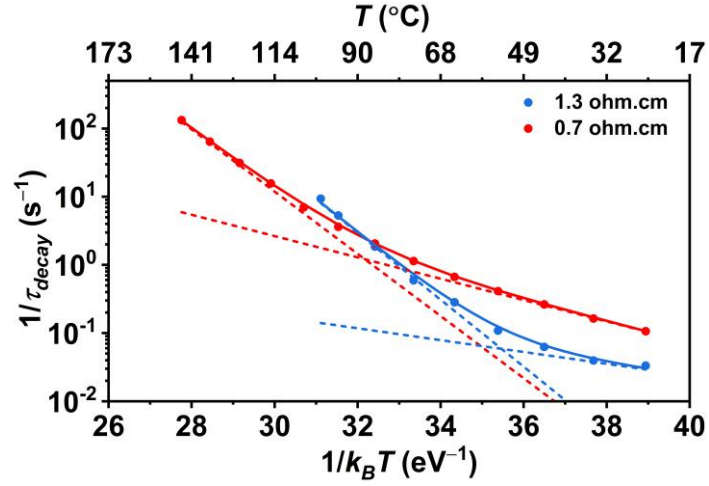


Fig. 3.20. Temperature dependence of the PCD time constant for two samples with different resistivities from Sets 1 and 2. The solid line shows a fitting with a double-exponential decay function and the dashed lines show each exponential fit.

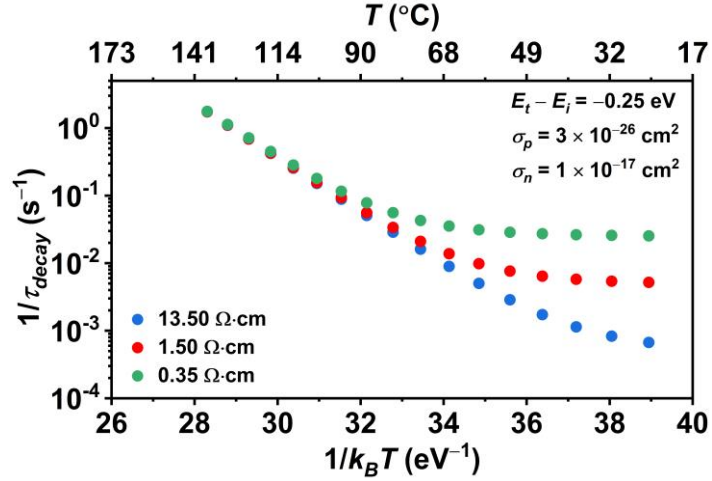


Fig. 3.21. Temperature dependence of the PCD time constant simulated for three samples with different resistivities for a *single-level trap* with $E_t - E_i = -0.25$ eV, $\sigma_p = 3 \times 10^{-26}$ cm², and $\sigma_n = 1 \times 10^{-17}$ cm².

3.4 Chapter summary

In this chapter, minority carrier traps in B-doped Cz silicon wafers were investigated using PCD measurements. While traps are typically investigated as a source of error in PC-based lifetime measurements, in this chapter the possible correlation between traps and recombination-active defects is investigated.

First, the presence of a trap in B-doped Cz silicon wafers was observed. It was shown that this trap is due to the simultaneous presence of B and O in the wafers. Moreover, it was shown that the traps are annihilated as the BO-related defects are generated and vice versa, suggesting that traps are acting as the precursor of BO-related defects. This suggestion was confirmed by comparing the rate of defect formation and trap annihilation during degradation.

To further investigate trap characteristics, doping- and temperature-dependent measurements were done. The results from doping-dependent measurements suggest that the observed BO-related traps have more than one energy level. This result was further confirmed by the temperature-dependent measurements. Moreover, the de-trapping activation energies were extracted for a wide temperature range, showing that two temperature regions are governed by different de-trapping activation energies.

Our findings suggest that while lifetime measurements investigate defects in their recombination-active state, PCD measurements can act as their equivalent to investigate defects in their non-recombination-active state. In the next chapter, PCD measurement will be utilized to investigate traps in B-doped mc-Si wafers.

Chapter 4

Investigation of Traps in Boron-Doped Multicrystalline Silicon¹

It was shown in the previous chapter that the investigation of traps is a useful method to study the precursor of defects in B-doped Cz silicon wafers. This finding suggests that while traps are typically considered as an unwanted artifact that hinders a correct lifetime assessment, they can be of significance to obtain critical information about defects in their non-active state.

In this chapter, the method developed in Chapter 3 is utilized to investigate traps in B-doped mc-Si wafers. In Section 4.1, previous findings regarding traps in B-doped mc-Si wafers are reviewed. In Section 4.2, the details of measurement and analysis methods (beyond what has been reviewed in previous chapters) are reported, and the findings are presented and discussed in Section 4.3.

4.1 Traps in B-doped mc-Si

Artificially high lifetimes at low injection levels have been reported in B-doped mc-Si wafers [107]. This artifact can be correlated with the presence of DRM [99], change in the charge barrier at the grain boundaries during illumination [108], or the presence of traps [45, 107]. While DRM occurs in both monocrystalline- and mc-Si wafers, charge buildup at the grain boundaries is specific to mc-Si. It has been shown previously that there are space-charge potential barriers for majority carriers at the grain boundaries of

¹ This chapter is partially based on:

S. Jafari, Y. Zhu, F. E. Rougieux, and Z. Hameiri, in *36th European Photovoltaic Solar Energy Conference and Exhibition (EUPVSEC)*, 2019.

S. Jafari, Y. Zhu, F. E. Rougieux, and Z. Hameiri, in *Asia-Pacific Solar Research Conference (APSRC)*, 2019.

S. Jafari, and Z. Hameiri, “Investigation of minority carrier traps in *p*-type mc-Si: Effect of firing and laser annealing”, *Sol. Energy Mater. Sol. Cells*, vol. 232, pp. 111341, 2021.

mc-Si wafers [108-110]. Following illumination, the charge barrier reduces, causing an increase in the majority carrier lateral flow which in turn increases the lateral conductance [108].

Besides the effect of grain boundaries, traps have been investigated as the source of an artificially high lifetime in B-doped mc-Si wafers at low injection levels [45, 107]. A study by Macdonald *et al.* reported that the density of *fast* traps is correlated with the dislocation density [45]. Another study suggested that the density of traps in B-doped mc-Si wafers is correlated with the oxygen concentration and anticorrelated with metallic impurities [111]. On the contrary, in another study, it has been suggested that the traps in mc-Si wafers can be related to mobile impurities, as the density of those traps has been found to be correlated with improvement in lifetime after P-diffusion gettering [112].

The method of fabrication significantly impacts the quality of silicon wafers [69, 113]. One of these processes is firing, which is used to form ohmic contacts between the metal grid and the silicon [114]. Moreover, the firing process releases hydrogen from the hydrogen-rich surface passivation layers to passivate bulk defects [115]. However, it has also been shown that firing is linked to LeTID in mc-Si, Cz, and FZ wafers [69, 116, 117]. To date, only a few studies have investigated the impact of fabrication processes on trap density [111, 113, 118]. For B-doped mc-Si, it has been shown that hydrogenation through firing decreases the density of traps while post-firing annealing above 500 °C recovers them [118]. It is also shown that after gettering, while the density of traps is not reduced, they are distributed more uniformly throughout the ingot in B-doped mc-Si wafers [113]. In these studies, the physical reason behind the change in the trap density was not discussed.

In this chapter, the presence of slow traps in B-doped mc-Si wafers is investigated. Additionally, the effect of firing, post-firing DA, and laser annealing on the traps is studied. Then, the possibility of a correlation between traps and LeTID-related defects is discussed. Finally, PCD measurements on mono-cast silicon wafers of varying crystallinity are done to investigate the effect that structural defects may have on the traps.

4.2 Materials and methods

A set of sister B-doped mc-Si wafers with a resistivity of $1.68 \pm 0.05 \, \Omega \cdot \text{cm}$ and thickness of $180 \pm 3 \, \mu\text{m}$ were used in this study. Wafers were gettered via a P-diffusion

process at 840 °C for 45 min. The diffused layer was then removed using an HF-HNO₃ solution with a volumetric ratio of 1:10. Some of the samples were then passivated with SiN_x using a PECVD system (refractive index of 2.08 at 632 nm) [92]. When required, the SiN_x was etched off using a 5% HF solution. The firing was done using a belt furnace (SCHMID) with a wafer peak temperature of 815 °C. For laser annealing, the samples were illuminated with a 932 nm laser at 140 °C (45 kW/m² intensity) [94]. In Fig. 4.1, the processing and characterization steps for each sample are shown. In this flowchart, the measurements are presented with blue boxes, the processing steps are marked with green boxes and each path is labeled from 1 to 11. Path 1 is designed to investigate the possible correlation between traps and TDDs. Paths 2, 5, 6, 7, and 8 are designed to investigate the impact of firing and post-firing DA on traps. Path 4 is to investigate the possible connection between the observed long PCD and DRM effect. Finally, paths 3, 9, 10, and 11 are designed to investigate the impact of laser annealing on traps and to study the possible connection between traps and LeTID-related defects. The corresponding path for each figure is stated in the figures' caption.

PCD and lifetime measurements were done using the customized lifetime tester introduced in Chapter 3 at 30 °C before firing and -100 °C before and after the firing process as well as after laser annealing. The reasons behind the selection of the temperatures will be discussed in more detail below. For the PCD measurements, the flash was used in the 1/64 mode with a decay time constant of 35 µs. Since the bulk of mc-Si wafers is quite non-uniform, care was taken to measure the same location (±1 mm uncertainty) for each sample. To determine the PCD time constants, the PCD curves were fitted using a double-exponential decay function in the form of:

$$\Delta\sigma = A_1 \cdot \exp\left(-\frac{t}{\tau_{decay1}}\right) + A_2 \cdot \exp\left(-\frac{t}{\tau_{decay2}}\right) \quad (4.1)$$

where A_1 and A_2 are the pre-exponential factors (correlated with the trap densities), and τ_{decay1} and τ_{decay2} are the PCD time constants. The reason for selecting a double-exponential function (and not a single-exponential function) will be discussed in more detail in the next section. Lifetime measurements were performed at 30 °C before and after each PCD measurement using the same system to ensure that the measurements did not alter the lifetime. For lifetime measurements, the flash was used in the QSS mode with a decay time constant of around 2.3 ms. As it was shown in Chapter 3, the transient

flash has a much shorter decay time constant. For this study, this is beneficial to reduce the effect of charge barrier reduction (as will be discussed in Section 4.3.1). Moreover, the very high number of flash exposures during the PCD measurement might lead to the degradation of the sample through light-induced degradation. Such a short decay time of the transient flash also minimizes the possible impact of light soaking due to the flash.

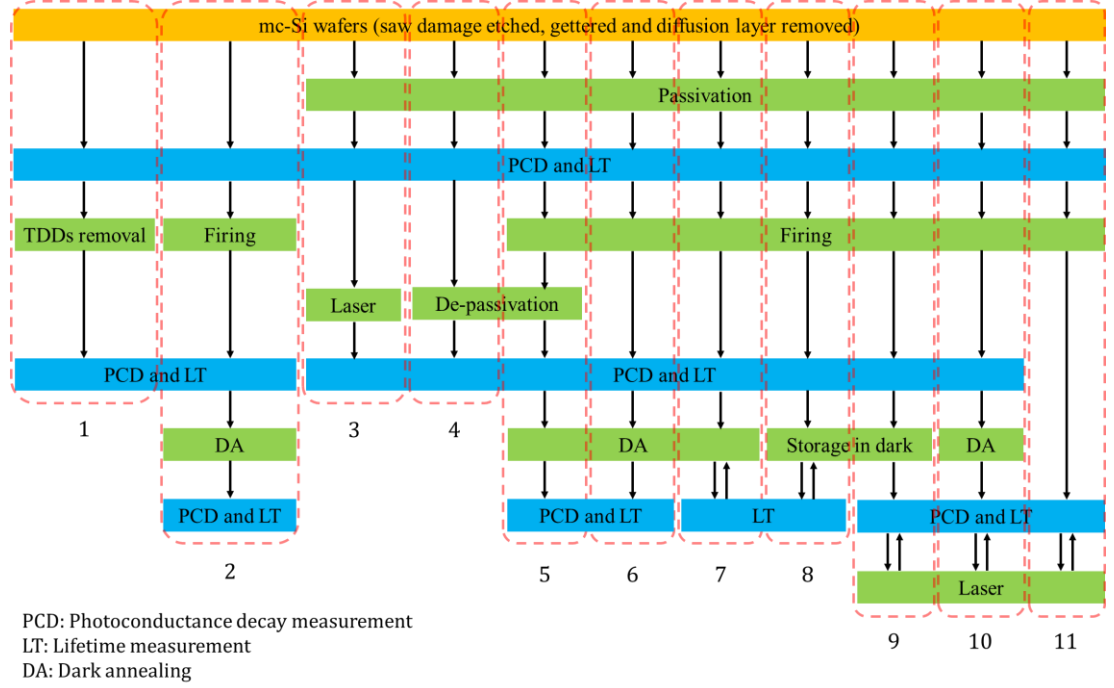


Fig. 4.1. Processing and experimental design for the investigation of traps in B-doped mc-Si wafers.

As mentioned, most of the PCD measurements were performed at $-100\text{ }^{\circ}\text{C}$. This is because the temperature has a critical impact on the quality of the PCD measurements. In Fig. 4.2 (a) and Fig. 4.2 (b), the PCD curves of a sample measured at $30\text{ }^{\circ}\text{C}$ and $-100\text{ }^{\circ}\text{C}$ are presented, respectively. While Fig. 4.2 (a) is generated by averaging 3,500 PCD measurements over thirty hours, Fig. 4.2 (b) is generated by averaging 470 PCD measurements over three hours. The SNR in the de-trapping region has been increased by a factor of ~ 3 (from 12.1 dB to 36.6 dB) when decreasing the measurement temperature from $30\text{ }^{\circ}\text{C}$ to $-100\text{ }^{\circ}\text{C}$, despite the lower number of averaged measurements at the lower temperature. As mentioned in Chapter 3, this is likely due to the higher mobility of carriers at lower temperatures which leads to higher conductivity resulting in higher signal strength [98]. Moreover, de-trapping is a thermalization process that is faster at higher temperatures. Hence, at lower temperatures, a higher concentration of traps is filled at a similar time after the excitation, leading to a higher PC signal. Therefore, in

this study, the PCD measurements were performed at $-100\text{ }^{\circ}\text{C}$ to increase the fitting quality and to reduce the uncertainty associated with determining the PCD time constants.

It should be mentioned that measurements at low temperatures are not always a viable option for trap investigations. The conductance before the flash is considered as dark conductance and is subtracted from the signal. Thus, for averaging PCD measurements, it is important to make sure that traps are almost empty before the next excitation (see Section 3.3.1). Since the duration of the low-temperature measurement is limited by the liquid nitrogen supply, it is challenging to detect traps with very long decay time constants at low temperatures. For this set of samples, considering the decay time constant of the second term, the period between consecutive flashes was chosen such that the background trap occupation was $< 2\%$.

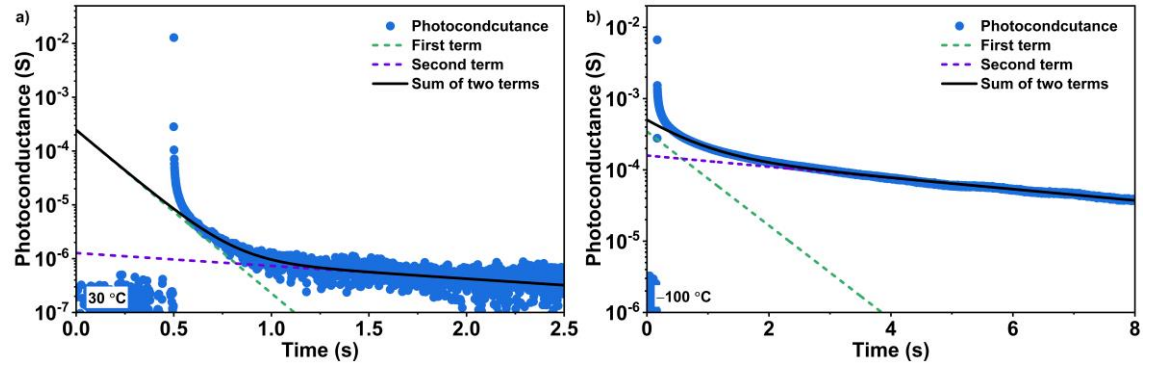


Fig. 4.2. PCD curves of a sample measured at (a) $30\text{ }^{\circ}\text{C}$; and (b) $-100\text{ }^{\circ}\text{C}$. The dashed lines are the two terms of the double-exponential fit, while the solid lines are their sum.

4.3 Results and discussion

4.3.1 Presence of trap-related long PCD time constant

In Fig. 4.3 (a), the PC-based and PL-based lifetime measurements of a representative sample before firing are presented. The two measurements agree well at high injection. However, at low injection, the PL-based lifetime decreases while the PC-based measurement significantly increases. This increase is an artifact that has been explained by the presence of traps or by the DRM effect [99, 119]. Both have only a negligible impact on PL-based measurements [35]. Another possible explanation for this phenomenon in mc-Si wafers is a reduction of the charge barrier in the vicinity of the grain boundaries due to illumination, which leads to an increase in the lateral flow of majority carriers [108-110]. However, it has been shown that the barriers return to their initial state when the illumination intensity is below 1×10^{-5} suns [109, 110]. Considering

the maximum illumination intensity (50 suns) and decay time constant of the flash ($\sim 35 \mu\text{s}$), the illumination intensity of 1×10^{-6} suns is reached $\sim 630 \mu\text{s}$ after the flash. As the trapping effect in this study is clearly visible for much longer times, it can be suggested that the observed effect cannot be solely explained by a change of the charge barriers at the grain boundaries.

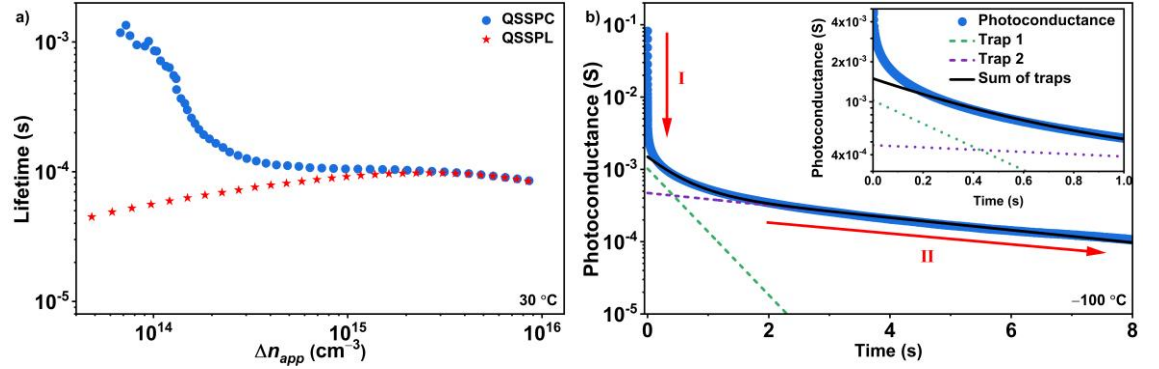


Fig. 4.3. (a) QSSPC and QSSPL lifetime curves measured at 30 °C; and (b) PCD curve measured at $-100 \text{ }^{\circ}\text{C}$ of a sample before firing. The dashed lines are the two terms of the double-exponential fit, while the solid line is their sum.

In Fig. 4.3 (b), the PCD curve of the same sample measured at $-100 \text{ }^{\circ}\text{C}$ is shown. There is a significant drop in the measured PC signal following the flash (marked with “I”) due to carrier recombination via different channels (mainly by recombination-active defects). This decay is followed by a much slower second decay (marked with “II”). As mentioned in Chapter 3, one possible source of such long PCD is the presence of the DRM effect in the samples [45, 99]. To confirm that the long PCD is not due to the DRM effect, the PCD of a sample was measured with and without surface passivation. In Fig. 4.4 (a), the lifetime curves of a representative sample, before and after the removal of the passivation layers are presented. It can be observed that while removing the passivation significantly reduces the lifetime, an abrupt increase in the lifetime is still clearly visible at low injection. In Fig. 4.4 (b), the PCD measurements of the same sample with and without passivation are shown. A similar decay is observed in both cases, indicating that DRM does not strongly impact the measurements. Hence, it can be suggested that traps, not DRM, are the source of the long PCD.

In Fig. 4.3 (b), the significant change in the recombination rate of carriers leads to a difference in the time constants of more than four orders of magnitude between the initial decay (due to carrier recombination) and the secondary decay (due to the emission of carriers from the traps). Such a sharp drop in the time constant should result in a sharp transition between these two decays. However, zooming into the transition between the

decays with the inset of Fig. 4.3 (b), this cannot be observed. The long decay cannot be fitted with only one exponential decay equation, suggesting that more than one trap is affecting the PCD curve in this range. Consequently, the PCD curves are fitted using the double-exponential decay function shown in Eq. (4.1). These two traps are labeled as “Trap1” (the trap with the smaller PCD time constant) and “Trap 2” (the trap with the larger PCD time constant). The time constants for Traps 1 and 2 are determined to be 0.68 ± 0.08 sec (0.14 ± 0.1 sec) and 5.44 ± 0.29 sec (1.87 ± 0.43 sec) at -100 °C (30 °C), respectively. Since the uncertainty associated with the fitting of Trap 2 is smaller (as the fitting of the fast decay is strongly impacted by Trap 2 and might also be impacted by the effect of charge build-up around the grain boundaries [108]), in this study only the trap with the *larger* decay time constant is investigated. The long decay and the presence of traps at illumination intensities well below 1×10^{-5} suns clearly indicate that barrier change around grain boundaries is not the only source of trapping in these mc-Si wafers. Note that both traps can be classified as *slow* traps since:

1. It has been shown that *slow* traps can be fitted with a “simple” exponential function, while *fast* traps cannot be fitted with such an expression [43, 46]. This means that the decay rate of *slow* traps does not change with time. Since in this study, the measured PCD curves can be fitted with two time-independent constants (τ_{decay1} and τ_{decay2}), it can be suggested that the investigated traps are *slow* traps [44].
2. After removing the surface passivation, only a negligible change has been observed in the PCD time constants of the two traps ($< 3.5\%$ for Trap 1 and $< 1\%$ for Trap 2), despite the significant drop of the lifetime illustrated in Fig. 4.4 (a). This further confirms the negligible re-capture of carriers after emission, meaning that the capture and emission of carriers only happen **once** in contrast to **multiple** capture and emission of carriers in *fast* traps. Thus, it can be suggested that both traps are *slow* [44].

One possible source of traps in silicon wafers is the presence of TDDs [120]. The possible connection between traps and TDDs was investigated by measuring the PCD of a sample before and after the TDDs removal process. In Fig. 4.5, the change in the PCD curve of an unpassivated sample before and after removing TDDs is shown. This is done by subjecting the sample to rapid thermal processing (peak sample temperature of 800 °C) for 10 sec [47]. While the trap density slightly decreases, the PCD tail is still visible after removing the TDDs. Hence, it can be concluded that the traps are not fully related to

TDDs. Although the slight change in the trap density (which was also observed after *firing* of unpassivated samples) might be due to removing TDDs, it can also be explained by a change in the impurity distribution after the high-temperature processing [121].

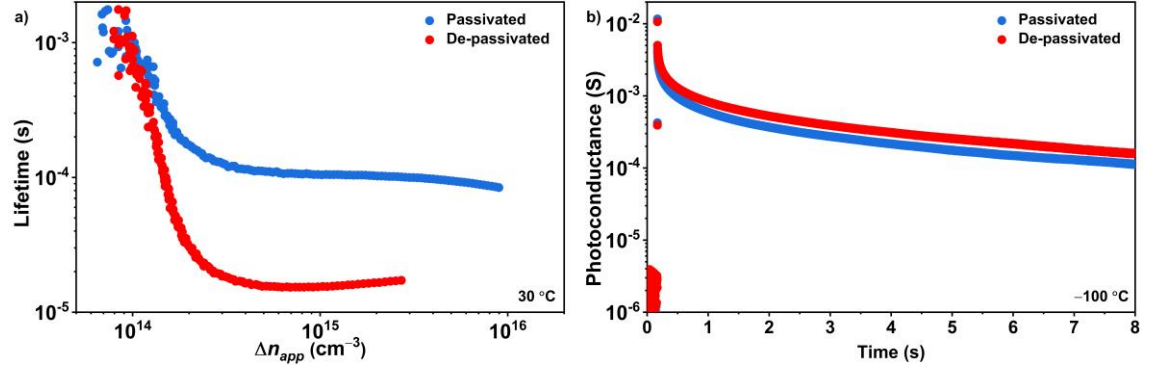


Fig. 4.4. (a) QSSPC lifetime curves measured at 30 °C; and (b) PCD curves measured at -100 °C of a sample with and without surface passivation (Path 4).

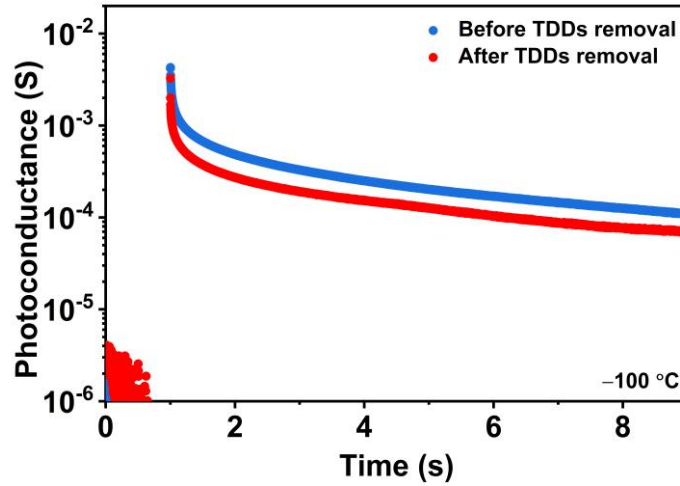


Fig. 4.5. PCD curves measured at -100 °C of an unpassivated sample before and after removing TDDs (Path 1).

This is the first report of *slow* traps with such long decay constants in mc-Si, as previously observed traps in mc-Si wafers can be classified as *fast* traps [107, 119] the properties of fast traps were discussed in (Section 2.3). As this trap is not due to thermal donors or BO-related traps (as will be shown below), it can be suggested that crystallographic and/or impurity-related defects are its possible sources. Investigation of the possible source of traps will be done in more detail in Sections 4.3.4 and 4.3.5.

4.3.2 Effect of firing on traps

In Fig. 4.6 (a), the lifetime measurements of a representative sample before and after firing (labeled as “AF”) are presented. Before firing, the impact of traps is noticeable at low injection. As expected, after the firing process the overall lifetime increases, probably

due to improved passivation of surface and bulk defects by hydrogen released from the dielectric layer [115]. Interestingly, it seems that firing also has a strong impact on the trap concentration as it is significantly reduced after the process. This agrees with previous reports regarding fast-decaying traps in *p*-type mc-Si wafers, showing a reduction in their density after firing [113, 118]. However, the trap density is recovered after several days of storage at room temperature (in the dark), suggesting that the temporary low trap density is due to a metastable state.

In Fig. 4.6 (b), the lifetime measurements of a second sample before and after firing, as well as after DA at 100 °C for various durations (labeled as “DA”) are presented. The same behavior is observed, in this case with a much faster recovery of the trap density.

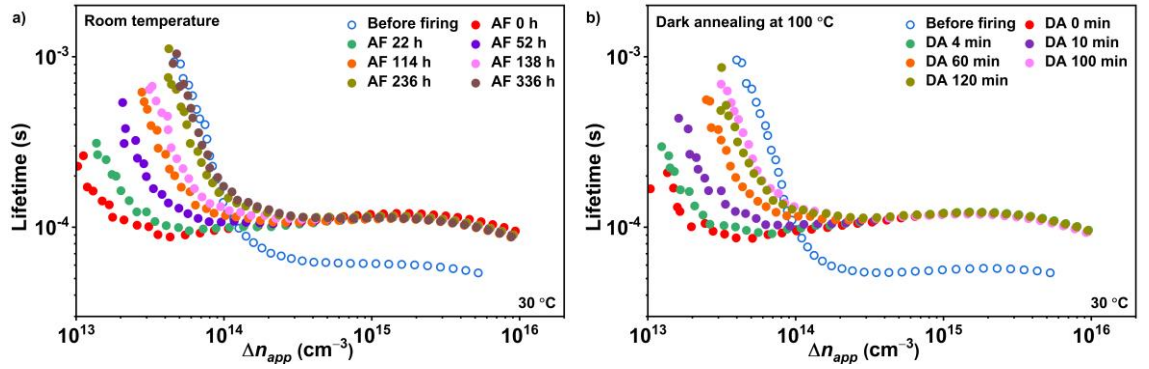


Fig. 4.6. QSSPC lifetime curves measured at 30 °C of a sample before firing, after firing, and (a) after storage at room temperature (Path 8); and (b) after DA at 100 °C for various times (Path 7).

Dekkers *et al.* reported that in order to recover annihilated traps after firing, annealing at 580 °C for 30 min is needed [118]. They indicated that the trap density is unaffected by annealing at a lower temperature (500 °C for 30 min) or without annealing. However, in this study, a recovery of the trap density even at room temperature is observed. It may be that Dekkers *et al.* did not measure the samples for a long enough time after firing and therefore did not notice a change. It is also noted that they observed a change in the lifetime at medium injection after annealing at 500 °C [118]. Such a change has not been observed here. While the trap density significantly changes during DA, the lifetime at medium and high injection ranges demonstrates only a negligible change. It is possible that the bulk of the samples from Ref. [118] have been modified during the process, explaining both the changes in lifetime and not observing a trap recovery after the annealing process. It is also noted that the study in Ref. [118] was done ~15 years ago. Considering the improvements in the wafer production, another possible reason for the

observed difference can be a difference in the wafer quality between this study and Ref. [118].

To investigate the source of the change in trap density after the firing and DA, PCD measurements were performed on unpassivated and passivated samples. In Fig. 4.7, the PCD curves of two representative samples, one unpassivated and one passivated, measured before firing, after firing, and after post-firing DA, are presented. Interestingly, in the unpassivated sample shown in Fig. 4.7 (a), the density of traps demonstrates only a small change after firing. Furthermore, after post-firing DA, the trap density seems to remain constant. On the other hand, for the sample with passivation, the trend is the same as observed in Fig. 4.6, the trap density drops after firing and recovers after the post-firing DA. This suggests that the metastable change in trap density is correlated with the presence of surface passivation on the samples. To further investigate this phenomenon, the PCD measurements were performed on a sample that have been fired *with* surface passivation, but their passivation layer *was removed* immediately after the firing (denoted “de-passivated”). In Fig. 4.8, the PCD curves for this sample are presented. Similar to the passivated sample, the trap density has a significant drop after firing, while it recovers following the DA process.

To quantify the changes in trap density, the curves were fitted using Eq. (4.1). In Fig. 4.9, the NTD of passivated, unpassivated, and de-passivated samples after firing and after post-firing DA is presented. To determine the NTD, the pre-exponential factor of Trap 2, which is correlated with the trap density, is calculated (see Section 3.3.2). The pre-exponents are then normalized to their initial (in here, pre-firing) values. After firing, the NTD of samples with surface passivation is reduced by $69\pm3\%$, while for samples without passivation the reduction is much smaller, in the range of $30\pm3\%$. A similar trend as the passivated samples is observed for the de-passivated samples. Moreover, while the passivated and de-passivated samples demonstrate a full recovery after DA, the trap density of the unpassivated samples changes by less than 5%. The results suggest that the metastable change in the trap density after firing is related to the SiN_x dielectric layer. Hence, it seems that while surface passivation is required during the firing process to observe this effect, it is not needed for the recovery of the trap density. The small change in the trap density of the unpassivated sample might be due to a change in impurities, or the removal of TDDs.

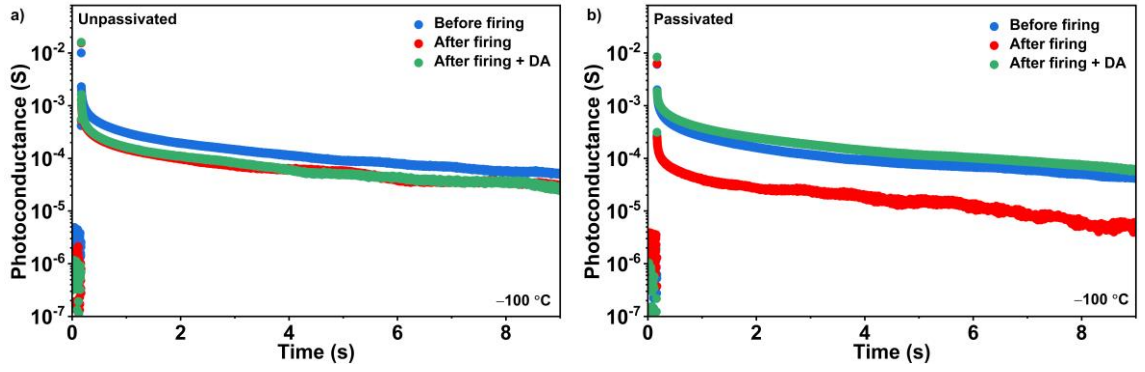


Fig. 4.7. PCD curves measured at $-100\text{ }^{\circ}\text{C}$ of (a) unpassivated (Path 2); and (b) passivated samples before firing, after firing, and after post-firing DA (Path 6).

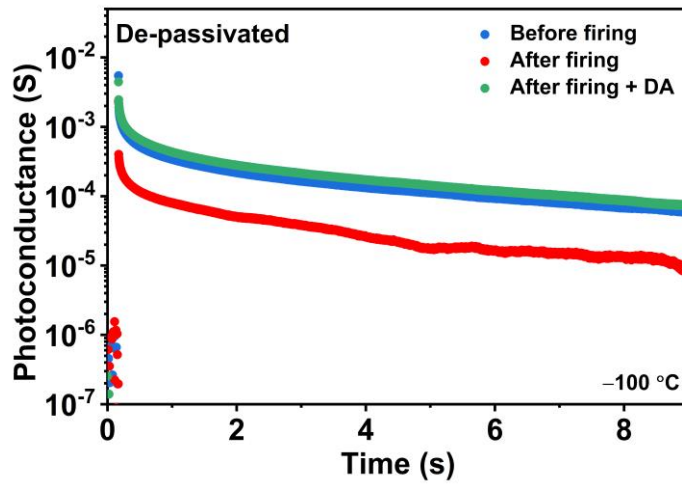


Fig. 4.8. PCD curves measured at $-100\text{ }^{\circ}\text{C}$ of a de-passivated sample before firing, after firing, and after post-firing DA (Path 5).

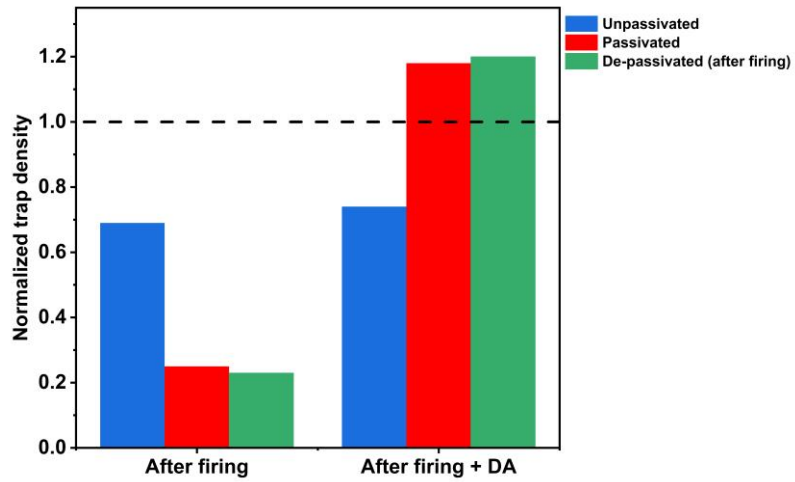


Fig. 4.9. NTD of unpassivated (blue), passivated (red), and de-passivated (green) samples after firing, and after post-firing DA at $100\text{ }^{\circ}\text{C}$.

A possible explanation for this phenomenon is the interaction between complexes in the mc-Si wafer and hydrogen released from the surface passivation during firing. Initial interaction of traps with hydrogen results in passivation of the traps [118]. As a result, their density is significantly reduced immediately after firing. If the sample is kept in the

dark after firing, the hydrogen presumably forms a new complex or is detached from the trap, thus, the traps are re-activated and the long PCD is observed again. Interestingly, the PCD decay time constant related to Trap 2 after the full recovery is 5.47 ± 0.28 sec at -100 °C which is similar to the value before firing (5.44 ± 0.29 sec). While this suggests that the source of both traps might be similar, it is not a definite conclusion, since traps with different parameters can have similar PCD time constants [44].

4.3.3 Effect of laser annealing on traps

In this section, the impact of laser annealing on the traps is investigated. Laser annealing is known to affect the lifetime of mc-Si wafers by either generating LeTID-related defects or passivating defects through hydrogenation [69, 96, 122].

In Fig. 4.10, the change in the lifetime of non-fired and fired samples (after full trap recovery) before and after laser annealing are shown. Laser annealing is done on both samples at 140 °C for 120 sec with a laser intensity of 45 kW/m^2 . Before laser annealing, both lifetime measurements are dominated by traps at low injection. However, while the lifetime of the non-fired sample is not impacted by laser annealing, the lifetime of the fired sample has a clear reduction after laser annealing, probably due to LeTID [123]. Additionally, the trap density demonstrates a strong decrease after the laser process.

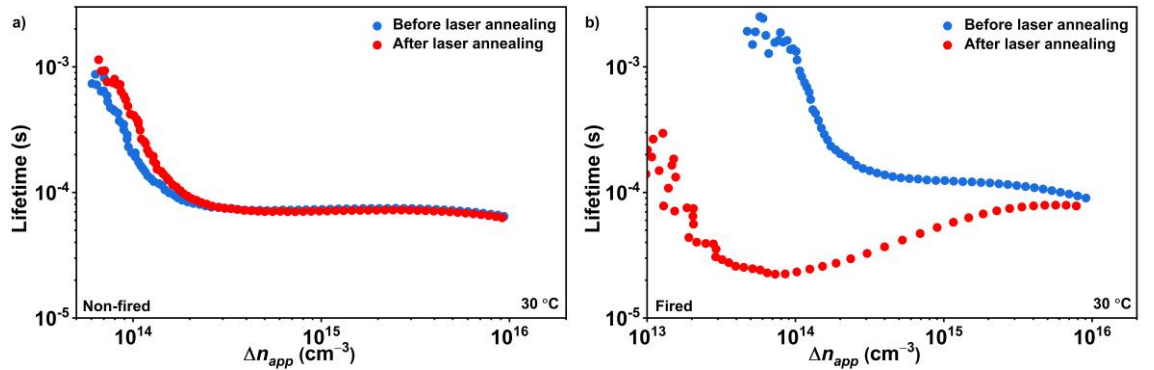


Fig. 4.10. QSSPC lifetime curves measured at 30 °C of (a) non-fired (Path 3); and (b) fired samples before and after laser annealing (45 kW/m^2 intensity) at 140 °C for 120 sec (Path 9).

In Fig. 4.11, the change in lifetime at $\Delta n = 0.1 \times N_A$ and NTD of two representative samples (fired and non-fired) before and after laser annealing are presented. While the lifetime of the non-fired sample remains almost constant (change smaller than 4%), the lifetime of the fired sample reduces by more than 50%. Interestingly, the NTD has the same trend. There is a significant reduction of almost 80% in the case of the fired sample, while the trap density of the non-fired sample stays almost the same after laser annealing

(2% change). One possible explanation for this observation is that the traps act as a precursor for the LeTID-related defects. Thus, the laser annealing transforms the trap into a defect causing a decrease in the lifetime. To investigate this hypothesis, the evolution of trap density and LeTID-related defect density during the duration of the laser annealing process was measured.

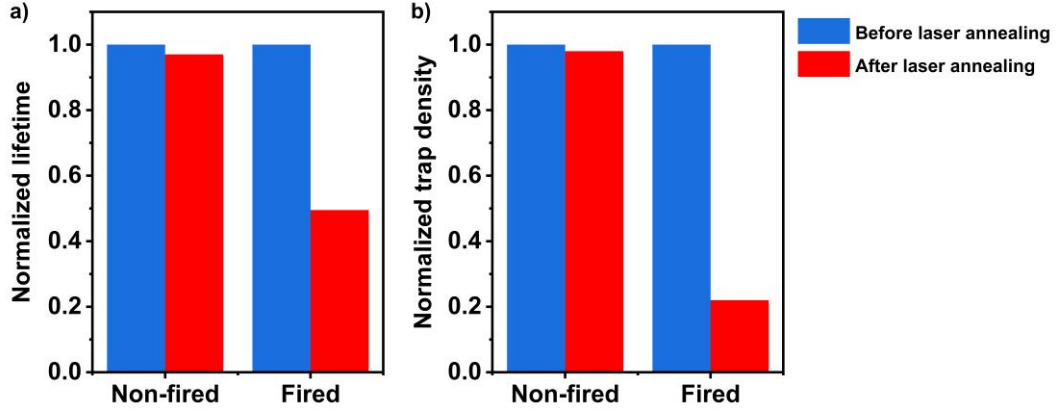


Fig. 4.11. (a) Lifetime; and (b) NTD of non-fired (blue) and fired (red) passivated samples before and after laser annealing (45 kW/m² intensity) at 140 °C for 120 sec.

In Fig. 4.12 (a), the change in the lifetime of a representative fired sample at the end of a full trap recovery and after various laser annealing durations is demonstrated. As expected, the lifetime decreases gradually with the laser annealing process and reaches its minimum after 120 sec. In Fig. 4.12 (b), the PCD curves of the sample after the same laser annealing durations are presented. Unlike the lifetime, the trap density continues to decrease beyond 120 sec of laser annealing.

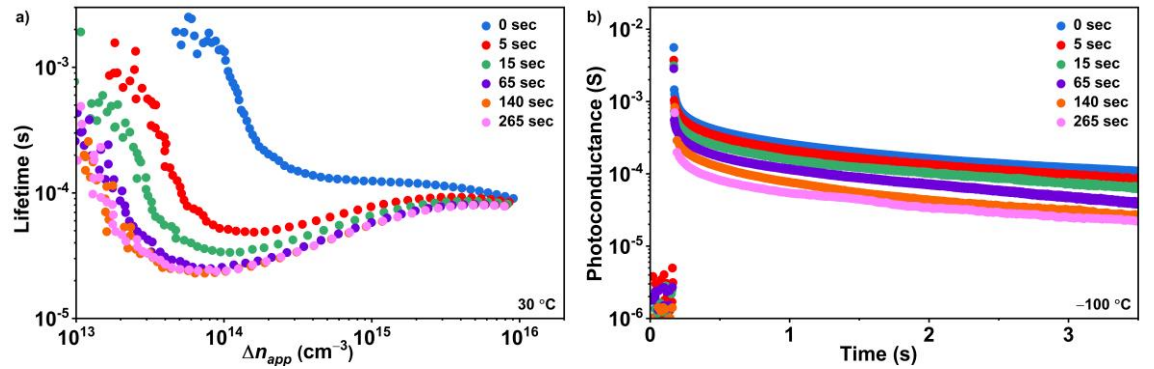


Fig. 4.12. (a) QSSPC lifetime curves measured at 30 °C; and (b) PCD curves measured at -100 °C of a sample after various laser annealing durations (Path 9).

By extracting the NDD and NTD from lifetime and PCD measurements, the rates of defect formation and trap annihilation with laser annealing are investigated. In Fig. 4.13 (a), the change in NTD and NDD of the sample is demonstrated. As mentioned, from 0 sec until 120 sec of laser annealing, the NTD reduces while the NDD increases,

demonstrating a clear anticorrelation. However, past 120 sec, the NDD reduces while the NTD further decreases and then stays almost constant. Fitting the NTD with a mono-exponential decay function, a time constant of 72.7 ± 5.3 sec is extracted. The NDD curve can be fitted only by using a double-exponential function to account for the simultaneous degradation and regeneration during laser annealing [124]. The calculated time constants for the defect formation and annihilation are 23.0 ± 3.5 sec and 989 ± 31 sec, respectively. The significantly different time constants for *trap* annihilation and *defect* formation suggest that the traps do not act as a precursor to the LeTID-related defects.

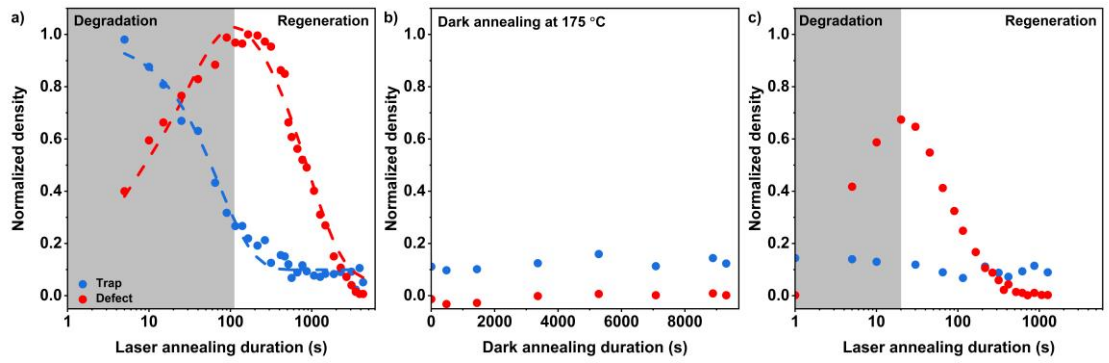


Fig. 4.13. Change in the NTD and NDD of a passivated and fired sample after full trap recovery: (a) after the first cycle of laser annealing; (b) dark annealing; and (c) after a second cycle of laser annealing. The dashed lines in (a) are mono-(trap) and double-exponential (defect) fits for the measurements.

In Fig. 4.13 (b), the change in NDD and NTD after DA of the same sample at 175 °C for 150 min is presented. Both NDD and NTD remain almost constant throughout the annealing process. This shows that unlike post-firing DA (see Fig. 4.9), post-laser annealing DA does not recover the traps. Hence, the trap annihilation after laser annealing seems to be irreversible. It also demonstrates that these traps are not correlated with BO-related degradation, as BO-related traps recover after DA (see Chapter 3) [103]. In Fig. 4.13 (c), the change in NDD and NTD after a second cycle of laser annealing is shown. In this cycle, the NDD has similar increasing and decreasing behavior with laser annealing duration. This change, however, happens in a shorter time scale with less degradation extent compared with the first cycle in Fig. 4.13 (a). The NTD, on the other hand, remains almost constant during the laser annealing process, different from the trends shown in the first cycle. This result further suggests that the LeTID-related defects and the observed traps are independent; while LeTID-related defects are recovered due to the DA, the traps are unaffected by this process. To further confirm this, LeTID in samples with different trap densities was studied. In Fig. 4.14, the change in the NDD of three passivated samples after firing is presented. The degradation of two samples was

started after full recovery of traps, either by keeping them at room temperature (labeled as “RT”) or by DA at 100 °C (labeled as “DA”). The third sample was degraded immediately after firing when the trap density is low. The sample that was degraded immediately after firing, when the trap density is very low, still shows the same degradation rate and extent as samples that were degraded after a full trap recovery.

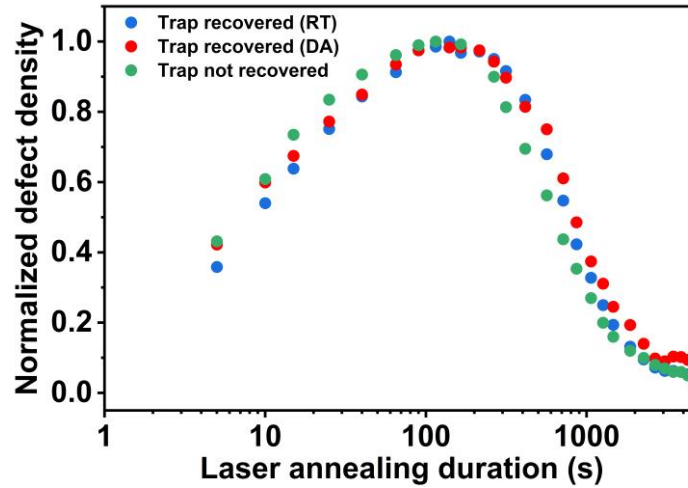


Fig. 4.14. Change in NDD of three passivated and fired samples, two degraded after full recovery of traps at room temperature (labeled as “RT”) or dark annealing (labeled as “DA”), and one was degraded immediately after firing (Paths 9, 10, and 11).

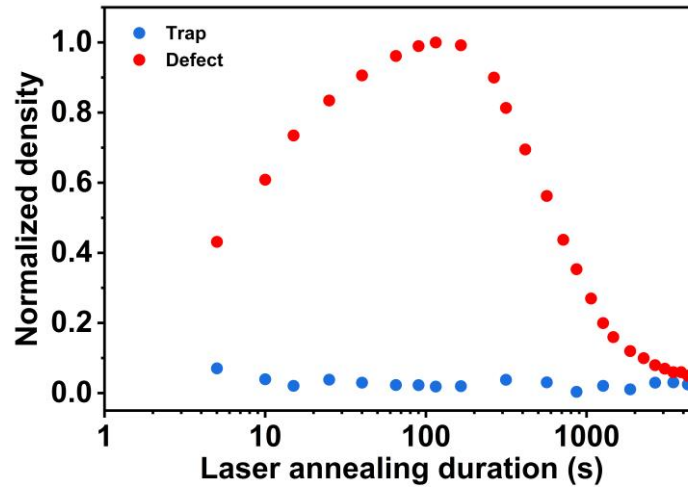


Fig. 4.15. Change in the NTD and NDD of a sample degraded immediately after firing (Path 11).

In Fig. 4.15, the change in the NTD (with respect to the trap density prior to the firing) and the NDD of the sample that was degraded before the trap recovery is presented (NDD is the same as in Fig. 4.14). In contrast to the observed anti-correlation between NTD and NDD in Fig. 4.13, the trap density is constant throughout laser annealing of the sample while the NDD has its characteristic degradation and regeneration behavior. This further suggests that the generation of defects is not due to the annihilation of traps, as no change in the trap density is observed throughout the laser annealing process. Thus, it can be

concluded that while the trap annihilation might be related to the passivation of traps via hydrogenation, it is not correlated with LeTID.

4.3.4 Impurity-related defects as a trapping center source

In Section 4.3.1, impurities and structural defects were suggested as possible sources of the observed traps. In this and the following section, these two possibilities are investigated. Since the measured samples in the previous sections have been gettered, it is assumed that the density of metallic impurities is small, suggesting that these impurities are not the source of the observed traps. To confirm this, the impact of two well-known metallic impurities in mc-Si, iron (Fe) and nickel (Ni) [125], on the trap densities is further investigated. For this purpose, another set of B-doped mc-Si wafers with a thickness of $196 \pm 5 \mu\text{m}$ and resistivity of $2.25 \pm 0.08 \Omega \cdot \text{cm}$ was used. Five sister samples were saw damage etched and gettered with a recipe similar to the one described in Section 4.2. This was followed by the removal of the diffused layer. Afterward, one sample was ion-implanted with Fe and the second sample with Ni. After the ion implantation, the two samples were annealed to distribute the impurities uniformly across the wafer. Two additional samples were annealed at the same conditions as reference samples. The labels used for the samples as well as the details of the implantation and annealing conditions are presented in Table 4.1. After the implantation, the surface of the samples was passivated with a PECVD $\text{AlO}_x\text{-SiN}_x$ stack.

Table 4.1. Implantation and annealing conditions of mc-Si samples used for the investigation of traps in contaminated samples.

Sample	Fluence (cm^{-2})	Annealing temperature ($^{\circ}\text{C}$)	Annealing duration (s)
R	-	-	-
R-Fe	-	900	3,600
I-Fe	1.5×10^{10}	900	3,600
R-Ni	-	800	600
I-Ni	6×10^{12}	800	600

The PCD curves of Samples R-Fe and I-Fe are shown in Fig. 4.16 (a) and the PCD curves of R-Ni and I-Ni samples are shown in Fig. 4.16 (b). The PCD curve of the R sample is presented in both figures as a reference. As expected, the PCD curve of the R samples shows a long PCD tail. Since the passivation layer has a negative fixed charge, the observed effect can be attributed to the traps and not DRM. Focusing on the Fe-implanted sample, the signal of the PCD measurement is almost identical to the R sample,

suggesting that Fe is not the source of this trap. Comparing the PCD curves of R and R-Fe samples, it can also be said that the annealing process does not impact the trap density. The same conclusion can be drawn for the Ni-implanted sample. The small difference in trap densities of I-Ni compared with R-Ni and R might be due to a slight error in the measurement, considering that the mc-Si measurement is significantly location-dependent. It should be noted that if Ni is the source of traps, an increase in the trap density should have been observed in the PCD signal. In conclusion, considering that all the samples have been gettered and Fe- and Ni-contaminated samples did not demonstrate an increase in trap density, it is likely that impurities are not the source of these traps.

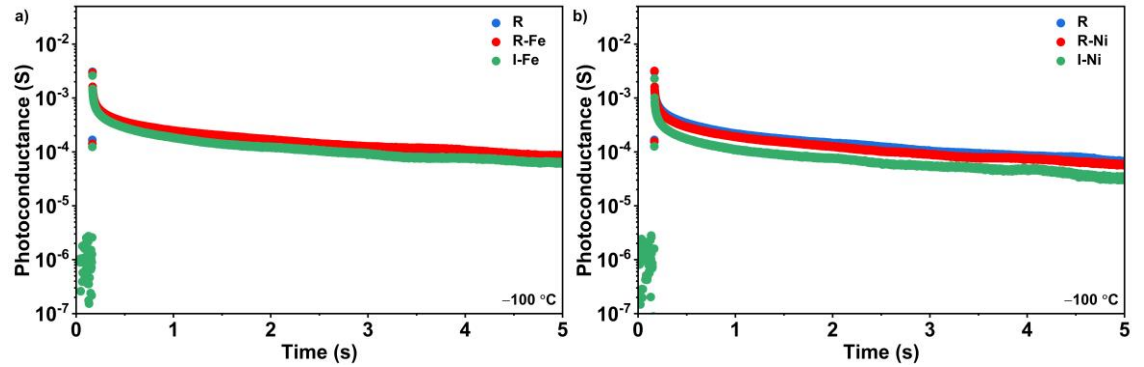


Fig. 4.16. PCD curves measured at $-100\text{ }^{\circ}\text{C}$ of samples implanted with (a) Fe; and (b) Ni, and their respective non-implanted and/or non-annealed references.

4.3.5 Structural defects as a trapping center source

To investigate the possibility of structural defects (i.e., dislocations and grain boundaries) being a source of traps in mc-Si wafers, a set of five B-doped **mono-cast** silicon samples were prepared. Two samples were from one 6-inch wafer (Wafer 1, $1.58 \pm 0.05\text{ }\Omega\cdot\text{cm}$; $194 \pm 7\text{ }\mu\text{m}$) and the other three from another wafer from the same ingot, however, from different location and height (Wafer 2, $1.78 \pm 0.04\text{ }\Omega\cdot\text{cm}$; $194 \pm 3\text{ }\mu\text{m}$). All the samples were saw damage etched using alkaline etching and measured without surface passivation. Mono-cast silicon wafers (also known as mono-like or cast-mono) are wafers grown from a monocrystalline seed using the casting method [126]. In these wafers, the structural defects are formed during the solidification stage as the ingot grows [126]. As a result, areas with different structural defect densities are generated after the growth. Since the growth method is similar to mc-Si (casting), it is assumed that the structural defects present in both wafer types are similar. Since the present samples have areas with different structural defects in a 6-inch silicon wafer, it is possible to separate the impact of each defect on trap density. To differentiate between different regions of the samples,

PL images were taken at room temperature using an 808 nm laser with 10 suns intensity with an acquisition time of 9.5 sec. While the PL image shows the presence of structural defects, it is challenging to differentiate between dislocations and grain boundaries in these samples. For this purpose, electron backscatter diffraction (EBSD) measurements [127] were performed.

In Fig. 4.17, the PL images and EBSD maps of two samples from Wafer 1 are presented. Both samples have a high density of structural defects, clearly visible in the PL images. In Fig. 4.17 (a), a PL image of a sample with dislocations but without any grain boundaries is shown. The nature of the structural defects is identified using an EBSD measurement on a representative region. As shown in Fig. 4.17 (a), the EBSD measurement does not show any anisotropy in crystal orientation in the marked region, suggesting that this sample is indeed a single crystal. It should be noted that the region chosen for EBSD measurement demonstrates all the observed features present in the PL image, suggesting that this region is a representation of the whole sample. On the other hand, the EBSD map of the second sample, shown in Fig. 4.17 (b) points out the fact that different grains (and thus, grain boundaries) are present in it. Besides using EBSD measurement, this can be inferred from the PL image. Since the samples have been etched with an alkaline solution, varying crystal orientations have different reflectance after the etching process, leading to unequal PL intensities in the different grains [128]. Moreover, each plane has different surface recombination rates which is the dominant contributor to the PL intensity in bare wafers [129]. Thus, the difference in the PL image intensity in different regions is presumably due to the presence of different grains which in turn suggests the presence of grain boundaries. The total length of the grain boundaries of this sample for the measured region is calculated to be 5.62 cm. The samples used in this section are labeled based on the type of structural defects present in them. These labels are shown in Table 4.2.

Table 4.2. Labels for mono-cast wafers used for investigation of trapping sources in mc-Si.

Sample label	Wafer number	Structural defects
MC1-D	1	Dislocations
MC1-DG	1	Dislocations and grain boundaries
MC2	2	None
MC2-D	2	Dislocations
MC2-DG	2	Dislocations and grain boundaries

With structural defects being differentiated, the PCD measurements were performed on both samples (MC1-D and MC1-DG) to investigate the traps. The results for the PCD measurements are shown in Fig. 4.18. No long PCD tail is observed in the sample with dislocations and without grain boundaries (MC1-D). On the other hand, the long PCD curve is visible in the sample with dislocations and grain boundaries (MC1-DG). As the samples have no passivation and the TDDs are removed, it can be suggested that this decay is due to the presence of traps that are non-related to TDDs. *It can be concluded that this trap is due to the presence of grain boundaries and not the dislocations.* The trap can also be related to the impurities *decorating the grain boundary*, as it has been shown previously that the type of impurities in these two structural defects are not always similar [130]. Consequently, it can be suggested that traps observed in the mc-Si wafers are likely due to the grain boundaries and not the dislocations or the impurities.

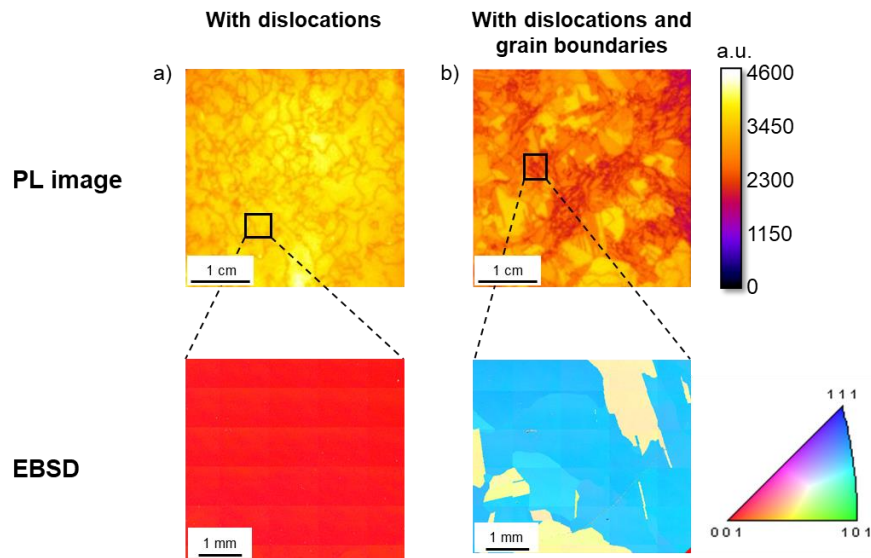


Fig. 4.17. PL images and EBSD maps of two mono-cast silicon samples from Wafer 1, from areas with: (a) dislocations only; and (b) both grain boundaries and dislocations.

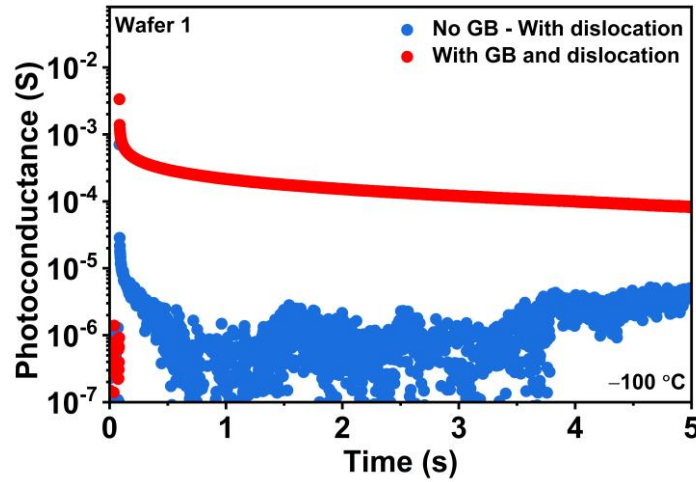


Fig. 4.18. PCD curves measured at $-100\text{ }^{\circ}\text{C}$ of samples MC1-D (No GB) and MC1-DG (With GB).

To confirm this, Wafer 2 (which is from a different area of the ingot) was chosen and the same measurement procedure was performed on this wafer. Besides the two areas mentioned before, this wafer also contains an area without any structural defects. The PL image and EBSD maps of three samples from three different areas are shown in Fig. 4.19. The sample presented in Fig. 4.19 (a) has no structural defects (MC2) while the sample in Fig. 4.19 (b) only has dislocations (MC2-D), and the sample in Fig. 4.19 (c) has dislocations and grain boundaries (MC2-DG). Like the previous samples, this can be inferred from the PL images and is confirmed with EBSD measurements.

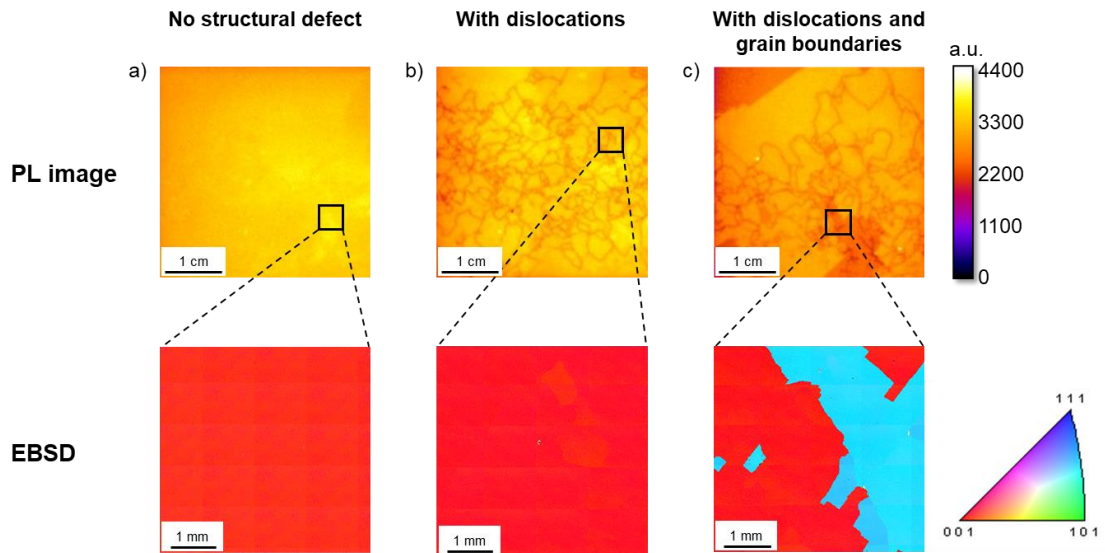


Fig. 4.19. PL images and EBSD maps of three mono-cast silicon samples from Wafer 2, from areas with: (a) no structural defects; (b) dislocations only; and (c) grain boundaries and dislocations.

The PCD measurements for these samples are shown in Fig. 4.20. As expected, the PCD measurement of MC2 (no structural defects) and MC2-D (dislocations only) samples do not show a long PCD tail. In contrast, the MC2-DG sample (with dislocations

and grain boundaries) has a PCD curve with a long decay, suggesting that this sample is impacted by traps. The total length of the grain boundaries in the region chosen for EBSD measurement of the MC2-DG sample is 2.76 cm which is 51% lower than MC1-DG. This might be the reason behind the lower measured trap density (49%) compared to MC1-DG.

As mentioned previously, a possible source of the long PCD tail is the high mobility of majority carriers under illumination due to the reduction in the charge barrier around grain boundaries. However, it is worth reiterating that this effect is shown to be negligible at light intensities lower than 1×10^{-5} suns. As mentioned previously, this light intensity is reached $\sim 630 \mu\text{s}$ after the excitation. Thus, it can be concluded that the current observation is not related to this phenomenon.

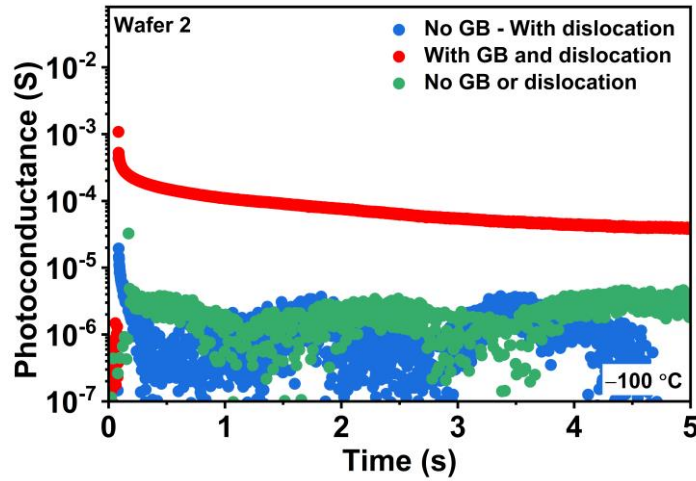


Fig. 4.20. PCD curves measured at $-100\text{ }^{\circ}\text{C}$ of samples MC2 (no structural defects), MC2-D (dislocations only), and MC2-DG (dislocations and grain boundaries).

4.4 Chapter summary

A trap-related long PCD measurement was observed in B-doped mc-Si wafers. It was shown that these long time constants cannot be due to the DRM or changes in the charge barrier near the grain boundaries. Thus, this PCD was associated with the presence of traps in B-doped mc-Si wafers. It was shown that this trap is not due to the TDDs or BO-related traps.

This long PCD measurement was associated with two traps having time constants of 0.14 ± 0.1 sec (Trap 1) and 1.87 ± 0.43 sec (Trap 2) at $30\text{ }^{\circ}\text{C}$. Additional investigations of Trap 2 indicated that firing the samples (passivated with SiN_x) results in a significant reduction in the density of these traps. After storing the samples at room temperature in

the dark for several days or DA the samples at 100 °C for a few hours, the traps were generated again. However, such a change was not observed in samples without a hydrogen-rich surface passivation dielectric layer, suggesting that this metastable change in trap densities might be related to the hydrogen released from the surface passivation during the firing process.

It was shown that laser annealing of the fired sample permanently annihilates the traps while generating LeTID-related defects. Such a change is not observed in non-fired samples. Unlike firing, the annihilation of traps after laser annealing seems to be permanent. It was shown that the rates for defect formation and trap annihilation are different. Moreover, when a sample with low trap density (immediately after firing) was laser annealed, the degradation rate and extent were identical to the sample after full recovery of traps (with DA or storage at room temperature). Thus, it can be concluded that there is no correlation between defect generation and trap annihilation in the case of LeTID.

In addition to the trap being observed in samples after gettering, it was shown that Fe and Ni implantation does not increase the trap densities. Thus, it can be suggested that these two metallic impurities are not the source of the observed traps. However, other metallic impurities, accumulated at the grain boundaries, might be the source of these traps. Finally, the likely source of the trap was determined. By measuring mono-cast silicon wafers from different regions of the ingot, with different combinations of structural defects, it was shown that grain boundaries are the source of the observed traps, and not dislocations.

Chapter 5

Investigation of Light-Induced Degradation in Gallium- and Indium-Doped Czochralski Silicon¹

LID in B-doped Cz wafers is an important problem that impacts commercial *p*-type solar cells. To reduce the impact of BO-related degradation on cell efficiencies, Ga- and In-doped Cz wafers have been suggested as a substitute for B-doped wafers [77, 78]. Moreover, the observations regarding the presence of LID in these two materials are inconclusive [78, 82-84, 87, 88]. It was stated that between Ga- and In-doped wafers, Ga-doped wafers are considered more suitable to replace B-doped wafers [81]. This has motivated several studies investigating Ga-doped wafers [85, 86, 131]. It has been suggested that as-received Ga-doped wafers demonstrate very high lifetimes equal to the values observed in gettered B-doped Cz wafers that have been stabilized to remove the impact of BO degradation [84]. A firing step seems necessary to observe LID in Ga-doped wafers [85, 131]. It was shown that a prolonged light soaking results first in the degradation and then in the recovery of the lifetime while further light soaking does not degrade the lifetime anymore [83]. It is also shown that the thermal history of Ga-doped wafers and cells has a significant impact on LID behavior. In a study by Grant *et al.*, it was shown that pre-light soaking DA at temperatures higher than 200 °C and up to 300 °C increases the degradation extent in Ga-doped cells [83]. However, after DA, no degradation was observed after stripping the cells of metallization, passivation layers and the diffusion layer, and then re-passivating the wafers with ALD AlO_x annealed at 420 °C [83]. This suggests that the thermal budget during annealing annihilated the LID-related defects generated during DA [83]. Several studies have been performed to investigate the LID-related defect in Ga-doped wafers. In addition to the extraction of the activation energies for formation and removal with extended light soaking [85, 131], the *k* value of the LID-related defects has also been extracted [85, 132]. These values have been

¹ This chapter is partially based on:

S. Jafari, and Z. Hameiri, in 48th *IEEE Photovoltaics Specialists Conference (PVSC)*, 2021.

extracted using injection-dependent lifetime spectroscopy (IDLS) measurement method, with the assumption of an energy level at the mid-gap [85, 132]. However, as discussed in Chapter 2, a single injection-dependent lifetime measurement is insufficient to extract reliable, accurate values for k . Moreover, the defect energy level cannot be determined with IDLS method.

In this chapter, LID in both Ga- and In-doped Cz wafers is investigated. First, the change in the lifetime during light soaking is investigated. The defect formation rates are measured at different temperatures and the defect formation activation energies are extracted. Defect annihilation with DA is investigated and, subsequently, the activation energies for defect annihilation are measured. Using TIDLS measurements, the parameters of the defect causing LID in Ga-doped wafers are extracted. Finally, PCD measurements are performed to investigate traps in Ga-doped wafers and their potential correlation with LID in this material.

5.1 Materials and methods

For the lifetime-based studies, a set of B- ($167 \pm 2 \mu\text{m}$; $1.65 \pm 0.03 \Omega \cdot \text{cm}$), Ga- ($189 \pm 2 \mu\text{m}$; $1.80 \pm 0.04 \Omega \cdot \text{cm}$), and In-doped ($166 \pm 3 \mu\text{m}$; $3.30 \pm 0.12 \Omega \cdot \text{cm}$) Cz wafers were used. Using FTIR measurements, the $[\text{O}_i]$ was measured to be $5 \times 10^{17} \text{ cm}^{-3}$ for the B- and In-doped wafers and $6 \times 10^{17} \text{ cm}^{-3}$ for the Ga-doped wafers. For trap studies using PCD measurements, a set of Ga-doped Cz wafers with a thickness of $178 \pm 4 \mu\text{m}$ and resistivity of $3.1 \pm 0.08 \Omega \cdot \text{cm}$ was used. All the wafers were gettered using a P-diffusion at 840°C for 45 min. The diffused layer was then etched off and the wafers were passivated with a 75 nm SiN_x , deposited using a PECVD system with a refractive index of 2.08 at 632 nm [92]. After passivation, the wafers used for lifetime measurements were fired at a peak temperature of 900°C using a SCHMID belt furnace. When needed, the passivation layer was removed using a 5% HF solution. For the degradation process, the samples were illuminated at various temperatures using halogen lamps with 0.4 suns or 0.1 suns equivalent intensity. For DA, the samples were annealed on a hot plate. In both degradation and DA processes, the reported temperature is the sample temperature as measured by two k-type thermocouples (CHAL-005 OMEGA) attached to a sample from the same sample set being measured.

For the room temperature lifetime measurements, a Sinton Instrument WCT-120 lifetime tester was used. For TIDLS and PCD measurements, the system described in Chapter 3 was used. For TIDLS measurement, the lifetime was measured in the $-50\text{ }^{\circ}\text{C}$ to $50\text{ }^{\circ}\text{C}$ temperature range while for PCD measurements, the PC signal was acquired in the $21\text{ }^{\circ}\text{C}$ to $45\text{ }^{\circ}\text{C}$ temperature range.

5.2 Results and discussion

5.2.1 Kinetics of LID in Ga- and In-doped Cz silicon

In Fig. 5.1, the change in lifetime at $\Delta n = 1 \times 10^{15}\text{ cm}^{-3}$ of representative B-, Ga-, and In-doped samples during light soaking at 0.4 suns and $80\text{ }^{\circ}\text{C}$ are presented. The B-doped sample has the highest degradation extent with a maximum lifetime reduction of 82% after $\sim 40,000$ sec. The Ga- and In-doped samples show a maximum lifetime reduction of 65% after $\sim 20,000$ sec and 77% after $\sim 450,000$ sec, respectively. The lifetime returns to its initial value after DA. The details of the DA leading to the recovery of sample lifetimes will be discussed in more detail. This suggests that the Ga- and In-doped Cz wafers are likely to have “degraded” and “annealed” states similar to the states observed in LID [52] and LeTID [74]. It has been shown that the rate and extent of LID [52, 103], as well as the extent of LeTID [133] in B-doped wafers, can be doping-dependent. It is possible that such a correlation might be present for Ga- and In-doped samples as well. Thus, care should be taken when comparing the degradation rate and extent of the In-doped samples with the other two dopants. While the doping density of B- and Ga-doped samples are similar ($8.8 \times 10^{15}\text{ cm}^{-3}$ and $8.1 \times 10^{15}\text{ cm}^{-3}$, respectively) and both are almost fully ionized at $80\text{ }^{\circ}\text{C}$ ($> 99\%$), the In-doped sample has a lower doping density ($5.5 \times 10^{15}\text{ cm}^{-3}$) with lower ionization extent ($\sim 90\%$) at this temperature [80].

As mentioned, previous findings regarding the degradation of Ga- and In-doped Cz wafers are inconclusive. In some studies, no degradation was observed [78, 134], whereas several recent investigations have shown degradation in both wafers and cells made from these materials [83, 84, 87]. The reason behind the different observations regarding the presence of LID in Ga-doped wafers is yet to be determined, however, a recent study has suggested that an unintentional presence of B in Ga-doped cells might have an impact on the observed degradation, although the density of this B contamination is very low ($< 1 \times 10^{14}\text{ cm}^{-3}$) [84]. It has been suggested that pre-degradation DA can also have an

impact on the degradation behavior of Ga-doped solar cells [83, 84]. Degradation in In-doped wafers has also been observed in several studies [87, 135]. Similar to Ga, the reason behind the different observations regarding LID in In-doped wafers is not clear yet.

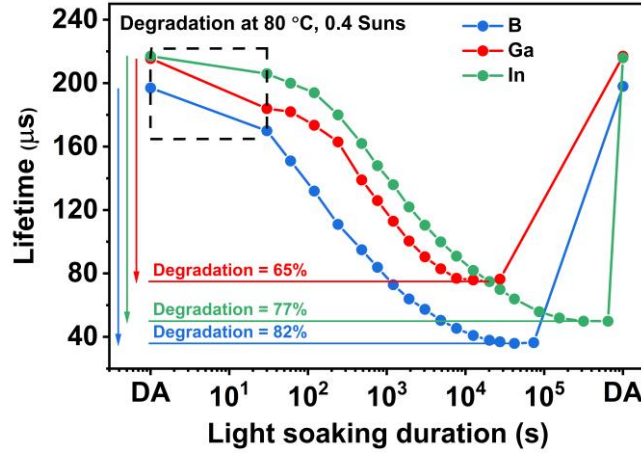


Fig. 5.1. The lifetime of B-, Ga-, and In-doped samples as a function of light soaking duration at 0.4 suns and 80 °C.

For short light soaking durations in Fig. 5.1 (marked with a square), an abrupt decrease in the lifetime can be observed for the Ga-doped and the B-doped samples while a smaller reduction is detected for the In-doped sample. To further investigate this region, two samples were degraded using a lower illumination intensity of 0.1 suns, at 28 °C for Ga and 50 °C for In. Due to the lower insolation and temperature compared to conditions in Fig. 5.1, the changes in the lifetime are slower, allowing easier monitoring of the lifetime change at shorter time scales. The higher temperature used for the In-doped sample was because no degradation was observed at 28 °C after 50 hours of light soaking. To remove the impact of Fe on the measurements (by forming Fe-Ga and Fe-In pairs), in addition to gettering, the samples were light-soaked using the flash of the lifetime tester to dissociate the pairs. This was done until no change in the lifetime was observed with additional flashing.

In Fig. 5.2, the change in lifetime (left y-axis, blue) and NDD (right y-axis, red) of Ga- and In-doped samples during degradation are presented. The Ga-doped sample demonstrates a clear two-step degradation, resulting in: (i) a ~13% reduction in the lifetime within a few minutes; followed by (ii) a second, much slower degradation step. A two-step degradation process in Ga-doped wafers during light soaking has also been observed in another study [85]. Furthermore, a similar two-step process has been previously reported for LeTID of B-doped mc-Si wafers [136]. The In-doped sample seems stable in comparison until ~1,000 sec of light soaking.

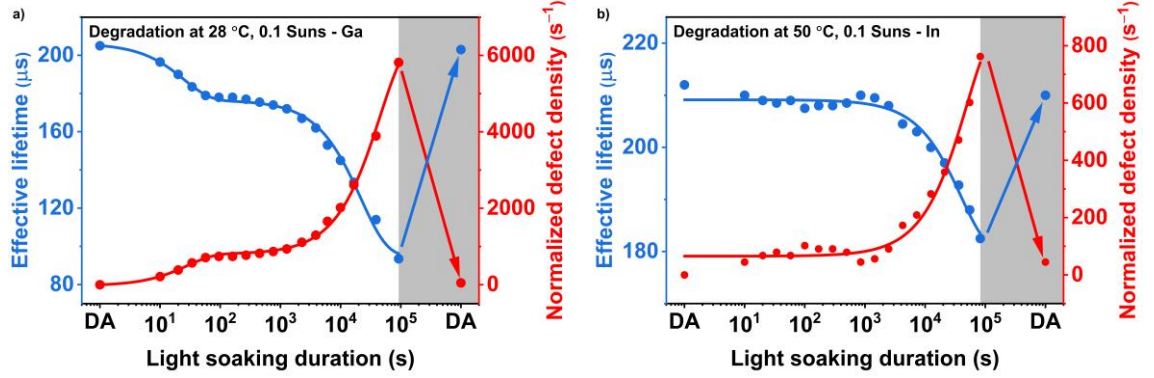


Fig. 5.2. The lifetime and NDD of (a) Ga-; and (b) In-doped wafers as a function of light soaking duration at 0.1 suns, 28 °C for Ga and 50 °C for In. The solid lines are double- (Ga) and single-exponential (In) fits to the data.

Defect formation

To extract the activation energies of defect formation, degradation was conducted at seven temperatures between 50 °C to 155 °C and the defect formation rate was determined at each temperature. For this purpose, the NDD at each temperature as a function of light soaking duration were fitted with a double-exponential function for the B- and Ga-doped samples, and a single-exponential function for the In-doped sample. For both B- and Ga-doped samples, only the activation energies of the slow step degradation were extracted.

The Arrhenius plot generated from these defect formation rates is shown in Fig. 5.3. The extracted activation energies for B-, Ga-, and In-doped wafers are summarized in Table 5.1. The values for B- and In-doped Cz samples are similar to previously reported values of 0.94 ± 0.06 eV for LeTID-related defect formation in B-doped mc-Si wafers [136]. Regarding the In-doped sample, the extracted activation energy has a slightly higher margin of error suggesting that the fit quality is lower. This may be due to the considerable change in the dopant ionization percentage for In-doped samples, from 85% at 50 °C to 96% at 155 °C [80]. Therefore, the degradation happens with different background doping at different temperatures, which may cause a slight shift in the degradation rate.

An activation energy of 0.58 ± 0.04 eV has been determined in a previous study for the generation of LID-related defects in the temperature range 90 °C to 140 °C for Ga-doped Cz wafers [131]. In the same study, a deviation from the reported value at temperatures below 90 °C was observed [131], while such deviation is not observed here in the range of 50 °C to 155 °C. Moreover, in Ref. [131] the degradation curves were fitted with a single-exponential function, assuming a one-step degradation process, which might have

caused an error in the extracted activation energy. In another study, the activation energy of the slow step defects was determined to be 0.90 ± 0.05 eV in the range of 100 °C to 160 °C [85]. The difference in light intensity used to induce the degradation process (0.4 suns vs. 0.7 suns) might be the source of the observed discrepancy between the extracted activation energies; it has been suggested that the degradation rate can be affected by the illumination intensity [86].

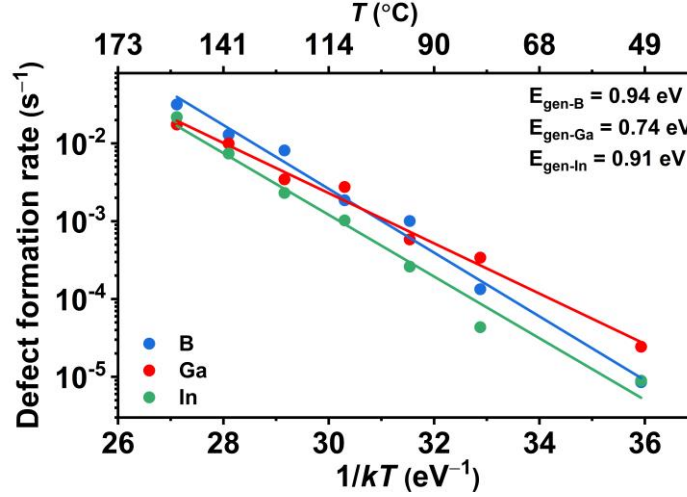


Fig. 5.3. Temperature dependence of the defect formation rates in B-, Ga-, and In-doped Cz wafers due to light soaking at 0.4 suns between 50 °C to 155 °C. The investigated defects for B- and Ga-doped wafers are the slow-formed defects. The solid lines are exponential fits to the data.

Table 5.1. Activation energies of LID- and LeTID-related defect formation in B-, Ga-, and In-doped Cz wafers from this study and literature.

Defect type	Activation energy (eV)		
	Fit	Literature	
LID in B-doped Cz	0.94 ± 0.12	0.48 ± 0.04 [103]	-
LID in Ga-doped Cz	0.74 ± 0.10	0.58 ± 0.04 [131]	0.90 ± 0.05 [85]
LID in In-doped Cz	0.91 ± 0.15	-	-
LeTID in B-doped mc-Si	-	0.94 ± 0.06 [136]	-

Defect annihilation

Prior work has suggested that the generated LID- and LeTID-related defects in B-doped wafers can be annihilated with DA [52, 75]. This was shown in Fig. 5.1, where the lifetime of Ga- and In-doped wafers also recovered after a post-LID DA. To investigate the kinetics of defect annihilation with DA, a set of three fully degraded samples with B, Ga, and In doping were dark annealed at 170 °C. The change in lifetime at $\Delta n = 1 \times 10^{15} \text{ cm}^{-3}$ for these three samples is shown in Fig. 5.4. For the B-doped sample, the lifetime initially recovers before reducing with further DA after $\sim 5,000$ sec. This has been observed previously and has been attributed to the formation of LeTID-related defects during the DA process [124]. Apart from this simultaneous defect formation

during the DA process in the B-doped sample, the initial lifetime recovery seems to happen in a single step. In contrast, the lifetime recovery (defect annihilation) of Ga-doped wafers during DA happens in two steps: one fast process and one slow. The former step is completed at around 1,000 sec while the second step extends past 100,000 sec. Similarly, the In-doped sample shows a two-step lifetime recovery throughout the DA process. Neither Ga- nor In-doped samples demonstrate a reduction in the lifetime within the prolonged DA duration investigated here ($> 200,000$ sec).

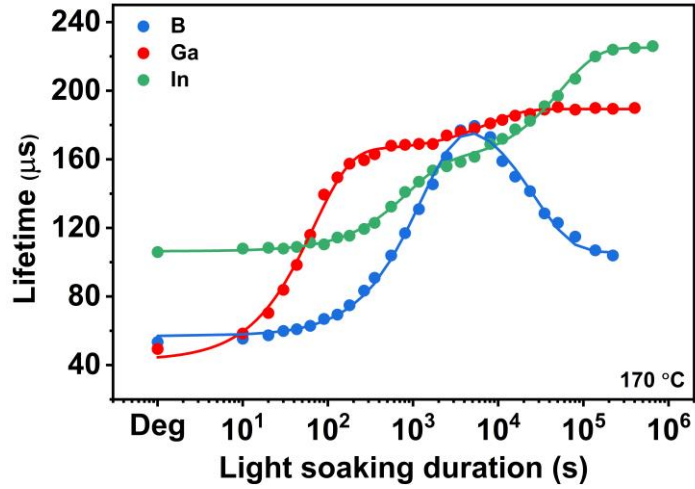


Fig. 5.4. The lifetime of B-, Ga-, and In-doped samples as a function of DA duration at 170 °C. The solid lines are double-exponential fits to the data (one growth and one decay function for B, and two growth functions for Ga and In).

To extract the activation energy for the annihilation of LID-related defects in Ga- and In-doped Cz wafers, the change in lifetime during DA was measured at seven different temperatures in the range of 140 °C to 200 °C in 10 °C intervals. The NDD extracted from lifetime was plotted as a function of DA time and subsequently fitted with a double-exponential function to extract the defect annihilation rates. The Arrhenius plots for the defect annihilation rates are provided in Fig. 5.5. For the extraction of the defect annihilation rate in the fast step for the Ga-doped sample, only the data up to 180 °C has been used, since at higher temperatures, the initial lifetime recovery happens in time scales close to the minimum measurement time intervals of 10 sec.

The Arrhenius plot for the fast step annihilation is shown in Fig. 5.5 (a). The extracted activation energies for the fast step of defect annihilation in Ga- and In-doped samples are 1.61 ± 0.04 eV and 1.40 ± 0.09 eV, respectively. While only a single regime is realized for the activation energy of the fast step of defect annihilation throughout the whole temperature range, the annihilation of defects in the slow step shows two activation energies for both samples, as shown in Fig. 5.5 (b). For the Ga-doped sample, the

annihilation rate seems to become temperature independent for temperatures lower than 150 °C, whereas at higher temperatures it follows an exponential increase with an activation energy of 1.86 ± 0.10 eV. For the In-doped sample, two activation energies can be extracted for two temperature ranges, 2.51 ± 0.11 eV for temperatures higher than ~ 180 °C and 0.90 ± 0.08 eV at temperatures lower than ~ 160 °C. These values are summarized in Table 5.2.

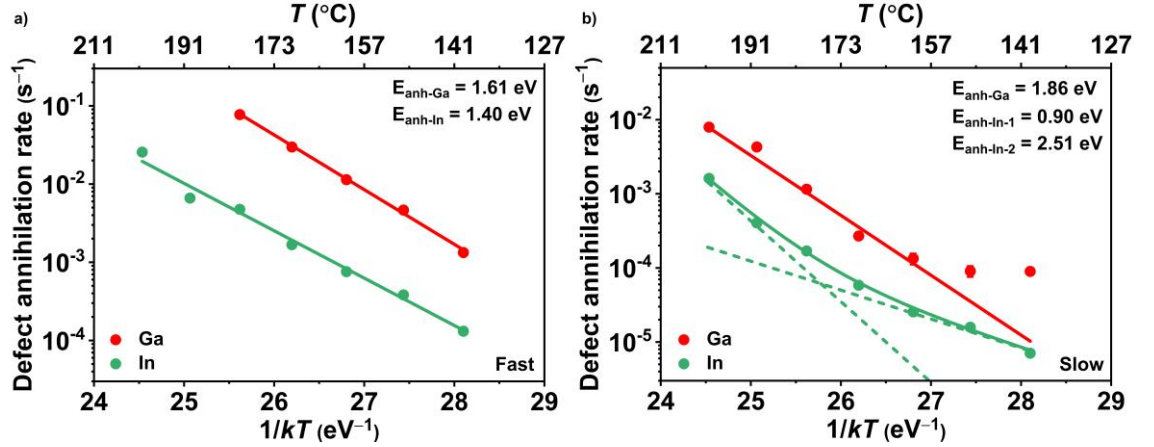


Fig. 5.5. Temperature-dependent defect annihilation rates of the (a) fast; and (b) slow steps in Ga- and In-doped wafers. The error bars of the extracted rates are smaller than the marker size. The solid lines are single- (Ga-fast, In-fast, Ga-slow) and double-exponential (In-slow) fits to the data.

Considering that Ga-doped samples have two-step degradation and regeneration processes, it is not yet clear whether two sets of defects are formed and annihilated during light soaking and DA, or one set of defects has a two-step formation and annihilation process. For In-doped samples, on the other hand, it is more likely that one set of defects is formed (one-step degradation), that are annihilated in two steps, based on the results in Fig. 5.2 and Fig. 5.4.

Table 5.2. Activation energies of the fast and slow steps of LID-related defect annihilation in Ga- and In-doped Cz wafers, measured at 140 °C to 200 °C.

Defect	Step type	Activation energy (eV)
Ga-doped Cz	Fast	1.61 ± 0.04
	Slow	1.86 ± 0.10
In-doped Cz	Fast	1.40 ± 0.09
	Slow #1	2.51 ± 0.11
	Slow #2	0.90 ± 0.08

5.2.2 Analysis of LID-related defects in Ga-doped Cz silicon

Ga has replaced B as a *p*-type dopant in silicon wafers used for PV applications [13]. For this reason, this chapter will focus on more detailed investigations of Ga-doped wafers from this point onwards. To better understand the defect causing LID in Ga-doped

wafers, TIDLS measurement was performed using a representative Ga-doped sample and the k -DPSS curves were generated to extract the defect parameters. The effective lifetime curves of the sample before and after degradation as well as the LID-related SRH lifetime component (τ_{LID}) are shown in Fig. 5.6. The SRH lifetime is extracted using the method described in Chapter 2. A significant drop in the lifetime is observed, in particular at the low injection range, which is presumably due to the generation of a recombination-active defect in the bulk after light soaking.

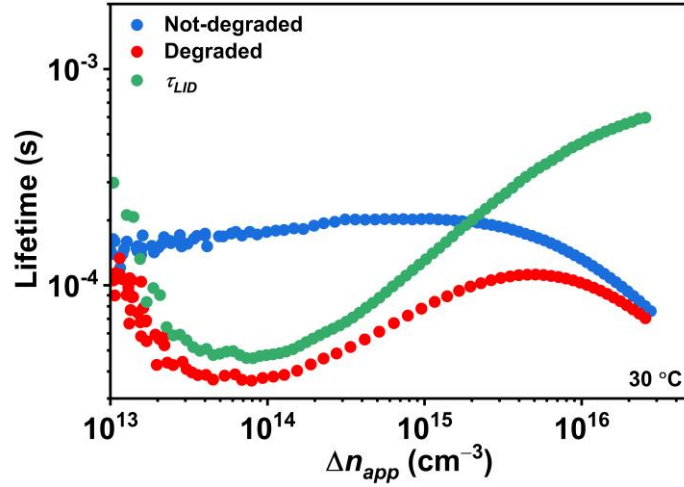


Fig. 5.6. Lifetime curves of a Ga-doped wafer measured at 30 °C, before (blue) and after (red) degradation. The LID-related lifetime component (green) is also presented.

To perform the DPSS analysis, the lifetime curves of the sample were measured in the $-50\text{ }^{\circ}\text{C}$ to $50\text{ }^{\circ}\text{C}$ temperature range using $25\text{ }^{\circ}\text{C}$ intervals. The lifetime curves are linearized and fitted with two SRH defects using the method discussed in Chapter 2. To provide an example, the linearized lifetime measured at $-50\text{ }^{\circ}\text{C}$ and the corresponding fitted SRH lifetimes are shown in Fig. 5.7 (a). Since the linearized lifetime curve cannot be fitted with a single straight line, it is assumed that more than one defect is affecting the lifetime curve. One of these SRH defects is more dominant in the low injection range (dominant defect), while the second one is affecting the high injection range (second defect). Another possibility is having a two-level defect affecting the lifetime after the LID. For the following discussion, two single-level defects are assumed to be present in the bulk.

The dominant defect is first investigated. The fitted SRH lifetime curves for the dominant defect are shown in Fig. 5.7 (b). As the temperature is increased, the lifetime curves become more linear and the fitted SRH curve gets closer to the experimental data

at high injection levels, meaning that the contribution of the second defect on the total lifetime curve becomes smaller.

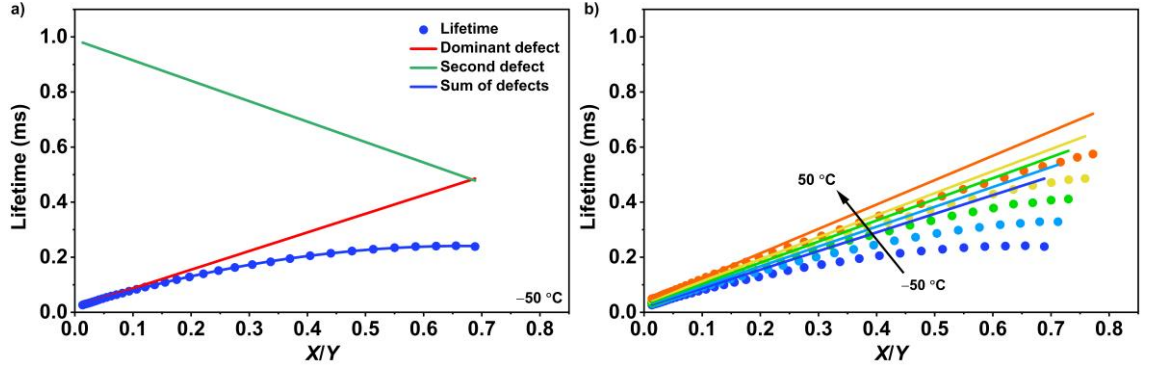


Fig. 5.7. (a) Linearized LID-related lifetime curve of the Ga-doped wafer at $-50\text{ }^{\circ}\text{C}$. The solid lines are the fitted SRH lifetime curves for the dominant defect (red), second defect (green), and the sum of the two defects (blue). (b) Linearized LID-related lifetime curves of the same wafer in the $-50\text{ }^{\circ}\text{C}$ to $50\text{ }^{\circ}\text{C}$ range. The solid lines are the fitted SRH lifetime curves for the dominant defect at each temperature.

Using the fitted SRH lifetime curves, the k -DPSS curves for the dominant defect were generated and are provided in Fig. 5.8 (a). The associated standard deviation of these curves is presented in Fig. 5.8 (b). One solution can be extracted at each bandgap half, shown in Fig. 5.8 (a) with black dots with the error range related to the fitting process described by the shaded grey area. The extracted energy levels for the bottom and upper bandgap halves are $-0.31 \pm 0.02\text{ eV}$ and $0.21 \pm 0.04\text{ eV}$, respectively. Furthermore, the extracted k values for the bottom and upper bandgap halves are 26 ± 2 and 25 ± 2 , respectively. For comparison, the k value and energy level combination of several previously investigated defects in silicon are also presented in the k -DPSS plot of Fig. 5.8 (a). The best known matches in the bottom bandgap half are the defect causing LeTID [96], the interstitial molybdenum donor $\text{Mo}_i^{0/+}$ [137], or the interstitial titanium double donor $\text{Ti}_i^{+/++}$ [138]. In the upper bandgap half, the only candidate is the defect associated with LeTID. However, none of the known solutions perfectly match the extracted parameters for the LID-related defect in Ga-doped silicon, suggesting that this may be a defect not characterized until now.

The reported k values in the literature for the LID-related defects in Ga-doped wafers, extracted using IDLS measurements are $27 < k < 35$ [85], and $k \approx 26$ [86], which are confirmed with these TIDLS results.

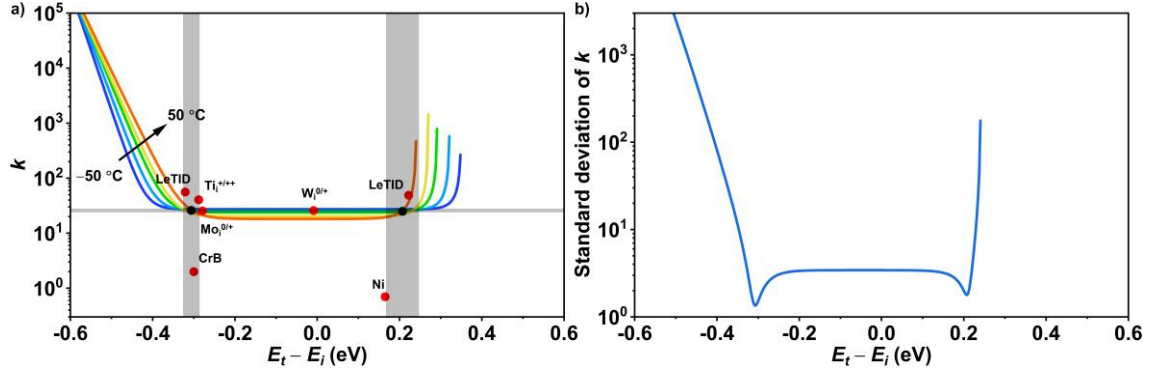


Fig. 5.8. (a) k -DPSS curves for the LID-related dominant defect in the Ga-doped wafer; and (b) the standard deviation of the k -DPSS curves at each energy level. The black dots in panel (a) are the calculated defect parameters. The shaded areas indicate the uncertainty range associated with the fitting process. Known candidate defects with parameters obtained from the literature are plotted as red dots in panel (a) [96, 137-140].

The k -DPSS curves as well as their standard deviation for the second defect are shown in Fig. 5.9 (a) and Fig. 5.9 (b), respectively. No clear intercept is observed between the k -DPSS curves, which results in not having a local minimum in the standard deviation curve. As a result, no defect parameter can be extracted based on these k -DPSS curves of the second defect.

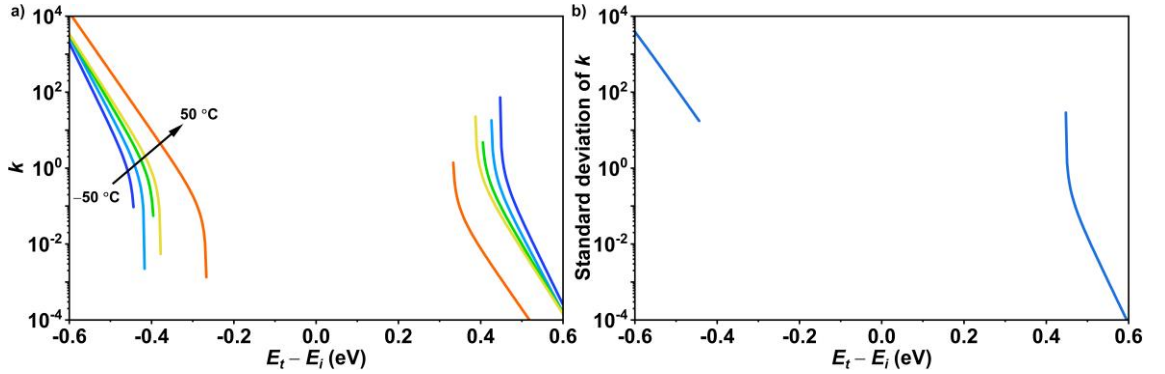


Fig. 5.9. (a) k -DPSS curves for LID-related second defect in a Ga-doped wafer; and (b) the standard deviation of the k -DPSS curves at each energy level.

5.2.3 Traps in Ga-doped Cz silicon

It was suggested in Chapter 3 that a set of traps are acting as the precursor of BO-related defects in B-doped Cz wafers. Moreover, in Chapter 4, it was shown that another set of traps with a large PCD time constant is present in B-doped mc-Si wafers and is impacted by light soaking. Considering these findings, PCD measurements were performed on Ga-doped Cz samples after light soaking and DA to investigate the trapping behavior of Ga-doped wafers.

PCD measurements were done at 30 °C on a representative sample (from previous sections) after DA and after LID. The passivation layers of this sample were removed and

replaced with a 10 nm ALD AlO_x capped with a 75 nm PECVD SiN_x . The sample was annealed at 400 °C for 30 min after AlO_x deposition (before SiN_x deposition) to activate the surface passivation. While passivation was crucial to observe the change in lifetime after the light soaking step, this passivation was chosen to remove the possible impact of DRM on the PCD measurements (see Section 3.3.1). The lifetime and PCD curves of this sample are shown in Fig. 5.10. As expected, the lifetime drops significantly with light soaking. The lower initial lifetime of the sample is presumably due to the lower quality of the surface passivation, compared with the PECVD SiN_x . A long decay tail is present in the PCD measurement shown in Fig. 5.10 (b), suggesting a trap exists in the bulk of the wafer. Since the TDDs are removed from this sample prior to the PCD measurement, this trap is unlikely to be due to TDDs. There seems to be a small change in the trap density after the degradation process. However, since the density of traps in this set of samples is very low, a correlation between degradation and change in trap density cannot be investigated with high certainty. It was mentioned previously that firing is required in order to observe LID in Ga-doped Cz wafers [85]. To separate the possible changes in trap density and LID-related defect density, a new set of samples was prepared with the same processing steps as the lifetime samples without firing, thus, without degradation upon light soaking.

This new set of unfired samples (denoted as the “PCD set”) was found to have a much higher trap density and was used for the following in-depth trap studies. This might be because the traps were not passivated during the firing process. The samples in the PCD set were prepared based on the processing steps described in Section 5.1 and note that the TDDs were annihilated for this set. The PCD curve of a representative sample from the PCD set is shown in Fig. 5.11. A long decay is present for both SiN_x -passivated and de-passivated samples indicating that traps are present in the bulk of these samples.

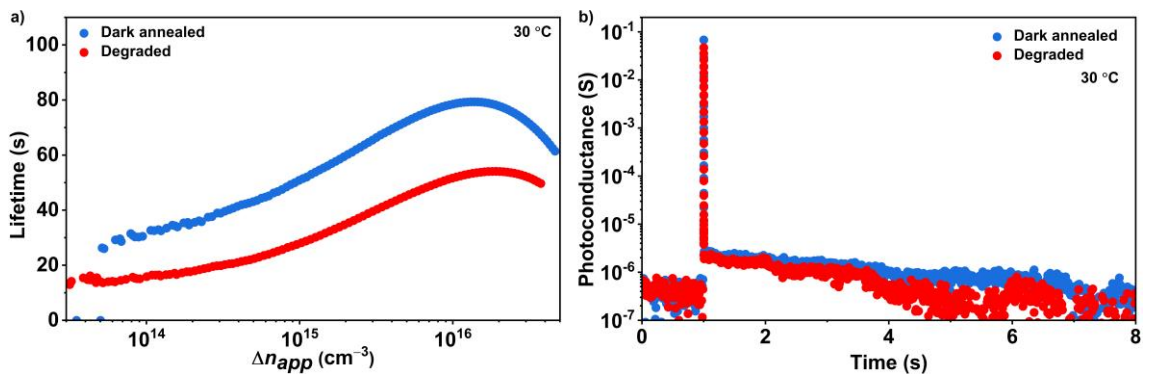


Fig. 5.10. (a) Lifetime; and (b) PCD curves of a Ga-doped sample measured at 30 °C before and after degradation.

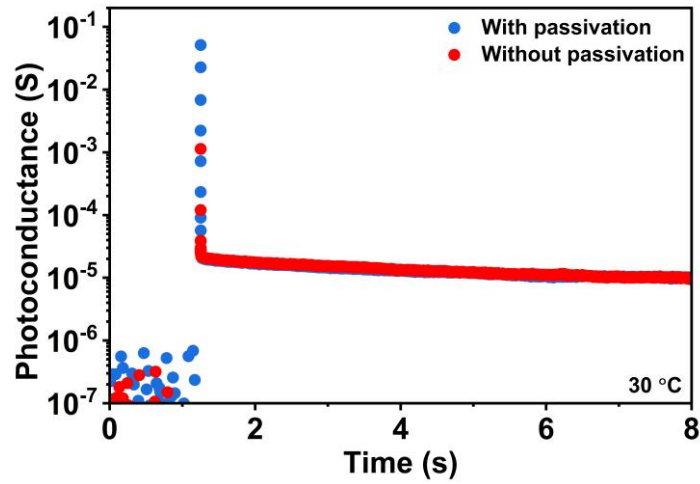


Fig. 5.11. PCD curves at 30 °C of a Ga-doped sample from the PCD set after DA, before and after removing surface passivation.

To investigate the evolution of traps with illumination and DA, PCD and lifetime measurements were performed on a representative passivated sample after DA at 175 °C for 10 min. Subsequent PCD and lifetime measurements were done after illuminating the sample at 75 °C for 3,000 min using halogen lamps with 0.4 suns intensity. This was followed by another DA-light soaking-DA process with PCD and lifetime measurements at the end of each step. The lifetime curves of the sample after these cycles are provided in Fig. 5.12 (a) and the PCD curves are shown in Fig. 5.12 (b). After light soaking, the lifetime of the sample does not decrease, but increases by $\sim 19\%$ at $\Delta n = 1 \times 10^{15} \text{ cm}^{-3}$. The increase in the effective lifetime is only present after the first light soaking and the lifetime remains almost unchanged in the following processing steps. Hence, the lifetime increase is not masking any LID effects in this sample. This increase in lifetime will be further investigated in the following paragraphs. The absence of degradation after light soaking is not surprising as it has been shown that a firing step is needed in order to observe degradation in Ga-doped wafers [85, 86], whereas the samples in the PCD set did not go through firing. With regards to the traps, it is observed that they are annihilated with light soaking and re-generated with DA. This behavior is like BO-related traps, observed in Chapter 3. However, in contrast with the B-doped Cz wafers, in these samples, the annihilation of the traps is accompanied by a lifetime increase in the first light soaking step and stabilization thereafter. Moreover, in the following DA and light soaking steps, the lifetime remains constant while in the B-doped samples, lifetime would cycle between dark annealed and degraded states.

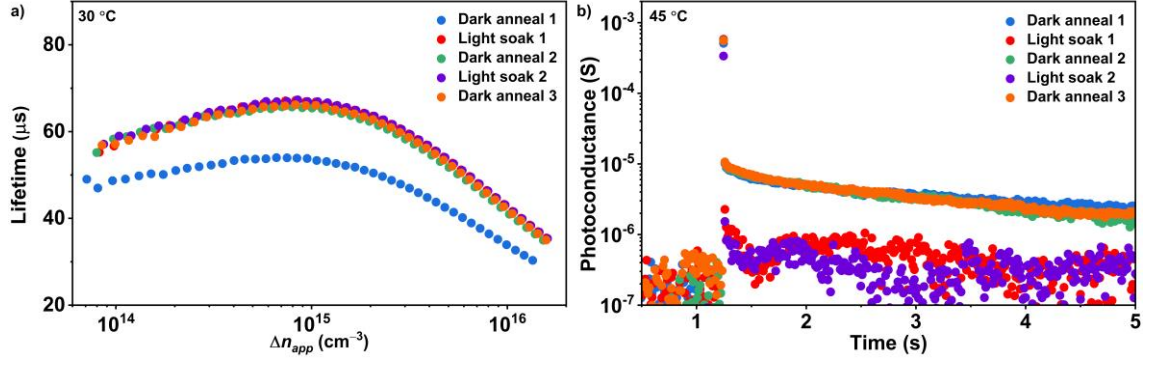


Fig. 5.12. Passivated Ga-doped sample from the PCD set cycled between DA and light soaking steps: (a) QSSPC lifetime curves at 30 °C; and (b) PCD curves at 45 °C.

To determine the source of the lifetime change after the first light soaking step and investigate the possible correlation between lifetime increase and trap annihilation, the saturation current density (J_0) of the sample after each processing step is extracted using the method developed by Kane and Swanson [141]. For this purpose, the $1/\tau_{\text{eff}}$ curve as a function Δn is generated and the slope of this curve is extracted in the high injection range. From this slope, the J_0 is calculated using:

$$J_0 = qWn_i^2 \left[\frac{d}{d(\Delta n)} \left(\frac{1}{\tau_{\text{corr}}} \right) \right] \quad (5.1)$$

where $1/\tau_{\text{corr}} = 1/\tau_{\text{eff}} - 1/\tau_{\text{intrinsic}}$ which includes the contributions from bulk SRH defects and surface recombination. For this calculation, it is assumed that the change in n_i with Δn is negligible. The J_0 values obtained after consecutive processing steps are shown in Fig. 5.13. J_0 decreases by ~20% after the first light soaking step and remains nearly constant in the following steps. It is possible that the observed improvement in the effective lifetime after the first light soaking step is due primarily to surface passivation improvement upon prolonged illumination [142]. Hence, it can be argued that the change in the lifetime is not related to the traps present in the bulk.

To validate the above tentative conclusion that changes in trap density and lifetime are not correlated, the trap annihilation rate was measured and compared with the rate of lifetime change during the first light soaking cycle. This comparison is done using NTD and NDD metrics. The effective lifetime curves of a representative sample after various light soaking durations are shown in Fig. 5.14 (a). The lifetime increases with light soaking for about one hour and remains almost unchanged afterward. On the other hand, the density of traps continues to decrease for up to 33 hours of light soaking in Fig. 5.14 (b). The measured NDD and NTD after each light soaking duration are presented in Fig.

5.14 (c). Fitting each curve with a mono-exponential function, the time constant of defect annihilation is determined to be 52.5 ± 10.8 min, while the time constant of trap annihilation is measured to be 611.8 ± 96.4 min. This order of magnitude difference in the annihilation rates further suggests that the traps in these Ga-doped Cz samples are unlikely to be related to the change in the lifetime.

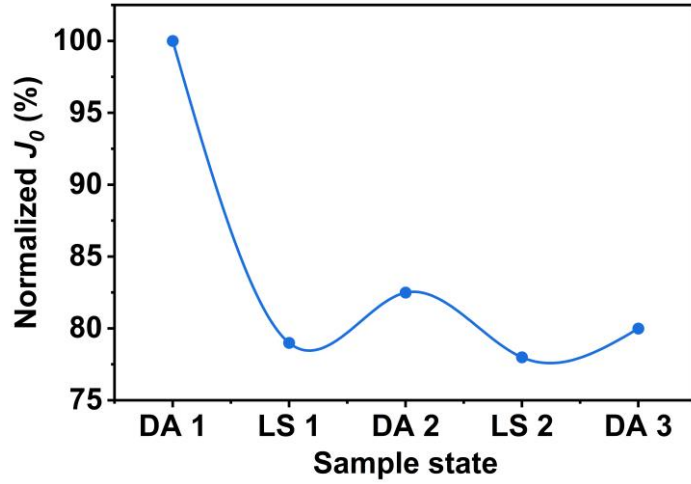


Fig. 5.13. Change in the normalized J_0 values of a Ga-doped sample from the PCD set during DA-light soaking cycles. The solid line is a guide to the eyes.

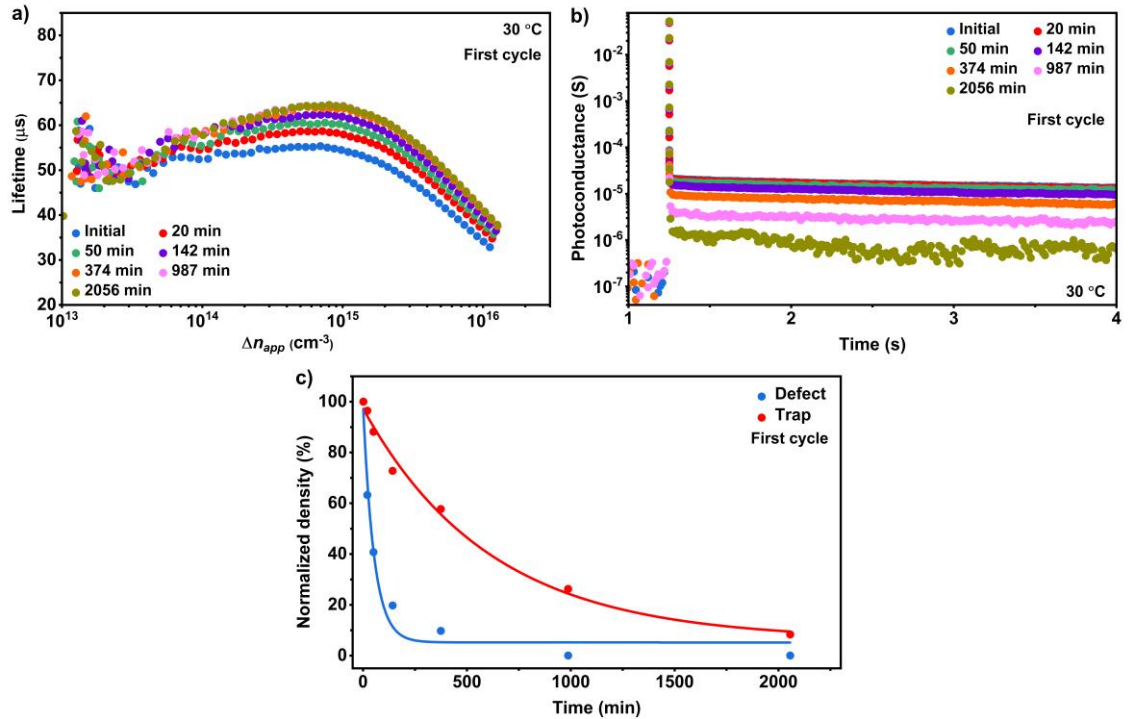


Fig. 5.14. (a) QSSPC lifetime curves; and (b) PCD curves of a Ga-doped sample from the PCD set measured at 30 °C after multiple light soaking durations. (c) Change in NDD and NTD during the light soaking process. Each data set is fitted with a mono-exponential function (solid lines).

Despite the difference in the defect and trap annihilation rates, it might be argued that a correlation between defects and traps might exist but with different rates. To investigate

this further, after the DA, a second cycle of light soaking was performed for the same time intervals and the change in the defect and trap densities were measured. While the lifetime remains almost unchanged throughout the second cycle in Fig. 5.15 (a), the long tail in the PCD curve shows the same decreasing behavior in Fig. 5.15 (b). Comparing the change in NDD in Fig. 5.15 (c) and NTD in Fig. 5.15 (d) between the first and the second cycles, it is clear that the rate of change in the NTD is the same in both cycles, while as expected, the NDD remains almost unchanged. Thus, it can be confirmed that the observed change in the trap density in Ga-doped samples is not correlated with lifetime improvement during light soaking.

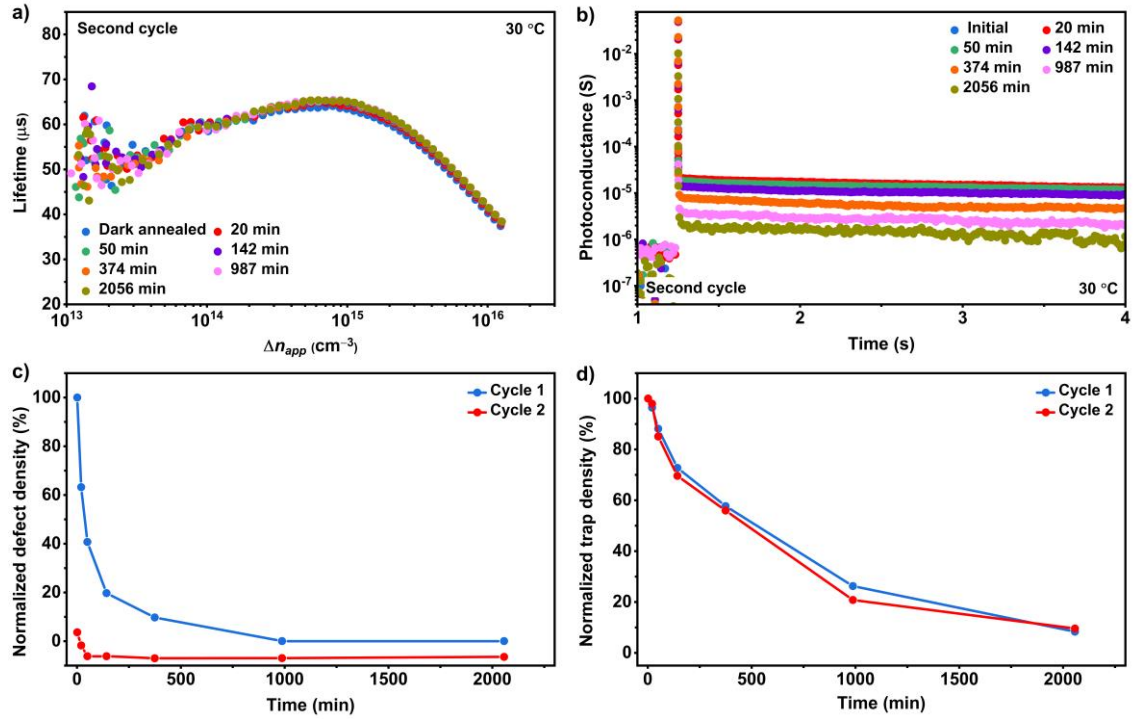


Fig. 5.15. (a) QSSPC lifetime curves; and (b) PCD curves of the Ga-doped sample from the PCD set measured at 30 °C in a second cycle of light soaking durations. Comparison of the change in (c) NDD; and (d) NTD as a function of light soaking duration for the first and second cycles.

Finally, temperature-dependent PCD measurements were conducted to extract the activation energy of the de-trapping process. Since the PCD signal drops significantly at very high temperatures, the PCD measurements were performed in a limited temperature range of 21 °C to 45 °C. The Arrhenius plot for the extracted PCD time constants is shown in Fig. 5.16. The extracted activation energy for this temperature range is 0.66 eV. By comparing this value with the E_a values of 1.13 eV and 0.2 eV extracted for the BO-related two-level traps in Chapter 3, it can be suggested that the nature of the observed trap in Ga-doped Cz samples is different from that of the BO-related traps.

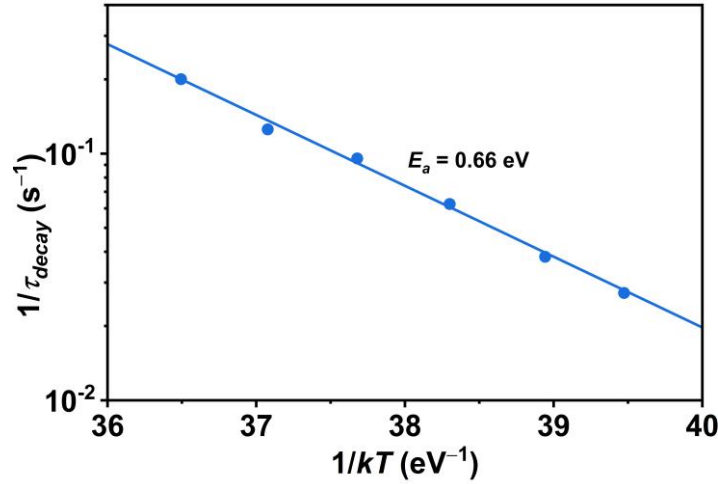


Fig. 5.16. Temperature-dependent PCD decay time constant for a Ga-doped sample from the PCD set. The solid line is a single-exponential function fit to the data.

5.3 Chapter summary

Due to the presence of BO-related degradation in B-doped Cz samples, a change in the doping element of *p*-type silicon wafers has been implemented by the major PV companies. The two proposed elements are Ga and In, with Ga being the dominant choice due to its higher segregation coefficient and lower dopant ionization activation energy. This chapter was dedicated to investigating the behavior of Ga- and In-doped Cz wafers under light soaking.

First, it was shown that Ga- and In-doped Cz wafers both demonstrate LID. Ga-doped wafers have a two-step degradation profile while In-doped wafers exhibit one-step degradation. By measuring the defect formation rate at several temperatures, the activation energies for the formation of LID-related defects were extracted. The defect annihilation with DA was also investigated. Both Ga- and In-doped samples exhibit two-step regeneration with DA, one fast and one slow. The activation energies for the annihilation of defects in the fast step are constant in the measured temperature range. For the slow step, only one defect annihilation activation energy was measured for Ga-doped samples (in the 200 °C to 170 °C range) while it seems that the annihilation rate becomes temperature-independent at temperatures below 170 °C. For the In-doped samples, two annihilation activation energies were extracted for two ranges of temperature.

In the next section, the parameters of the defect causing LID in Ga-doped samples were extracted. For this purpose, TIDLS measurement was performed and *k*-DPSS curves

were generated. It is shown that the two sets of parameters can be extracted for the dominant defect. On the other hand, for the second defect, no parameters can be determined from the DPSS analysis. When comparing the obtained parameters with several defects investigated in the literature, the best match is LeTID-related defects.

Finally, minority carrier traps in Ga-doped Cz wafers were studied. It was shown that traps are present in these samples. These traps are annihilated with light soaking and regenerated with DA. However, no connection between traps and LID-related defects was found. Moreover, the de-trapping activation energy of these traps is different from the BO-related traps investigated in Chapter 3.

As the share of Ga-doped Cz wafers in the PV market grows rapidly, it has become increasingly important to better identify the bulk defects in this alternative wafer material. This aim has been pursued in this chapter; first, by investigating the properties of recombination-active LID-related defects and, second by studying the traps in Ga-doped wafers. The findings regarding the degradation and annihilation steps and activation energies are important to theorize the degradation mechanism. The extracted defect parameters are a signature of the defect in Ga-doped wafers and were used to find possible candidates for this defect. Further investigation of bulk defects revealed the presence of a trap in Ga-doped wafers, although, no connection was found between traps and recombination-active defects.

Chapter 6

Bulk Defect Characterization in Metalized Solar Cells Using Temperature-Dependent Suns- V_{oc} Measurements¹

Extracting the parameters of efficiency-limiting bulk defects, E_t and k , in silicon solar cells is a critical step in identifying those defects and potentially eliminating their impact. As shown in Chapter 2, TIDLS measurement can be used to extract these parameters from wafers [96, 143-146]. Commonly, the QSSPC or transient PC methods are used to extract temperature- and injection-dependent lifetime curves [38, 147]. However, samples with a significant amount of metal on the surface (i.e., solar cells) cannot be measured using this method. One approach to overcome this barrier is to use wafers that closely match those used for the cells (“sister” wafers). However, sister wafers are not always available in production lines and the preparation of these wafers often requires significant effort. Another possible method for lifetime measurements on metalized cells is the front detection QSSPL measurement [148, 149]. However, this method needs a sophisticated calibration for each sample, thus, it is not suitable for mass production lines. Hence, there is a need to develop a fast method, that can be easily used in a production environment, to extract defect parameters directly from completed, metalized solar cells.

The illumination- V_{oc} measurement, also known as Suns- V_{oc} , has been long used as a method to obtain the solar cell pseudo-current-voltage (I - V) parameters without the impact of the series resistance [150]. The method is based on the measurement of open circuit voltage (V_{oc}) at different illumination intensities that are easily converted into current. Importantly, lifetime curves can also be extracted from Suns- V_{oc} measurements and unlike PC-based lifetime measurements, the obtained lifetime is not overestimated

¹ This chapter is partially based on:

S. Jafari, M. Abbott, D. Zhang, J. Wu, F. Jiang, and Z. Hameiri, “Bulk defect characterization in metalized solar cells using temperature-dependent Suns- V_{oc} measurements”, *Sol. Energy Mater. Sol. Cells*, vol. 236, pp. 111530, 2022.

by artifacts that impact the low injection levels (such as traps, [45] and DRM [99]). While Suns- $V_{oc}(T)$ measurements of silicon-based solar cells have been previously done [151-153], they have not been used to perform TIDLS-like defect characterization.

In this chapter, a novel method for the extraction of defect parameters from metalized solar cells is introduced. The method is based on Suns- $V_{oc}(T)$ measurements developed in this thesis. First, the newly developed Suns- $V_{oc}(T)$ method is presented in Section 6.1. In Section 6.2, the results are presented and discussed. First, the method is validated by comparing the parameters of the well-known BO-related defect [52, 143], extracted from solar cells and lifetime structures fabricated from B-doped Cz wafers. The method is then used to investigate the defect causing degradation in commercial Ga-doped passivated emitter and rear cells (PERC), its parameters are extracted and are compared with the extracted parameters in Chapter 5. Finally, a sensitivity analysis of the method is performed to investigate the effect of a limited temperature range on the certainty of extracted parameters. This analysis is further discussed to better understand different sources of error in TIDLS-based measurements.

6.1 Materials and methods

Sets of B-doped Cz wafers (B: $1.8 \pm 0.05 \text{ } \Omega \cdot \text{cm}$; $167 \pm 2 \text{ } \mu\text{m}$) and B- and Ga-doped Cz cells (B: $0.8 \pm 0.02 \text{ } \Omega \cdot \text{cm}$; $200 \pm 5 \text{ } \mu\text{m}$, Ga: $0.7 \pm 0.02 \text{ } \Omega \cdot \text{cm}$; $205 \pm 5 \text{ } \mu\text{m}$) were used in this chapter. The cells and wafers used in this chapter are not sisters. The wafers were gettered using a P-diffusion at $840 \text{ } ^\circ\text{C}$ for 45 min. The diffused layer was subsequently removed using an HF-HNO₃ solution with a volumetric ratio of 1:10. The wafers were then passivated with 75 nm PECVD SiN_x with a refractive index of 2.08 at 632 nm [92]. They were later fired at sample peak temperatures of $700 \text{ } ^\circ\text{C}$. The cells were commercially produced bifacial PERC devices (both B- and Ga-doped) passivated with a silicon oxide (SiO_x)-SiN_x stack on the front and an AlO_x-SiN_x rear stack deposited with an industrial PECVD tool.

The degradation was performed by light-soaking either at $130 \text{ } ^\circ\text{C}$ using halogen lamps with 0.4 suns equivalent photon flux illumination intensity (wafers) or at $130 \text{ } ^\circ\text{C}$ using a 960 nm laser with 40 suns intensity (cells). The extent of degradation at each stage was monitored using PL imaging. Prior to the degradation, the B-doped cells were dark annealed at $220 \text{ } ^\circ\text{C}$ for 20 min to destabilize the BO-related defect [52].

TIDLS measurements of the wafers were done using the custom made temperature-dependent lifetime system described in Chapter 3 [97]. The lifetime was monitored before and after the TIDLS (at 30 °C) to verify that no change was induced by the measurements. In this chapter, the reported lifetime is the average of ten consecutive measurements.

A modified Suns- V_{oc} system (see Fig. 6.1) was used to measure the cells. The system allows measurements in the temperature range of 30 °C to 200 °C. An X5DR flash head from Quantum Instruments was used as the excitation source. Suns- V_{oc} measurements at 30 °C were performed before and after the temperature-dependent measurements to verify that no changes are induced during the measurements. As pre-tests indicated that averaging has only a negligible impact on the quality of the measurement, no averaging was used for the Suns- V_{oc} measurements. It is known that τ_{eff} can be extracted from Suns- V_{oc} measurements. First, Δn is extracted (for a p -type cell) using [37]:

$$\Delta n(N_A + \Delta n) = n_i^2 \exp\left(\frac{V_{oc}q}{k_B T}\right) \quad (6.1)$$

Using the system's reference cell to determine the G , τ_{eff} can then be calculated:

$$\tau_{eff} = \frac{\Delta n}{G - \frac{d\Delta n}{dt}} = \frac{\Delta n}{\frac{J_{sc}S}{qw} - \frac{d\Delta n}{dt}} \quad (6.2)$$

where J_{sc} is the short circuit current density of the cell at 1 Sun illumination and S is the illumination intensity which is determined using the reference cell. To account for the change in G with temperature, J_{sc} should be known at each temperature. Here, J_{sc} was measured using a WaveLabs SINUS-220 I - V tester at eight temperatures in the 25 °C to 60 °C range. The temperature coefficient of J_{sc} was extracted from the linear fit to determine its value at any given temperature. The possible spectral mismatch between the flash lamp and WaveLabs excitation source is considered to be negligible for the current purpose.

As mentioned in Chapter 2, the SRH lifetime of the dominant defect can be determined by measuring the harmonic difference of the lifetime before and after degradation. It should be noted that this procedure is not always necessary when wafers are investigated, however, it is often crucial for cells as τ_{other} (and $\tau_{surface}$) in cells can be similar in magnitude to the investigated defect [19-21]. Thus, it is highly important to remove these effects by subtracting their contribution to the effective lifetime (here it is assumed that they are not modified by the degradation process).

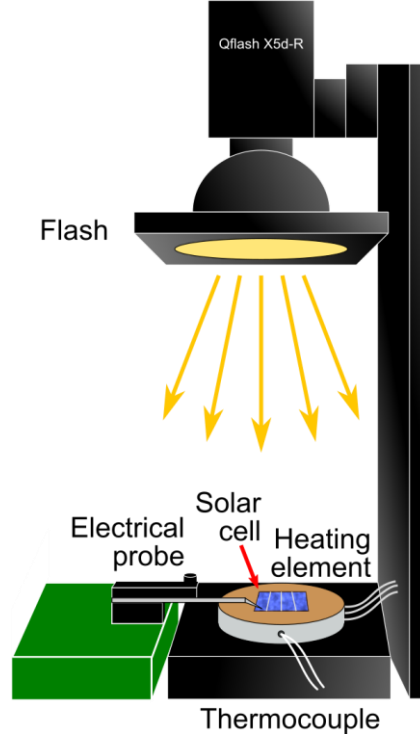


Fig. 6.1. Schematic of the modified system for temperature-dependent Suns- V_{oc} measurements.

6.2 Results and discussion

6.2.1 Investigation of BO-related defects in cells

In Fig. 6.2, the lifetime at 30 °C of a B-doped wafer (a) and cell (b) before and after degradation, as well as the τ_{LID} curves (using the method described in Section 2.2) are presented. As expected, the lifetime dropped after the light-soaking process, mainly at low injection levels [40]. At $\Delta n = 1 \times 10^{15} \text{ cm}^{-3}$, the cell and wafer lifetimes reduced by 19% and 65%, respectively. The difference in the degradation extent can be explained by the different initial lifetimes. The lower initial lifetime of the cells is probably due to recombination in the heavily diffused regions and poorer surface passivation. The difference in the extent of degradation can also be attributed to the different doping densities and different firing conditions as it is known that the firing process can suppress the generation of BO-related defects [154]. An important benefit of the proposed method is highlighted in Fig. 6.2. Note the obtained high-quality lifetime measurements down to $\Delta n = 1 \times 10^{13} \text{ cm}^{-3}$ via the Suns- V_{oc} measurement in Fig. 6.2 (b). In comparison, the PC-based measurements in Fig. 6.2 (a) seem to be impacted by artifacts (such as noise, trapping, or DRM effect) below $\Delta n = 2 \times 10^{14} \text{ cm}^{-3}$, limiting the range of data available for subsequent extraction of the defect parameters (marked with a square).

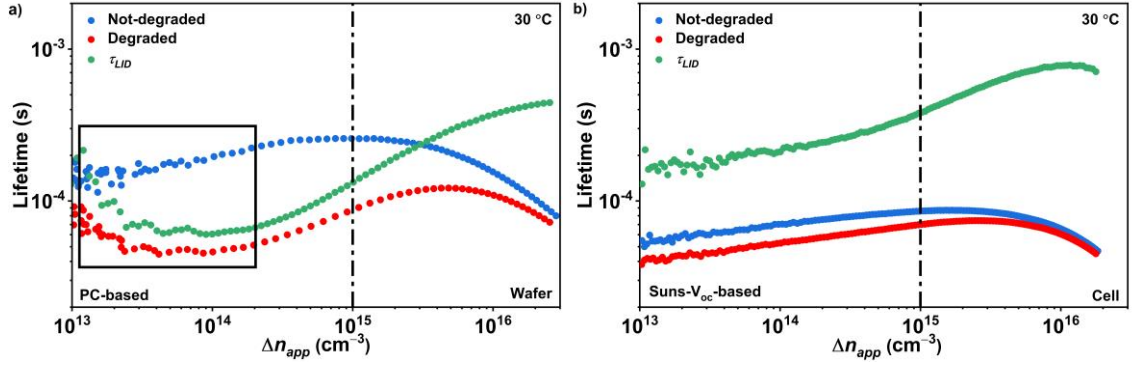


Fig. 6.2. Lifetime measurements at 30 °C of a B-doped (a) wafer measured with the PC-based method; and (b) cell measured with the Suns- V_{oc} method before (blue) and after (red) degradation, and the LID-related (green) lifetime curves.

In Fig. 6.3 (a), the k -DPSS curves [40] corresponding to the BO-related SRH lifetime in the range of -25 °C to 100 °C for a B-doped wafer are shown. The standard deviation of the fitted k across all the temperatures at each energy level is presented in Fig. 6.3 (c). The black dots at each bandgap half in Fig. 6.3 (a) are the $[E_t, k]$ combinations that provide the lowest normalized standard deviation of k . In Fig. 6.3 (b) and Fig. 6.3 (d), similar graphs for the B-doped cell measured in the range of 30 °C to 90 °C by the Suns- $V_{oc}(T)$ system are shown. Since the lifetime of the cell starts to recover at temperatures higher than 90 °C, the upper bound of the measurement is limited to this temperature. In both cases of the wafer and cell, the intersection point between the k -DPSS curves is not very sharp. This is assumed to be due to the temperature dependence of k resulting from the temperature dependence of the capture cross-sections. Therefore, the lower standard deviation associated with $[E_t, k]$ of the cell compared to the wafer can be explained by the smaller temperature range in the Suns- $V_{oc}(T)$ measurements. Another possible explanation for the diffused interceptions is the noise associated with the lifetime measurements.

The extracted defect parameters, $[E_t, k]$, for the wafer and cell are summarized in Table 6.1. As mentioned before, the reported uncertainties are due to the temperature dependence of k and possible measurement noise. Good agreement is obtained between the extracted E_t values for wafers and cells. Furthermore, the extracted E_t in the upper half is similar to the E_t reported in Ref. [143] and slightly higher than E_t determined by Ref. [41]. Regarding the extracted k values for the wafer and cell, a small difference in both bandgap halves can be observed. The difference between the extracted k values can be explained by the lower degradation extent in the case of the cell. The harmonic difference between the lifetime of the two states (not-degraded and degraded) is quite

small and therefore is prone to measurement uncertainty. Another possible reason for this difference is the smaller temperature range in the Suns- $V_{oc}(T)$ system. The uncertainty associated with this limited temperature range will be investigated in Section 6.2.3. It will be shown that the smaller temperature range is not the source of the observed difference in the extracted k values. Compared with the literature, the value extracted from the wafer is slightly lower than the k reported by Ref. [143] and in the range reported in Ref. [41]. For the cell, the extracted k value is higher than the values reported in both studies (18–25% higher) [41, 143]. Overall, the extracted value of k agrees with the literature within the expected uncertainty of the various methods. These results demonstrate the potential of the proposed method to extract the defect parameters *directly* from solar cells. Hence, it can be used in solar cell production lines without the need for sister wafers or special sample preparation.

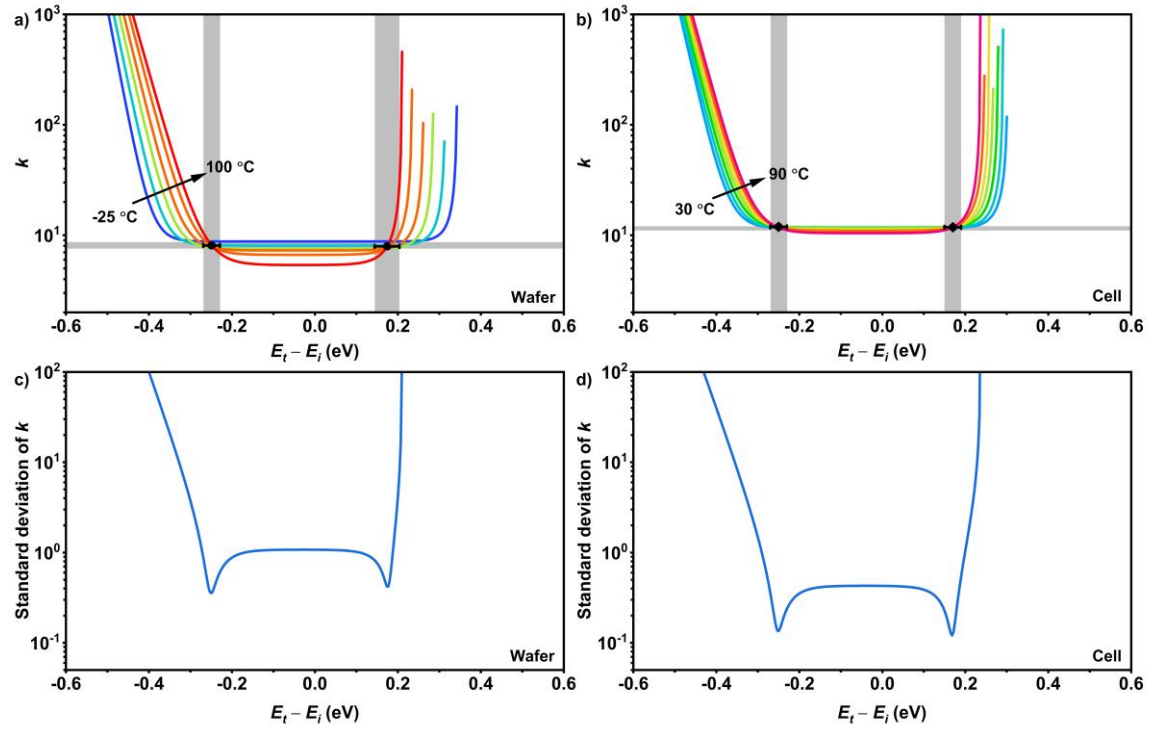


Fig. 6.3. Top row: (a) k -DPSS curves of k for BO-related defect in a wafer; and (b) cell. Bottom row: (c) standard deviation of the k -DPSS curves at each energy level for the wafer and (d) cell. The black dots are the calculated defect parameters. The shaded areas indicate the uncertainty range associated with the fitting process.

Table 6.1. The energy level and capture cross-section ratio for BO-related defect in a wafer, in a cell, and previously reported values.

Bandgap half	Parameter	Wafer	Cell	Ref. [143]	Ref. [41]
Bottom	$E_t - E_i$ (eV)	-0.25 ± 0.02	-0.25 ± 0.02	-	-0.22 to 0
	k	8.1 ± 0.4	11.9 ± 0.2	-	5 – 10
Upper	$E_t - E_i$ (eV)	0.17 ± 0.03	0.17 ± 0.02	0.15 ± 0.04	0 to 0.12
	k	7.9 ± 0.5	11.8 ± 0.2	9.5	5 – 10

6.2.2 Investigation of LID in Ga-doped cells

As discussed in Chapter 5, Ga has become the dominant doping element for *p*-type silicon wafers for PV applications [13]. To improve the stability of solar cells fabricated on Ga-doped substrates, it is important to investigate the defect causing LID in this material. In Fig. 6.4, the lifetime at 30 °C of a Ga-doped cell before and after LID, as well as τ_{LID} are shown. At $\Delta n = 1 \times 10^{15} \text{ cm}^{-3}$, the lifetime reduces by 8% (17% at $1 \times 10^{14} \text{ cm}^{-3}$) which is lower than the reported degradation extent for the wafer in Chapter 5 (60% at $1 \times 10^{15} \text{ cm}^{-3}$). The defect causing degradation in Ga-doped wafers and cells has not yet been studied extensively. This difference in degradation might be due to differences in doping densities, firing conditions, or the lower initial lifetime of the cell compared with the wafer.

In Fig. 6.5 (a) and Fig. 6.5 (b), the *k*-DPSS curves and the corresponding standard deviation curve as a function of energy level for a representative Ga-doped cell are presented, respectively. Table 6.2 summarizes the extracted $[E_t, k]$ values as well as the reported values in Chapter 5 for Ga-doped wafers and the reported defect parameters for LeTID-related defects [96]. The extracted energy levels from the wafer and the cell match well in the bottom bandgap half. However, in the upper bandgap half, the values have a larger difference. This is partially related to the difference in the measurement temperatures [40]. Since in both structures, the extracted energy level at the bottom bandgap half has a lower standard deviation, it can be suggested that this is the more likely solution. The extracted *k* values in both bandgap halves are slightly different ($\sim 30\%$) which might be due to the factors mentioned previously i.e., lower degradation extent in the case of the cell and different measurement temperature range. To separate the impact of different sources of error on the extracted parameters, the *k*-DPSS curves in the 25 °C to 100 °C (from the same set used in Section 5.2.2) and 30 °C to 105 °C (cell) temperature ranges are compared. The extracted $E_t - E_i$ values for the wafer are $-0.25 \pm 0.03 \text{ eV}$ and $0.13 \pm 0.04 \text{ eV}$ in the bottom and upper bandgap halves, respectively. Moreover, the extracted *k* values for the wafer in the bottom and upper halves are measured to be 23 ± 2 and 22 ± 2 , respectively. The results suggest that by changing the measurement temperature range of the wafer from -50 to 50 , to 25 °C to 100 °C, the difference in the extracted E_t of is slightly reduced, while the difference in *k* is slightly increased. These results suggest that the possible source of error for the investigated

defect is the temperature-dependence of k when extracting E_t and the extent of the degradation when extracting k .

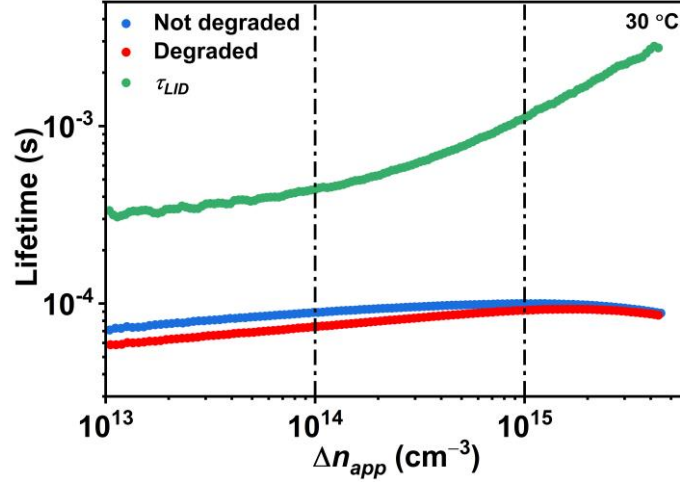


Fig. 6.4. Lifetime measurements at 30 °C of a Ga-doped cell measured with the Suns- V_{oc} method before (blue) and after (red) degradation, and the LID-related (green) lifetime curve.

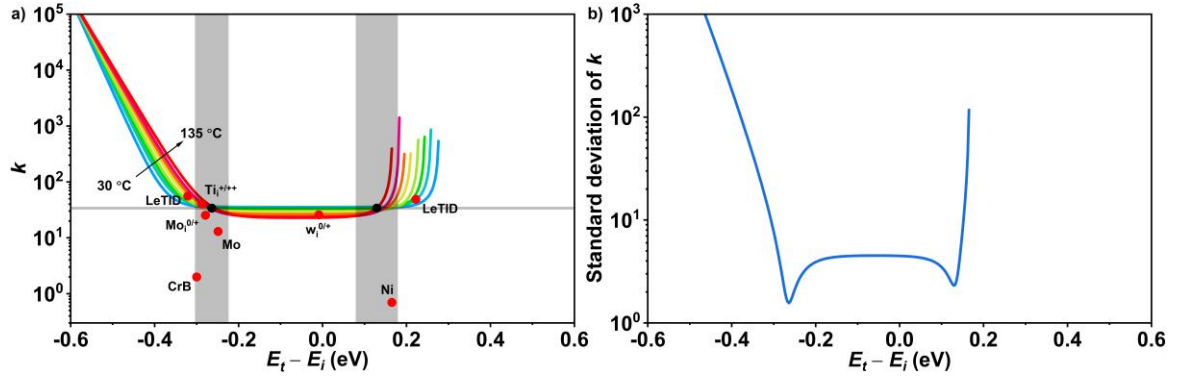


Fig. 6.5. (a) k -DPSS curves for LID-related defect in a Ga-doped cell; and (b) the standard deviation of the k -DPSS curves at each energy level. The black dots are the calculated defect parameters. The shaded areas indicate the uncertainty range associated with the fitting process. Candidate defects with parameters from the literature are plotted as red dots [96, 137-140].

Table 6.2. Energy levels and capture cross-section ratios for the LID-related defect as extracted from the Ga-doped wafer, cell, and values reported for LeTID-related defect parameters.

Bandgap half	Parameter	Wafer	Cell	LeTID [96]
Bottom	$E_t - E_i$ (eV)	-0.31 ± 0.02	-0.26 ± 0.04	-0.31 ± 0.05
	k	26 ± 2	34 ± 2	46 ± 16
Upper	$E_t - E_i$ (eV)	0.21 ± 0.04	0.13 ± 0.05	0.21 ± 0.05
	k	25 ± 2	33 ± 3	45 ± 15

The $[E_t, k]$ combination of defects with similar E_t or k values as for the Ga-doped cell is also shown in Fig. 6.5 (a). In the bottom bandgap half, the best matches are LeTID-related defects [96], $Ti_i^{+/++}$ [138], and $Mo_i^{0/+}$ [137]. In the upper bandgap half, the best match for the wafer is the LeTID-related defect (see Fig. 5.8) while no good match can be found for the cell. As mentioned in Chapter 5, two k values of $27 < k < 35$ [85], and

$k \approx 26$ [86] were recently reported for LID-related defects in Ga-doped Cz silicon, which agrees with these findings. However, as the researchers did not use TIDLS, the energy level has not been reported. Despite the good agreement between the extracted parameters in the bottom half with the parameters of the LeTID-related defect, it has indicated that the degradation of Ga-doped cells may not have the typical behavior of LeTID after DA and stabilization processes [84]. Hence, further investigation is required to determine if this defect is indeed similar to the LeTID-related defect.

The results from the characterization of defects in B-doped and Ga-doped cells suggest that the Suns- $V_{oc}(T)$ method is highly beneficial for the characterization of defects in cells without the need for the preparation of lifetime structures. This becomes more important as the quality of wafers improves and a slight difference in processing steps (between wafers and cells) might have an impact on the accuracy of extracted defect parameters. A limitation of the developed method in its current state is the limited measurement temperature range which will be discussed in detail in Section 6.2.3. Another possible limitation of the proposed method is that the internal voltage and terminal voltage are not always the same [155]. However, this effect is more dominant at higher injection while the change in the lifetime due to the bulk defects mainly happens in the low and medium injection ranges [23]. Another possible limitation of using the proposed method is shunted cells or high recombination at the metal and silicon interface [20, 156, 157]. The shunt resistance in modern industrial solar cells is often very high and the silicon-metal recombination has been significantly reduced. It is predicted to be reduced even further with the implementation of passivating contacts like tunnel oxide passivated carrier-selective contacts (TOPCon) and heterojunction solar cells [158, 159]. These improvements make the use of Suns- $V_{oc}(T)$ for defect analysis more attractive.

6.2.3 Sensitivity analysis

A limitation of the Suns- $V_{oc}(T)$ -based TIDLS technique used in this study, compared to lifetime-based TIDLS, is the limited temperature range of the tool and particularly the inability to perform measurements below 30 °C. This is not a fundamental limitation of the technique and can be removed by integrating a cooling stage into the system. The possibility of introducing a systematic error in the extracted parameters due to this limitation is discussed in this section. Besides the temperature range, the sensitivity

analysis is expanded to further discuss the validity of extracted parameters from lifetime- and Suns- V_{oc} -based TIDLS measurements.

The systematic error is investigated by modeling the injection-dependent lifetime curves with added artificial noise. SRH lifetime curves of a wafer with doping of $2.25 \times 10^{16} \text{ cm}^{-3}$ (similar to the Ga-doped cells) were generated for 11,500 $[E_t, k]$ combinations within the $E_t - E_i$ range of -0.57 eV to 0.57 eV and k range of 0.01 to 100. The defect density used for all the simulations is $1 \times 10^{13} \text{ cm}^{-3}$ with a fixed electron capture cross-section of $1 \times 10^{-16} \text{ cm}^2$. To reproduce the actual lifetime curves, random noise was added to the simulated curves. The noise used in this study is a random Gaussian noise which is anticorrelated with the injection level (as in typical lifetime measurements):

$$\tau_{with\ noise} = \tau_{without\ noise} (1 + \varepsilon \cdot \log \left(\frac{\Delta n_{max}}{\Delta n} \right)) \quad (6.3)$$

where ε is a random noise with normal distribution and Δn_{max} is the highest excess carrier density. As a result, the noise at the highest carrier density is zero and it increases with decreasing the injection level. The average added noise level at the lowest excess carrier concentration (at 0.01 of p_0) is 8%. This **average** noise is equal to the **highest** measured deviation (for all of the samples and temperatures) between the fitted SRH lifetime curve and the experimental lifetime data points (at 0.01 of p_0). Random noise is used, so the lifetime curve changes after each iteration. The graph on the left in Fig. 6.6 presents the SRH lifetime curves of a defect with $E_t = -0.45 \text{ eV}$ and $k = 30$ in the 0°C to 100°C temperature range (25°C intervals) while the graphs on the right are four consecutive simulations of the same lifetime curves with added noise. It is clear that the lifetime curve at each temperature changes after each iteration, since the generated noise in each iteration for each temperature is random. Since different lifetime curves lead to different error maps, each simulation was repeated 50 times and the averaged errors were used to generate the error maps. Further improving the maps requires a significant increase in averaging (hence, computation time), considering that the noise level has an anticorrelation with the square root of averages. As a result, 50 averages (~ 17 hours of computation for 8 temperatures using a typical desktop computer) were done to generate each of the $[E_t, k]$ combination maps.

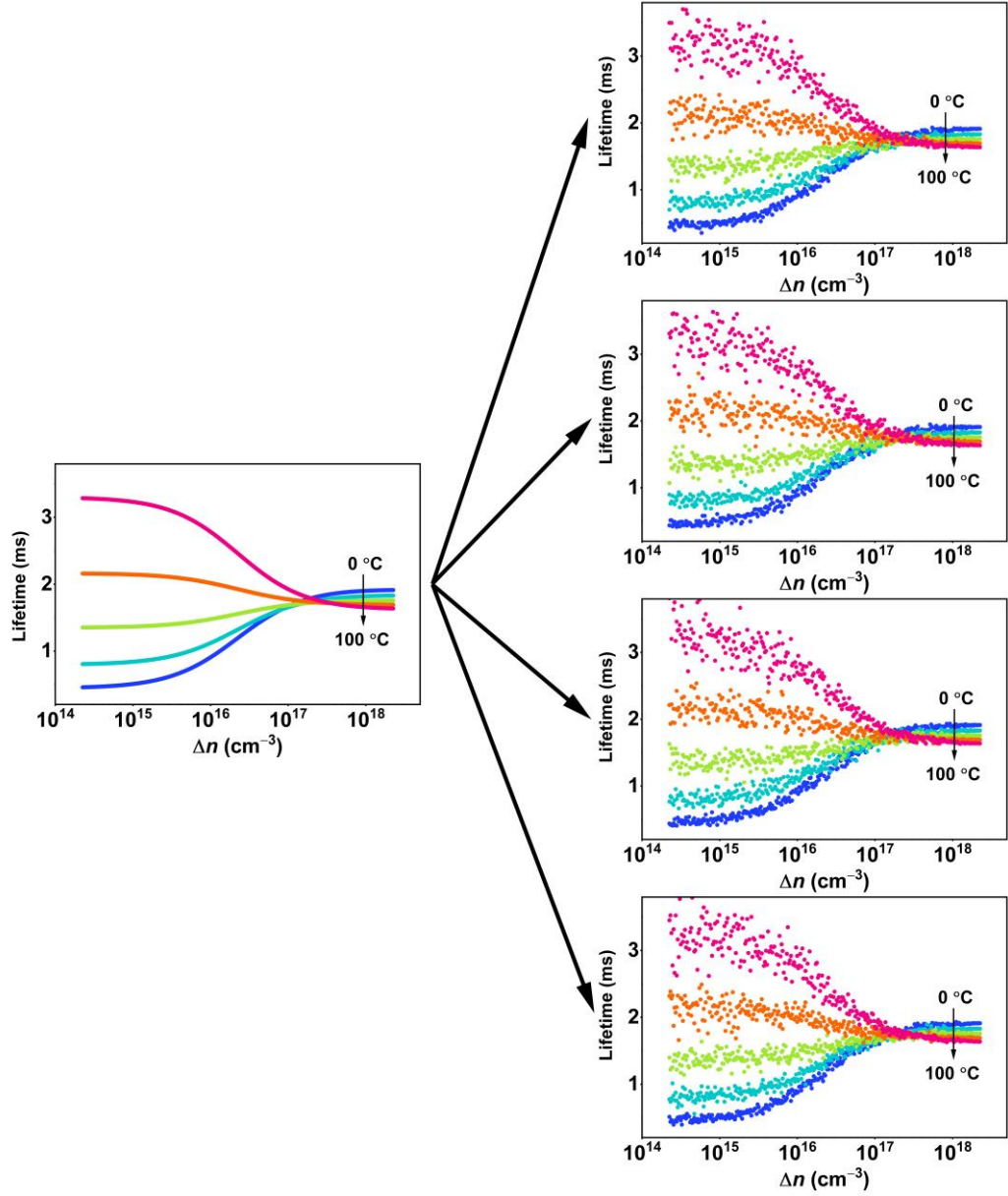


Fig. 6.6. Left: The SRH lifetime curves of a defect with $E_t - E_i = -0.45$ eV and $k = 30$ in the 0 °C to 100 °C temperature range. Right: The SRH lifetime curves for the same defect after adding random Gaussian noise.

Measurement temperature

Using the simulated lifetime curves, k -DPSS curves at different temperatures were created and the defect parameters were extracted in each bandgap half. The error associated with the extracted parameters was then determined from the comparison to the input values. As mentioned, this procedure was repeated 50 times for each $[E_t, k]$ combination and the averaged error is reported in the following figures. For E_t , the error is reported in eV (absolute error) while percentage is used to report the error for k (relative error). The simulation has been performed in three temperature ranges: (a) 30 °C to 90 °C (15 °C intervals) to consider the cases where bulk lifetime is overly sensitive to high-temperature measurements, similar to the Suns- $V_{oc}(T)$ measurements of the B-doped cell;

(b) 30 °C to 135 °C (15 °C intervals) as the typical temperature range of the Suns- $V_{oc}(T)$ system; and (c) -30 °C to 135 °C (15 °C intervals) to represent the temperature range of a lifetime-based TIDLS measurement. It should be noted that the reported error in this section is different from the reported uncertainty (Table 6.1 and Table 6.2). Since the real value is known, the calculated *error* is the difference between the real value and the extracted value. The *uncertainty*, on the other hand, is the confidence interval associated with the experimental data. It is due to both noise in measurements and temperature-dependence of k , while for the error, only the noise is considered. Note that without noise, the correct solution is determined across the entire simulated $[E_t, k]$ space (i.e., no error).

In Fig. 6.7, the error map of E_t (a–c) and k (d–f) for the simulated lifetime curves are presented. The $[E_t, k]$ for the BO-related defect extracted from the B-doped cell (in the upper bandgap half) is shown as a white circle while the $[E_t, k]$ of the LID-related defect extracted from the Ga-doped cell (in the bottom bandgap half) is shown as a red circle. The general trend of the error maps for both E_t and k are similar in all three cases. In general, near the mid-gap, the error of the extracted E_t is higher than in other areas. The high error associated with defect parameter extraction near mid-gap has been previously reported [160]. For k , the region near the mid-gap with k between ~ 0.1 and ~ 50 has a low error while outside this region, especially near the band edges, the error is relatively high.

Comparing Fig. 6.7 (a) and Fig. 6.7 (b), it seems that increasing the upper limit of the temperature from 90 °C to 135 °C reduces the error across the entire simulated range, especially for defects near the mid-gap. Extending the lower bound of the temperature further increases the accuracy of the extracted energy level, mainly near the band edges when comparing Fig. 6.7 (b) and Fig. 6.7 (c). The error maps of k show a similar trend: a wider temperature range lowers the error across the entire range. The high-accuracy region of k (dark areas in the figures) is further expanded when the measurements are extended to lower temperatures. It seems that the different temperature ranges do not introduce a systematic error when extracting $[E_t, k]$ values in most areas, meaning that the Suns- $V_{oc}(T)$ -based TIDLS method is not limited by the temperature range in the majority of the cases. The errors associated with the extracted E_t and k for both BO-related defect (white circles) and LID-related defect in Ga-doped cell (red circles) can be estimated from the figures. It seems that only a very small difference in errors is present

after changing the measurement temperature, of below 0.02 eV for E_t and $< 4\%$ for k (considering similar noise levels).

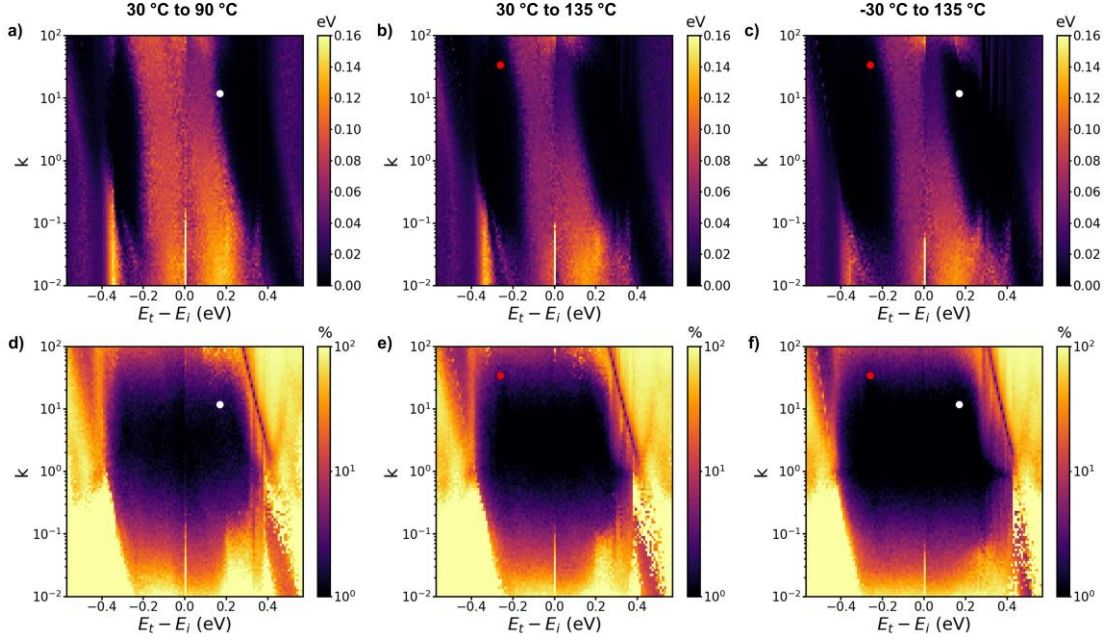


Fig. 6.7. (a–c) Absolute error in the extracted E_t ; and (d–f) relative error in the extracted k as a function of $E_t - E_i$ and k for the simulated lifetime measurements in the temperature ranges of: (a, d) 30 °C to 90 °C; (b, e) 30 °C to 135 °C; and (c, f) –30 °C to 135 °C. The white and red dots are the parameters of the BO-related defect and LID-related defect extracted from B- and Ga-doped cells, respectively.

Generation of similar error maps can be helpful to better assess the validity of any extracted parameters from TIDLS measurements (considering the expected defect parameters, doping level, measurement temperature range, noise level, etc). It should be noted that the error associated with temperature-dependent k is not considered in these simulations. However, this is a fundamental limit that also affects lifetime-based TIDLS measurements [40]. Moreover, this error can easily be added to the maps for the cases where the temperature dependency of k is known.

DPSS curve type

It is interesting to notice that k can be extracted with a high level of accuracy around mid-gap, despite the large error associated with E_t . On the other hand, near the band edges, the error in the determined k is relatively high. This difference in the error maps associated with E_t and k is mainly related to the two different types of DPSS curves, denoted as *continuous* and *split* [40]. In Fig. 6.8, the k -DPSS curves in the 0 °C to 100 °C temperature range (25 °C intervals) for three different defects are presented. The parameters of these defects are stated in the caption. In the case of only continuous k -DPSS curves, as shown in Fig. 6.8 (a), the intersection of the curves is not clear, making

the extraction of E_t challenging especially near the mid-gap region. However, as k is quite constant across a wide range of E_t , the error associated with the k value is quite small. In Fig. 6.8 (b), a set of split k -DPSS curves is presented. Unlike the previous case, k is significantly changing, even with a very small change of E_t , leading to a large error in the extracted k value while E_t can be determined relatively accurately. The impact of having both types of curves is shown in Fig. 6.8 (c). Having a mixture of continuous and split curves can have a positive impact to reduce the uncertainty associated with the extraction of the defect parameters from the TIDLS analysis.

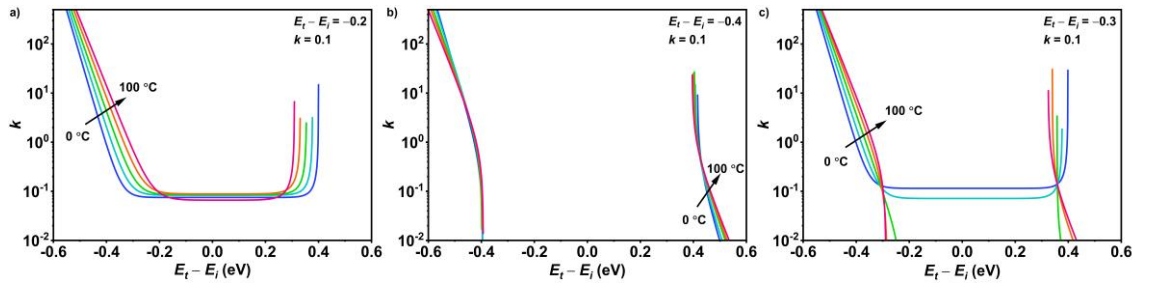


Fig. 6.8. k -DPSS curves generated from simulated SRH lifetime curves in the range of 0 °C to 100 °C with defect parameters of: (a) continuous curves with $E_t - E_i = -0.2$ eV and $k = 0.1$; (b) split curves with $E_t - E_i = -0.4$ eV and $k = 0.1$; and (c) combined continuous and split curves with $E_t - E_i = -0.3$ eV and $k = 0.1$.

Some of the sharp transitions from low error to high error regions observed in Fig. 6.7 error maps can be explained by the transition between the different types of DPSS curves. In Fig. 6.9 (a) and Fig. 6.9 (d), the error maps of E_t and k for the 30 °C to 135 °C temperature range (15 °C intervals) are presented, respectively [identical to Fig. 6.7 (b) and Fig. 6.7 (e)]. These maps are hatched in the areas with fully continuous DPSS curves (blue), fully split DPSS curves (red), and at least one DPSS curve from each type (green). Besides these maps, the error distribution in two energy level ranges denoted as mid-gap (-0.285 eV to 0.285 eV) and band edge (< -0.285 eV and > 0.285 eV) are also presented. The distribution of the absolute error in energy level for the mid-gap and band edge are shown in Fig. 6.9 (b) and Fig. 6.9 (c), respectively. Similarly, the relative error in k for these two regions is shown in Fig. 6.9 (e) and Fig. 6.9 (f), respectively. These histograms are fitted with a Kernel estimation of the probability density function, shown as solid lines.

Energy level: The error in the extracted E_t near the mid-gap is relatively high in Fig. 6.9 (a). This high error is shown as a peak in the error level of around 0.06 eV for the fully continuous curves in Fig. 6.9 (b). The error is reduced towards the band edges. In the mid-gap region, having a mixed type of DPSS curves results in relatively high error

levels due to this type of DPSS curves being limited to low k values which have high error levels in general. Moving towards the band edge region, the error increases [see Fig. 6.9 (a)], however, it is lower than the error in the mid-gap. This can be concluded from the error distribution for the fully split DPSS curves in Fig. 6.9 (c), which has a second peak around 0.03 eV and is almost without error levels higher than 0.05 eV.

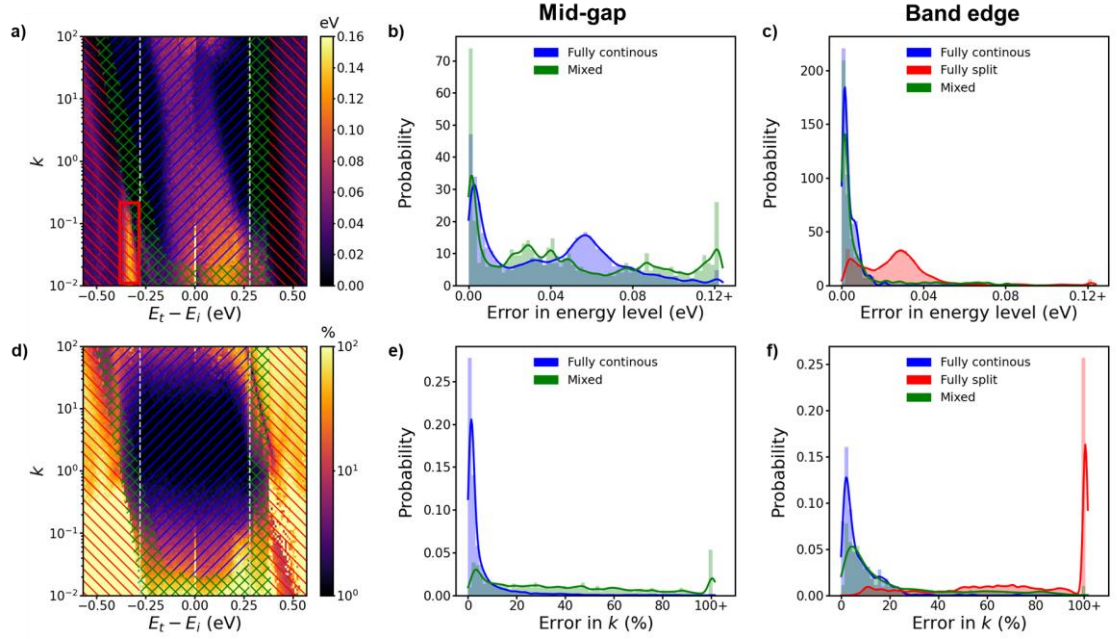


Fig. 6.9. (a) Map of the absolute error in the extracted E_i . The hatched areas are areas with fully continuous (blue), fully split (red), and the mixture of both (green) DPSS curves. (b) The distribution of the error in E_i in the mid-gap (-0.285 eV to 0.285 eV) and (c) band edge (< -0.285 eV and > 0.285 eV). (d) Map of the relative error in the extracted k . The hatched areas are areas with fully continuous (blue), fully split (red), and the mixture of both (green) DPSS curves. (e) The distribution of the error in the mid-gap (-0.285 eV to 0.285 eV) and (f) band edge (< -0.285 eV and > 0.285 eV). The solid lines in (b), (c), (e), and (f) are an estimation of the probability density function.

Capture cross-section ratio: The least error in the extracted k is near the mid-gap for k between ~ 1 and ~ 20 [Fig. 6.9 (d)]. As expected, the error level is very low when having fully continuous DPSS curves which mainly happens in the mid-gap region [Fig. 6.9 (e)]. Similar to energy level, having mixed types of DPSS curves is not beneficial in this range, since the mixed DPSS curves mainly happen at low k values with high error levels. Moving from mid-gap to the band edge region, it becomes clear why fully split curves are highly inaccurate for the extraction of k . A significantly high density of $> 100\%$ error levels for the extracted k is visible for the fully split curves [Fig. 6.9 (d)]. Comparing this error with the mixed error distribution, it can be suggested that having at least one continuous DPSS curve is beneficial to significantly reduce the error in the extracted k value. The results suggest that for accurate defect characterization, having a continuous DPSS curve is crucial while having a split curve might be beneficial in some cases. Thus, changing the measurement temperature or using a sample with a different doping density

might be needed for some measurements. For the defects investigated here (both in the mid-gap region), having fully continuous curves does not have a significant impact on the accuracy of the extracted E_t or k .

Besides the mentioned transitions, a high error area near the $E_t - E_i \approx -0.35$ eV and $k < 0.1$ is observed [marked with a red square in Fig. 6.9 (a)]. In Fig. 6.10 (a), the k -DPSS curves in the 30 °C to 135 °C (15 °C intervals) for a defect in this area are presented. The parameters of this defect are $E_t - E_i = -0.3$ eV and $k = 0.01$. The corresponding standard deviation curve of the k -DPSS curves is shown in Fig. 6.10 (b). The k -DPSS curves have two crossovers, one near the band edge (wrong solution in the bottom half) and one closer to the mid-gap (correct solution in the bottom half). As a result, two minima are observed in the bottom half of the standard deviation curve. The two minima have a very close standard deviation, shown in the inset of Fig. 6.10 (b), suggesting that in some iterations, the energy level near the band edge is considered as the solution. Thus, the average error corresponding to $[E_t, k]$ combinations in this region are higher than the neighboring areas.

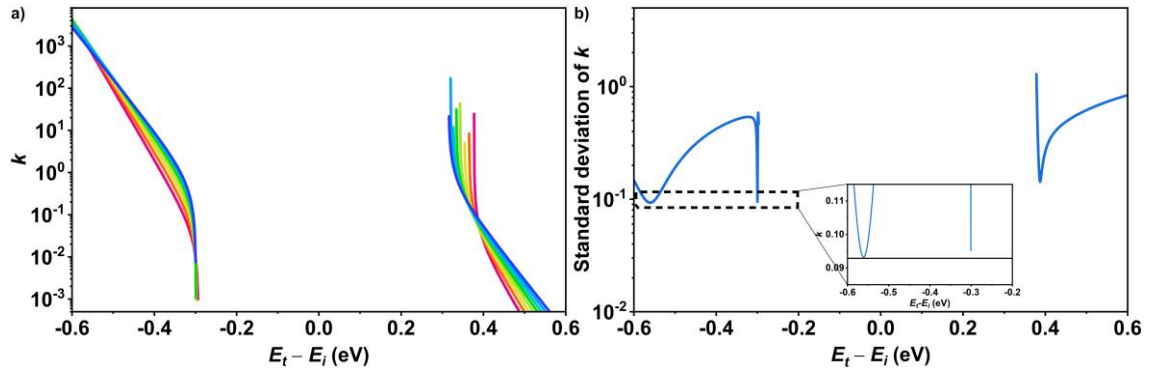


Fig. 6.10. (a) k -DPSS curves of a defect with $E_t - E_i = -0.3$ eV and $k = 0.01$ in the 30 °C to 135 °C temperature range; and (b) the standard deviation of the k -DPSS curves at each energy level.

Temperature uncertainty

Uncertainty in the measured temperature can also have an impact on the extracted parameters, as the calculated Δn is strongly correlated with the square of n_i [see Eq. (6.1)]. As n_i has a strong temperature dependency [106], a small error in the temperature measurement can lead to a significant error in n_i and thus, Δn . Therefore, the error is assessed in the temperature measurements by measuring the cell temperature five times at each temperature across the entire range of 30 °C to 135 °C (15 °C intervals) using two thermocouples (k-type thermocouples from OMEGA) attached to the sample. The cell was removed and put back on the stage after each measurement. In Fig. 6.11, the measured and the average sample temperatures as a function of the set temperature

reported by the software are presented. The measurement was done in the 30 °C to 135 °C temperature range (5 °C temperature intervals). It is shown that the temperature does not have a significant deviation even at the highest temperature with the highest deviation being 2.8 °C at 135 °C and the highest standard deviation being 1.5 °C at the same temperature. The average temperature deviation for all temperatures is 1.3 °C and the average standard deviation is 0.6 °C.

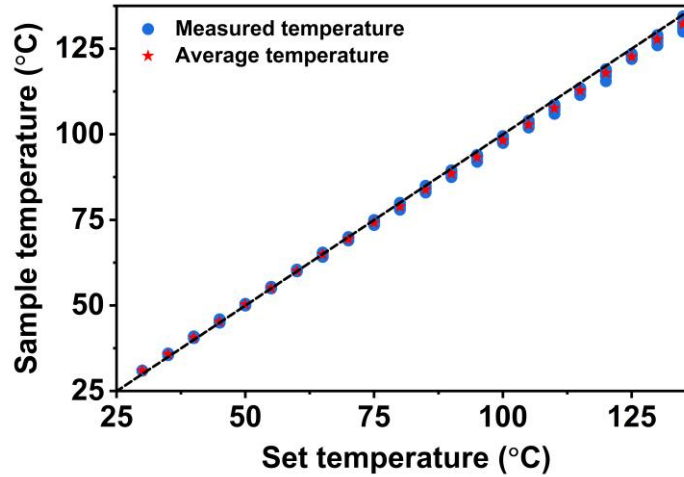


Fig. 6.11. The thermocouple-measured sample temperatures and their average, as a function of set temperatures. The dashed line is the $y = x$ function.

The standard deviation at each temperature was then considered as the error in the temperature and deviated temperature was generated by adding this value to the real temperature. Then, this deviated temperature was used to generate inaccurate n_i and in turn inaccurate Δn and lifetime curves for every set of defect parameters. The maximum deviation in n_i is 8% at 135 °C. In Fig. 6.12 the error maps of E_t [(a–b)] and k [(c–d)] for the simulated lifetime curves are presented. The error maps before and after considering the error in the measured temperature are almost identical, indicating only a minor impact of the small uncertainty associated with temperature.

Temperature intervals

To investigate the impact of more measurements (smaller temperature intervals) on the error maps, two sets of measurements with different temperature intervals within the same temperature range of 30 °C to 135 °C were simulated. The error maps for the 15 °C intervals (eight temperatures) are presented in Fig. 6.13 (a) and Fig. 6.13 (d) while Fig. 6.13 (b) and Fig. 6.13 (e) show the maps for the 5 °C intervals for (22 temperatures). The difference between the E_t and k error maps are presented in Fig. 6.13 (c) and Fig. 6.13 (f),

respectively. For E_t the difference is reported as the absolute difference between values while for k , the difference is reported in the form of percentage difference:

$$Difference = \frac{(ER_{k1} - ER_{k2})}{ER_{k1}} \cdot 100 \quad (6.4)$$

where ER_{k1} (ER_{k2}) is the error in the extracted k from the DPSS curves with 15 °C (5 °C) temperature intervals. In the difference maps, the positive areas (blue) mean that more measurements result in a lower error while the negative areas (red) are the opposite.

More measurements tend to result in a decrease in the error in the extracted E_t near the mid-gap, while it increases the error near the band edges [Fig. 6.13 (c)]. Between these two areas (especially at higher k values), an increase in the number of measurements does not have a significant impact on the extracted E_t .

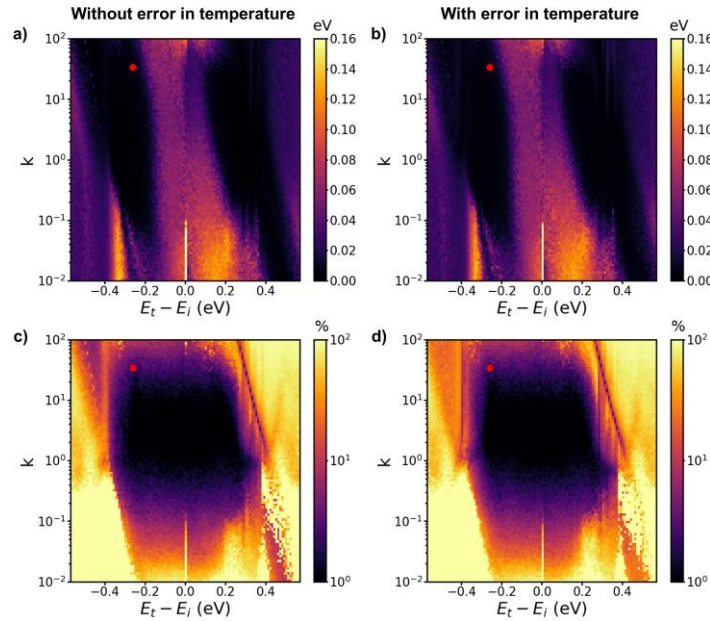


Fig. 6.12. Map of the (a, b) absolute error in the extracted E_t and (c, d) relative error in k as a function of E_t and k for the simulated lifetime measurements in the temperature range of 30 °C to 135 °C (a, c) without; and (b, d) with consideration of the error in temperature measurements.

For k , the same trend is observed. The results suggest that having more DPSS curves is beneficial near the mid-gap, while it increases the error near the band edges, especially at low k values [Fig. 6.13 (f)]. It should be noted that the presented maps are specific to this investigated case and may differ based on the factors mentioned before (doping level, measurement temperature range, noise level, etc). Thus, the optimum number of measurement temperatures might differ for each case.

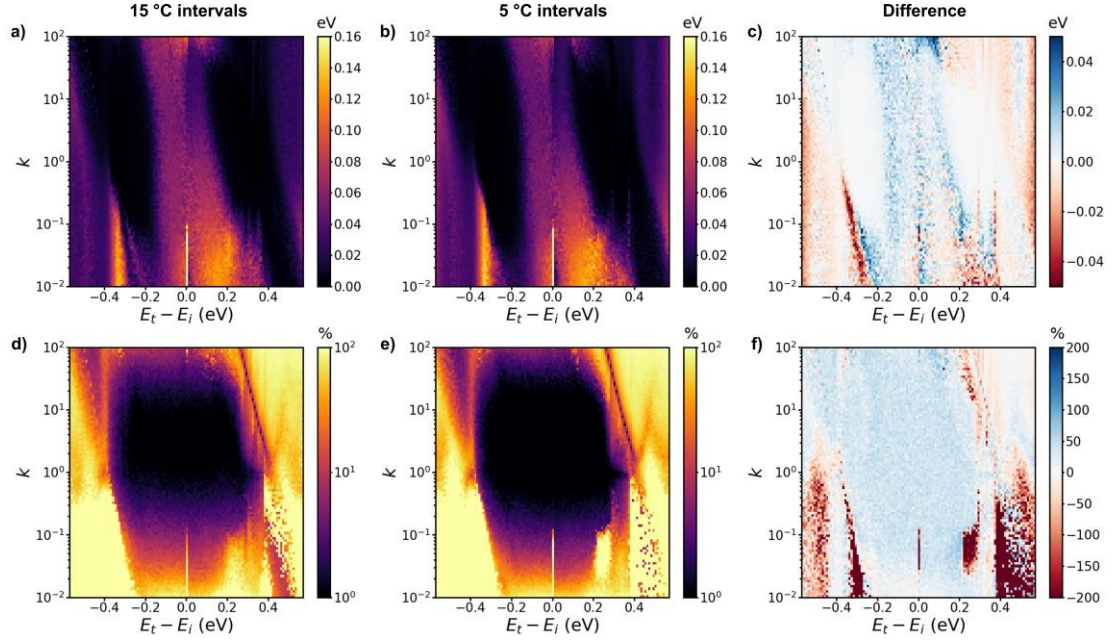


Fig. 6.13. (a, b) The absolute error in the extracted E_t ; and (c) the difference between the maps; and (d, e) the relative error in the extracted k ; and (f) the difference between the maps as a function of $E_t - E_i$ and k for the simulated lifetime measurements in the 30 °C to 135 °C temperature range. The temperature intervals of the lifetime curves are (a, d) 15 °C and (b, e) 5 °C.

6.3 Chapter summary

To better understand lifetime limiting defects in silicon cells, it is important to characterize these defects and extract the defect parameters. One method for defect characterization is to perform TIDLS measurements on silicon wafers. However, this method is not viable for the characterization of completed solar cells and, in many cases, only completed cells and not wafers are available for characterization. In this chapter, a method based on $Suns-V_{oc}(T)$ has been introduced to characterize defects within metalized cells.

First, the method was validated by comparing the parameters of the BO-related defect extracted from a B-doped cell using the proposed method and from wafers using a conventional lifetime-based TIDLS method. The extracted parameters were also compared with reported values from the literature. Based on the results, it can be suggested that this method has good accuracy for defect characterization within the typical error range for DPSS analysis.

Then, the proposed method was utilized to extract the parameters of the defect causing LID in the Ga-doped cells, and these parameters are compared with the parameters extracted from Ga-doped wafers in Chapter 5. It was shown that the results are slightly

different, which might be due to the different degradation extent in cells. Comparing the extracted parameters with the values reported in the literature, LeTID-related defect is the best match. However, it is also possible that the true defect has not been investigated previously in the literature.

Finally, a sensitivity analysis of the technique revealed that the limited temperature range of the system does not introduce a significant systematic error to the extracted parameters. Thus, it can be suggested that the uncertainty in the extracted parameters is mainly due to the factors which also affect lifetime-based TIDLS measurements.

This study demonstrates the potential of $\text{Suns-}V_{\text{oc}}(T)$ -based TIDLS measurement as a simple and accurate method for fast bulk defect characterization from metalized cells in production lines. Combining this method with appropriate error map simulations further improves the assessment of the extracted parameters.

Chapter 7

Summary and Outlook

7.1 Conclusions

To contextualize the importance of this thesis within the wider PV community: with the continual improvement of silicon solar cell efficiencies through advanced surface and contact passivation technologies, the quality of the bulk material becomes a key limitation. Silicon wafer bulk quality has been improving rapidly and, with this improvement, there comes a need to apply more sophisticated characterization methods.

The key aim of this thesis was to investigate bulk defects in *p*-type silicon wafers, both recombination-active defects and traps. This was pursued by extending the capabilities of established PC lifetime, PCD, and Suns- V_{oc} methods, and developing new methods for defect characterization.

In this thesis, two new methods are introduced to investigate the bulk. First, PCD measurements were utilized to study the precursor of a recombination-active defect directly. The direct assessment of precursors might have the benefit of higher sensitivity, as indirect measurements can be affected by other factors besides defect generation. Moreover, this method can be utilized to record other changes in the bulk, which do not impact the lifetime but can be helpful to describe other observed phenomena. For the second method, the parameters of recombination-active defects are extracted directly from metalized solar cells using temperature-dependent Suns- V_{oc} measurements. With the significant decrease in the density of bulk defects, a small difference between lifetime and cell structures can lead to inaccurate defect characterization. Thus, the extraction of defect parameters *directly* from metalized cells is of significant value. The key findings of each chapter are presented below.

In Chapter 3, PCD measurements were utilized to investigate the precursor of BO-related defects. It was shown that a trap is acting as the precursor of this defect and the trap density is reduced as the defect density increases. It was found that this trap has more

than one energy level. The findings in this chapter demonstrate the unique potential of PCD measurements to study defects in their **non-active** form. It also presents the importance of trap studies for a better understanding of the electrical properties of silicon wafers. These results confirm the previous findings with DLTS measurements, suggesting the presence of a set of deep donor traps which act as the precursor of the BO-related defects; transforming to recombination active shallow acceptor defects through illumination.

In Chapter 4, the developed PCD measurement method was used to investigate traps in B-doped mc-Si wafers. It was shown that a set of slow traps with a large decay time constant are present in these samples. Further investigation of these traps showed that they are temporarily removed with the firing process, while they are generated again after DA or by keeping the samples at room temperature. Laser annealing of the samples permanently removed the traps, however, no connection between the removal of traps and generation of LeTID-related defects was observed. It was also shown that Fe or Ni impurities are not the possible sources of this trap. By investigating a set of contrasting mono-cast silicon wafers, it was concluded that the source of these traps is not dislocations, but the grain boundaries.

In Chapter 5, LID in Ga- and In-doped Cz wafers was studied. First, the kinetics of this degradation in both materials were investigated. Both the defect formation and annihilation activation energies were measured. The focus then shifted toward Ga-doped wafers as it is the more promising substitute for B-doped wafers. For the first time, the defect parameters for the LID-related defect in Ga-doped wafers were extracted. In the final section of this chapter, traps in Ga-doped wafers were studied using the PCD method developed in Chapter 3. It was shown that this trap is annihilated with light soaking and re-generated with DA. However, in contrast to the B-doped Cz wafers, it is likely that this Ga-doped Cz wafer trap is not related to the LID-related defect.

In Chapter 6, a method for the direct characterization of recombination-active defects in *completed and fully metalized cells* was developed. The method is based on Suns- $V_{oc}(T)$ measurements and DPSS analysis to extract the defect parameters. The method was verified using B-doped cells; the parameters of BO-related defects were extracted from the cells and compared with: (i) the values extracted from lifetime structure; as well as (ii) values reported in the literature. This novel Suns- $V_{oc}(T)$ method was subsequently

applied to extract the parameters of LID-related defects in Ga-doped cells. These parameters were compared with the values measured in Chapter 5, with the extracted energy level in the bottom bandgap half being similar within the error range and k being slightly different. In the last section of this chapter, a sensitivity analysis method was conducted to evaluate the impact of the limited temperature range of the Suns- $V_{oc}(T)$ measurement. It was shown that for the defects investigated in this chapter, the limited temperature range is not introducing a systematic error.

7.2 Future work

The items below summarize potential directions for which the work done in this thesis can continue:

1. To confirm the observations regarding the chemical composition of the complex causing BO-related degradation, PCD measurements of samples with varying B and O concentrations can be done. This will be a direct assessment of defect precursor density to study the composition of the defect.
2. The observed BO-related trap has more than one energy level. There are no existing methods for the extraction of the parameters of traps with multiple energy levels using PCD measurements. A method to extract the parameters of the multi-level BO-related traps can be developed.
3. The knowledge gained in this thesis can be used to investigate traps in non-silicon materials. Due to the typically shorter time constant of traps in other materials, the system might need larger data acquisition rates to record changes in PCD with higher resolution.
4. It was shown previously, and also in this thesis, that various Ga-doped Cz wafers demonstrate different LID behavior. Further investigation can be done to unravel the reasons behind this difference. Moreover, the characterization of LID-related defects in Ga-doped Cz wafers can be done with other methods (such as DLTS) to confirm the extracted parameters from TIDLS measurements.
5. A systematic study regarding the impact of temperature range, signal noise level, temperature dependence of k , doping level, etc. on the accuracy of the extracted defect parameters from TIDLS measurements can be done using the sensitivity analysis method developed in Chapter 6.

References

- [1] M. Lynas, B. Z. Houlton, and S. Perry, "Greater than 99% consensus on human caused climate change in the peer-reviewed scientific literature," *Environ. Res. Lett.*, vol. 16, no. 11, p. 114005, 2021.
- [2] "AAAS reaffirms statements on climate change and integrity." [Online]. Available: <https://www.aaas.org>.
- [3] J. W. Zillman, "The IPCC third assessment report on the scientific basis of climate change," *Australas. J. Environ. Manag.*, vol. 8, no. 3, pp. 169-185, 2001.
- [4] J. Houghton, Y. Ding, D. Griggs, M. Noguer, P. Van der Linden, and D. Xiaosu, "IPCC third assessment report: Climate change 2001: The scientific basis," *IPCC*, 2001.
- [5] "What's in a name? Global warming vs. climate change." [Online]. Available: <https://www.nasa.gov>.
- [6] "Global greenhouse gas emissions data." [Online]. Available: <https://www.epa.gov>.
- [7] "Sector by sector: Where do global greenhouse gas emissions come from?" [Online]. Available: <https://ourworldindata.org>.
- [8] *Kyoto protocol*. 1997.
- [9] *Paris agreement*. 2015.
- [10] I. E. Agency, "Net zero by 2050: A roadmap for the global energy sector," 2021.
- [11] R. Perez and M. Perez, "A fundamental look at energy reserves for the planet," *The IEA SHC Solar Update*, vol. 50, no. 2, 2009.
- [12] IEA, "Renewables 2020: Analysis and forecast to 2025," 2020.
- [13] "International technology roadmap for photovoltaic (ITRPV)," 2022.
- [14] "Renewable power generation costs in 2020." [Online]. Available: <https://www.irena.org>.
- [15] PVPS, "Trends in photovoltaic applications," 2020.
- [16] NREL, "Best research-cell efficiency chart," 2021.

- [17] M. Green, E. Dunlop, J. Hohl-Ebinger, M. Yoshita, N. Kopidakis, and X. Hao, "Solar cell efficiency tables (version 57)," *Prog. Photovolt.: Res. Appl.*, vol. 29, no. 1, pp. 3-15, 2021.
- [18] P. Würfel and U. Würfel, *Physics of solar cells: From basic principles to advanced concepts*. John Wiley & Sons, 2016.
- [19] A. Cuevas, "The effect of emitter recombination on the effective lifetime of silicon wafers," *Sol. Energy Mater. Sol. Cells*, vol. 57, no. 3, pp. 277-290, 1999.
- [20] J. Muller, K. Bothe, S. Gatz, H. Plagwitz, G. Schubert, and R. Brendel, "Contact formation and recombination at screen-printed local aluminum-alloyed silicon solar cell base contacts," *IEEE Trans. Electron Devices*, vol. 58, no. 10, pp. 3239-3245, 2011.
- [21] Y. Tomizawa *et al.*, "Analysis of contact recombination at rear local back surface field via boron laser doping and screen-printed aluminum metallization on p-type PERC solar cells," *Energy Procedia*, vol. 124, pp. 384-391, 2017.
- [22] Y. Varshni, "Band-to-band radiative recombination in groups IV, VI, and III-V semiconductors (I)," *Phys. status solidi (b)*, vol. 19, no. 2, pp. 459-514, 1967.
- [23] W. Shockley and W. Read Jr, "Statistics of the recombinations of holes and electrons," *Phys. Rev.*, vol. 87, no. 5, p. 835, 1952.
- [24] R. N. Hall, "Electron-hole recombination in germanium," *Phys. Rev.*, vol. 87, no. 2, p. 387, 1952.
- [25] M. A. Green, *Solar cells: Operating principles, technology, and system applications*. Englewood Cliffs, 1982.
- [26] T. Trupke *et al.*, "Temperature dependence of the radiative recombination coefficient of intrinsic crystalline silicon," *J. Appl. Phys.*, vol. 94, no. 8, pp. 4930-4937, 2003.
- [27] H. Schlangenotto, H. Maeder, and W. Gerlach, "Temperature dependence of the radiative recombination coefficient in silicon," *Phys. status solidi (a)*, vol. 21, no. 1, pp. 357-367, 1974.
- [28] P. Altermatt, F. Geelhaar, T. Trupke, X. Dai, A. Neisser, and E. Daub, "Injection dependence of spontaneous radiative recombination in crystalline silicon: Experimental verification and theoretical analysis," *Appl. Phys. Lett.*, vol. 88, no. 26, p. 261901, 2006.
- [29] S. M. Sze, Y. Li, and K. K. Ng, *Physics of semiconductor devices*. John Wiley & Sons, 2021.
- [30] L. Hultdt, "Band-to-band Auger recombination in indirect gap semiconductors," *Phys. status solidi (a)*, vol. 8, no. 1, pp. 173-187, 1971.
- [31] J. Dziewior and W. Schmid, "Auger coefficients for highly doped and highly excited silicon," *Appl. Phys. Lett.*, vol. 31, no. 5, pp. 346-348, 1977.

- [32] A. Hangleiter and R. Häcker, “Enhancement of band-to-band Auger recombination by electron-hole correlations,” *Phys. Rev. Lett.*, vol. 65, no. 2, p. 215, 1990.
- [33] P. P. Altermatt, J. Schmidt, G. Heiser, and A. G. Aberle, “Assessment and parameterisation of Coulomb-enhanced Auger recombination coefficients in lowly injected crystalline silicon,” *J. Appl. Phys.*, vol. 82, no. 10, pp. 4938-4944, 1997.
- [34] D. T. Stevenson and R. J. Keyes, “Measurement of carrier lifetimes in germanium and silicon,” *J. Appl. Phys.*, vol. 26, no. 2, pp. 190-195, 1955.
- [35] R. A. Bardos, T. Trupke, M. C. Schubert, and T. Roth, “Trapping artifacts in quasi-steady-state photoluminescence and photoconductance lifetime measurements on silicon wafers,” *Appl. Phys. Lett.*, vol. 88, no. 5, p. 053504, 2006.
- [36] T. Trupke and R. Bardos, “Photoluminescence: A surprisingly sensitive lifetime technique,” in *31st IEEE Photovoltaic Specialists Conference (PVSC)*, 2005.
- [37] R. A. Sinton and A. Cuevas, “Contactless determination of current–voltage characteristics and minority-carrier lifetimes in semiconductors from quasi-steady-state photoconductance data,” *Appl. Phys. Lett.*, vol. 69, no. 17, pp. 2510-2512, 1996.
- [38] D. K. Schroder, *Semiconductor material and device characterization*. John Wiley & Sons, 2015.
- [39] J. Schmidt, “Temperature-and injection-dependent lifetime spectroscopy for the characterization of defect centers in semiconductors,” *Appl. Phys. Lett.*, vol. 82, no. 13, pp. 2178-2180, 2003.
- [40] S. Rein, *Lifetime spectroscopy: A method of defect characterization in silicon for photovoltaic applications*. Springer Science & Business Media, 2006.
- [41] J. Schmidt and A. Cuevas, “Electronic properties of light-induced recombination centers in boron-doped Czochralski silicon,” *J. Appl. Phys.*, vol. 86, no. 6, pp. 3175-3180, 1999.
- [42] J. D. Murphy, K. Bothe, R. Krain, V. Voronkov, and R. Falster, “Parameterisation of injection-dependent lifetime measurements in semiconductors in terms of Shockley-Read-Hall statistics: An application to oxide precipitates in silicon,” *J. Appl. Phys.*, vol. 111, no. 11, p. 113709, 2012.
- [43] J. A. Hornbeck and J. R. Haynes, “Trapping of minority carriers in silicon. I. p-type silicon,” *Phys. Rev.*, vol. 97, no. 2, p. 311, 1955.
- [44] Y. Zhu, M. K. Juhl, G. Coletti, and Z. Hameiri, “Reassessments of minority carrier traps in silicon with photoconductance decay measurements,” *IEEE J. Photovoltaics*, vol. 9, no. 3, pp. 652-659, 2019.

- [45] D. Macdonald and A. Cuevas, "Trapping of minority carriers in multicrystalline silicon," *Appl. Phys. Lett.*, vol. 74, no. 12, pp. 1710-1712, 1999.
- [46] J. Haynes and J. Hornbeck, "Trapping of minority carriers in silicon. II. n-type silicon," *Phys. Rev.*, vol. 100, no. 2, p. 606, 1955.
- [47] Y. Hu, H. Schøn, Ø. Nielsen, E. Johannes Øvrelid, and L. Arnberg, "Investigating minority carrier trapping in n-type Cz silicon by transient photoconductance measurements," *J. Appl. Phys.*, vol. 111, no. 5, p. 053101, 2012.
- [48] H. P. Fischer, W., "Investigation of photon and thermal induced changes in silicon solar cells," in *10th IEEE Photovoltaic Specialists Conference (PVSC)*, 1973.
- [49] S. Glunz, S. Rein, W. Warta, J. Knobloch, and W. Wettling, "On the degradation of Cz-silicon solar cells," in *2nd World Conference on Photovoltaic Energy Conversion (WCPEC)*, 1998.
- [50] S. Rein, S. Diez, R. Falster, and S. Glunz, "Quantitative correlation of the metastable defect in Cz-silicon with different impurities," in *3rd World Conference on Photovoltaic Energy Conversion (WCPEC)*, 2003.
- [51] J. Schmidt and K. Bothe, "Structure and transformation of the metastable boron- and oxygen-related defect center in crystalline silicon," *Phys. Rev. B*, vol. 69, no. 2, p. 024107, 2004.
- [52] T. Niewelt, J. Schøn, W. Warta, S. W. Glunz, and M. C. Schubert, "Degradation of crystalline silicon due to boron-oxygen defects," *IEEE J. Photovoltaics*, vol. 7, no. 1, pp. 383-398, 2016.
- [53] S. W. Glunz, S. Rein, W. Warta, J. Knobloch, and W. Wettling, "Degradation of carrier lifetime in Cz silicon solar cells," *Sol. Energy Mater. Sol. Cells*, vol. 65, no. 1-4, pp. 219-229, 2001.
- [54] A. Herguth, G. Schubert, M. Kaes, and G. Hahn, "Avoiding boron-oxygen related degradation in highly boron doped Cz silicon," in *21st European Photovoltaic Solar Energy Conference (EUPVSEC)*, 2006.
- [55] J. Knobloch, S. Glunz, D. Biro, W. Warta, E. Schaffer, and W. Wettling, "Solar cells with efficiencies above 21% processed from Czochralski grown silicon," in *25th IEEE Photovoltaic Specialists Conference (PVSC)*, 1996.
- [56] H. Hashigami, Y. Itakura, and T. Saitoh, "Effect of illumination conditions on Czochralski-grown silicon solar cell degradation," *J. Appl. Phys.*, vol. 93, no. 7, pp. 4240-4245, 2003.
- [57] K. Bothe, R. Hezel, and J. Schmidt, "Recombination-enhanced formation of the metastable boron-oxygen complex in crystalline silicon," *Appl. Phys. Lett.*, vol. 83, no. 6, pp. 1125-1127, 2003.
- [58] J. Schmidt *et al.*, "Impurity-related limitations of next-generation industrial silicon solar cells," in *38th IEEE Photovoltaic Specialists Conference (PVSC)*, 2012.

- [59] J. Schmidt, A. G. Aberle, and R. Hezel, "Investigation of carrier lifetime instabilities in Cz-grown silicon," in *26th IEEE Photovoltaic Specialists Conference (PVSC)*, 1997.
- [60] B. Lim, K. Bothe, and J. Schmidt, "Deactivation of the boron–oxygen recombination center in silicon by illumination at elevated temperature," *Phys. status solidi - Rapid Res. Lett.*, vol. 2, no. 3, pp. 93-95, 2008.
- [61] A. Herguth and G. Hahn, "Kinetics of the boron-oxygen related defect in theory and experiment," *J. Appl. Phys.*, vol. 108, no. 11, p. 114509, 2010.
- [62] V. P. Markevich *et al.*, "Boron–oxygen complex responsible for light-induced degradation in silicon photovoltaic cells: A new insight into the problem," *Phys. status solidi (a)*, vol. 216, no. 17, p. 1900315, 2019.
- [63] M. Vaqueiro-Contreras *et al.*, "Identification of the mechanism responsible for the boron oxygen light induced degradation in silicon photovoltaic cells," *J. Appl. Phys.*, vol. 125, no. 18, p. 185704, 2019.
- [64] K. Ramspeck *et al.*, "Light induced degradation of rear passivated mc-Si solar cells," in *27th European Photovoltaic Solar Energy Conference and Exhibition (EUPVSEC)*, 2012.
- [65] K. Petter *et al.*, "Dependence of LeTID on brick height for different wafer suppliers with several resistivities and dopants," in *9th International Workshop on Crystalline Silicon for Solar Cells*, 2016.
- [66] G. Coletti, C. Mulder, G. Galbiati, and L. Geerligs, "Reduced effect of BO degradation on multicrystalline silicon wafers," in *21st European Photovoltaic Solar Energy Conference (EUPVSEC)*, 2006.
- [67] K. Bothe, R. Sinton, and J. Schmidt, "Fundamental boron–oxygen-related carrier lifetime limit in mono-and multicrystalline silicon," *Prog. Photovolt.: Res. Appl.*, vol. 13, no. 4, pp. 287-296, 2005.
- [68] M. Padmanabhan *et al.*, "Light-induced degradation and regeneration of multicrystalline silicon Al-BSF and PERC solar cells," *Phys. status solidi - Rapid Res. Lett.*, vol. 10, no. 12, pp. 874-881, 2016.
- [69] C. Vargas *et al.*, "Carrier-induced degradation in multicrystalline silicon: Dependence on the silicon nitride passivation layer and hydrogen released during firing," *IEEE J. Photovoltaics*, vol. 8, no. 2, pp. 413-420, 2018.
- [70] R. Eberle, W. Kwapil, F. Schindler, M. C. Schubert, and S. W. Glunz, "Impact of the firing temperature profile on light induced degradation of multicrystalline silicon," *Phys. status solidi - Rapid Res. Lett.*, vol. 10, no. 12, pp. 861-865, 2016.
- [71] D. Bredemeier, D. C. Walter, R. Heller, and J. Schmidt, "Impact of hydrogen-rich silicon nitride material properties on light-induced lifetime degradation in multicrystalline silicon," *Phys. status solidi - Rapid Res. Lett.*, vol. 13, no. 8, p. 1900201, 2019.

-
- [72] J. Schmidt, D. Bredemeier, and D. C. Walter, "On the defect physics behind light and elevated temperature-induced degradation (LeTID) of multicrystalline silicon solar cells," *IEEE J. Photovoltaics*, vol. 9, no. 6, pp. 1497-1503, 2019.
- [73] K. Krauß, A. A. Brand, F. Fertig, S. Rein, and J. Nekarda, "Fast regeneration processes to avoid light-induced degradation in multicrystalline silicon solar cells," *IEEE J. Photovoltaics*, vol. 6, no. 6, pp. 1427-1431, 2016.
- [74] D. Sperber, A. Herguth, and G. Hahn, "A 3-state defect model for light-induced degradation in boron-doped float-zone silicon," *Phys. status solidi - Rapid Res. Lett.*, vol. 11, no. 3, p. 1600408, 2017.
- [75] T. H. Fung *et al.*, "A four-state kinetic model for the carrier-induced degradation in multicrystalline silicon: Introducing the reservoir state," *Sol. Energy Mater. Sol. Cells*, vol. 184, pp. 48-56, 2018.
- [76] P. Rosenits, T. Roth, S. W. Glunz, and S. Beljakowa, "Determining the defect parameters of the deep aluminum-related defect center in silicon," *Appl. Phys. Lett.*, vol. 91, no. 12, p. 122109, 2007.
- [77] M. Binns *et al.*, "Indium-doped mono-crystalline silicon substrates exhibiting negligible lifetime degradation following light soaking," in *42nd IEEE Photovoltaic Specialists Conference (PVSC)*, 2015.
- [78] S. Glunz, S. Rein, J. Knobloch, W. Wettling, and T. Abe, "Comparison of boron- and gallium-doped p-type Czochralski silicon for photovoltaic application," *Prog. Photovolt.: Res. Appl.*, vol. 7, no. 6, pp. 463-469, 1999.
- [79] F. A. Trumbore, "Solid solubilities of impurity elements in germanium and silicon," *Bell Syst. Tech. J.*, vol. 39, no. 1, pp. 205-233, 1960.
- [80] L. Linares and S. Li, "An improved model for analyzing hole mobility and resistivity in p-type silicon doped with boron, gallium, and indium," *J. Electrochem. Soc.*, vol. 128, no. 3, p. 601, 1981.
- [81] "Gallium-doped monocrystalline silicon: The next big thing in PV?" [Online]. Available: <https://onestepoffthegrid.com.au>.
- [82] Y. Zhi *et al.*, "Ga-doped Czochralski silicon with rear p-type polysilicon passivating contact for high-efficiency p-type solar cells," *Sol. Energy Mater. Sol. Cells*, vol. 230, p. 111229, 2021.
- [83] N. E. Grant, J. R. Scowcroft, A. I. Pointon, M. Al-Amin, P. P. Altermatt, and J. D. Murphy, "Lifetime instabilities in gallium doped monocrystalline PERC silicon solar cells," *Sol. Energy Mater. Sol. Cells*, vol. 206, p. 110299, 2020.
- [84] N. E. Grant *et al.*, "Gallium-doped silicon for high-efficiency commercial passivated emitter and rear solar cells," *Solar RRL*, vol. 5, no. 4, p. 2000754, 2021.
- [85] D. Lin, Z. Hu, L. Song, D. Yang, and X. Yu, "Investigation on the light and elevated temperature induced degradation of gallium-doped Cz-Si," *Sol. Energy*, vol. 225, pp. 407-411, 2021.

-
- [86] W. Kwapil, J. Dalke, R. Post, and T. Niewelt, "Influence of dopant elements on degradation phenomena in B- and Ga-doped Czochralski-grown silicon," *Solar RRL*, vol. 5, no. 5, p. 2100147, 2021.
- [87] J. D. Murphy *et al.*, "Minority carrier lifetime in indium doped silicon for photovoltaics," *Prog. Photovolt.: Res. Appl.*, vol. 27, no. 10, pp. 844-855, 2019.
- [88] E. Cho *et al.*, "P-type indium-doped passivated emitter rear solar cells (PERC) on Czochralski silicon without light-induced degradation," *IEEE J. Photovoltaics*, vol. 6, no. 4, pp. 795-800, 2016.
- [89] J. Schmidt, K. Bothe, and R. Hezel, "Oxygen-related minority-carrier trapping centers in p-type Czochralski silicon," *Appl. Phys. Lett.*, vol. 80, no. 23, pp. 4395-4397, 2002.
- [90] R. Boyle, "FT-IR measurement of interstitial oxygen and substitutional carbon in silicon wafers," *Thermo Scientific Application Note*, vol. 50640, 2008.
- [91] A. K. S iland, "Silicon for solar cells," Norwegian University of Science and Technology, 2005.
- [92] Z. Hameiri, N. Borojevic, L. Mai, N. Nandakumar, K. Kim, and S. Winderbaum, "Low-absorbing and thermally stable industrial silicon nitride films with very low surface recombination," *IEEE J. Photovoltaics*, vol. 7, no. 4, pp. 996-1003, 2017.
- [93] U. Varshney *et al.*, "Controlling light- and elevated-temperature-induced degradation with thin film barrier layers," *IEEE J. Photovoltaics*, vol. 10, no. 1, pp. 19-27, 2019.
- [94] D. Payne *et al.*, "Acceleration and mitigation of carrier-induced degradation in p-type multi-crystalline silicon," *Phys. status solidi - Rapid Res. Lett.*, vol. 10, no. 3, pp. 237-241, 2016.
- [95] M. A. Green and M. J. Keevers, "Optical properties of intrinsic silicon at 300 K," *Prog. Photovolt.: Res. Appl.*, vol. 3, no. 3, pp. 189-192, 1995.
- [96] C. Vargas *et al.*, "Recombination parameters of lifetime-limiting carrier-induced defects in multicrystalline silicon for solar cells," *Appl. Phys. Lett.*, vol. 110, no. 9, p. 092106, 2017.
- [97] Y. Zhu and Z. Hameiri, "Review of injection dependent charge carrier lifetime spectroscopy," *Progress in Energy*, vol. 3, no. 1, p. 012001, 2021.
- [98] A. Sproul and M. Green, "Intrinsic carrier concentration and minority-carrier mobility of silicon from 77 to 300 K," *J. Appl. Phys.*, vol. 73, no. 3, pp. 1214-1225, 1993.
- [99] P. J. Cousins, D. H. Neuhaus, and J. E. Cotter, "Experimental verification of the effect of depletion-region modulation on photoconductance lifetime measurements," *J. Appl. Phys.*, vol. 95, no. 4, pp. 1854-1858, 2004.

- [100] M. Bail, M. Schulz, and R. Brendel, "Space-charge region-dominated steady-state photoconductance in low-lifetime Si wafers," *Appl. Phys. Lett.*, vol. 82, no. 5, pp. 757-759, 2003.
- [101] D. Klaassen, "A unified mobility model for device simulation—I. Model equations and concentration dependence," *Solid-State Electron.*, vol. 35, no. 7, pp. 953-959, 1992.
- [102] C. Sun, F. E. Rougieux, and D. Macdonald, "A unified approach to modelling the charge state of monatomic hydrogen and other defects in crystalline silicon," *J. Appl. Phys.*, vol. 117, no. 4, p. 045702, 2015.
- [103] K. Bothe and J. Schmidt, "Electronically activated boron-oxygen-related recombination centers in crystalline silicon," *J. Appl. Phys.*, vol. 99, no. 1, p. 013701, 2006.
- [104] V. V. Voronkov, R. J. Falster, J. Schmidt, K. Bothe, and A. Batunina, "Lifetime degradation in boron doped Czochralski silicon," *ECS Transactions*, vol. 33, no. 11, p. 103, 2010.
- [105] M. A. Green, "Intrinsic concentration, effective densities of states, and effective mass in silicon," *J. Appl. Phys.*, vol. 67, no. 6, pp. 2944-2954, 1990.
- [106] R. Couderc, M. Amara, and M. Lemiti, "Reassessment of the intrinsic carrier density temperature dependence in crystalline silicon," *J. Appl. Phys.*, vol. 115, no. 9, p. 093705, 2014.
- [107] D. H. Macdonald, "Recombination and trapping in multicrystalline silicon solar cells," Australian National University, 2001.
- [108] R. Sinton, J. Swirhun, M. Forsyth, and T. Mankad, "The effects of sub-bandgap light on QSSPC measurement of lifetime and trap density: What is the cause of trapping?," in *25th European Photovoltaic Solar Energy Conference (EUPVSEC)/5th World Conference on Photovoltaic Energy Conversion (WCPEC)*, 2010.
- [109] D. P. Joshi and D. P. Bhatt, "Theory of grain boundary recombination and carrier transport in polycrystalline silicon under optical illumination," *IEEE Trans. Electron Devices*, vol. 37, no. 1, pp. 237-249, 1990.
- [110] C. H. Seager, "Grain boundaries in polycrystalline silicon," *Annu. Rev. Mater. Sci.*, vol. 15, no. 1, pp. 271-302, 1985.
- [111] P. Gundel, M. C. Schubert, and W. Warta, "Origin of trapping in multicrystalline silicon," *J. Appl. Phys.*, vol. 104, no. 7, p. 073716, 2008.
- [112] A. Bentzen, H. Tathgar, R. Kopecek, R. Sinton, and A. Holt, "Recombination lifetime and trap density variations in multicrystalline silicon wafers through the block," in *31st IEEE Photovoltaic Specialists Conference (PVSC)*, 2005.

- [113] J. Tan, A. Cuevas, D. MacDonald, T. Trupke, R. Bardos, and K. Roth, "On the electronic improvement of multi-crystalline silicon via gettering and hydrogenation," *Prog. Photovolt.: Res. Appl.*, vol. 16, no. 2, pp. 129-134, 2008.
- [114] H. El Omari, J. Boyeaux, and A. Laugier, "Screen printed contacts formation by rapid thermal annealing in multicrystalline silicon solar cells," in *25th IEEE Photovoltaic Specialists Conference (PVSC)*, 1996.
- [115] J. F. Nijs, J. Szlufcik, J. Poortmans, S. Sivonthaman, and R. P. Mertens, "Advanced manufacturing concepts for crystalline silicon solar cells," *IEEE Trans. Electron Devices*, vol. 46, no. 10, pp. 1948-1969, 1999.
- [116] D. Chen *et al.*, "Evidence of an identical firing-activated carrier-induced defect in monocrystalline and multicrystalline silicon," *Sol. Energy Mater. Sol. Cells*, vol. 172, pp. 293-300, 2017.
- [117] T. Niewelt, F. Schindler, W. Kwapil, R. Eberle, J. Schön, and M. C. Schubert, "Understanding the light-induced degradation at elevated temperatures: Similarities between multicrystalline and floatzone p-type silicon," *Prog. Photovolt.: Res. Appl.*, vol. 26, no. 8, pp. 533-542, 2018.
- [118] H. Dekkers, L. Cernel, and G. Beaucarne, "Carrier trap passivation in multicrystalline Si solar cells by hydrogen from SiN_x:H layers," *Appl. Phys. Lett.*, vol. 89, no. 1, p. 013508, 2006.
- [119] A. Cuevas, M. Stocks, D. Macdonald, M. Kerr, and C. Samundsett, "Recombination and trapping in multicrystalline silicon," *IEEE Trans. Electron Devices*, vol. 46, no. 10, pp. 2026-2034, 1999.
- [120] M. Siriwardhana, Y. Zhu, Z. Hameiri, D. Macdonald, and F. Rougieux, "Photoconductance determination of carrier capture cross sections of slow traps in silicon through variable pulse filling," *IEEE J. Photovoltaics*, vol. 11, no. 2, pp. 273-281, 2021.
- [121] M. Kim *et al.*, "Impact of thermal processes on multi-crystalline silicon," *Frontiers in Energy*, vol. 11, no. 1, pp. 32-41, 2017.
- [122] B. J. Hallam *et al.*, "Advanced hydrogenation of dislocation clusters and boron-oxygen defects in silicon solar cells," *Energy Procedia*, vol. 77, pp. 799-809, 2015.
- [123] M. A. Jensen, A. E. Morishige, J. Hofstetter, D. B. Needleman, and T. Buonassisi, "Evolution of LeTID defects in p-type multicrystalline silicon during degradation and regeneration," *IEEE J. Photovoltaics*, vol. 7, no. 4, pp. 980-987, 2017.
- [124] C. Vargas, G. Coletti, C. Chan, D. Payne, and Z. Hameiri, "On the impact of dark annealing and room temperature illumination on p-type multicrystalline silicon wafers," *Sol. Energy Mater. Sol. Cells*, vol. 189, pp. 166-174, 2019.
- [125] S. A. McHugo *et al.*, "Nanometer-scale metal precipitates in multicrystalline silicon solar cells," *J. Appl. Phys.*, vol. 89, no. 8, pp. 4282-4288, 2001.

- [126] I. Guerrero *et al.*, “About the origin of low wafer performance and crystal defect generation on seed-cast growth of industrial mono-like silicon ingots,” *Prog. Photovolt.: Res. Appl.*, vol. 22, no. 8, pp. 923-932, 2014.
- [127] A. J. Schwartz, M. Kumar, B. L. Adams, and D. P. Field, *Electron backscatter diffraction in materials science*. Springer, 2009.
- [128] J. Hylton, A. Burgers, and W. Sinke, “Alkaline etching for reflectance reduction in multicrystalline silicon solar cells,” *J. Electrochem. Soc.*, vol. 151, no. 6, p. G408, 2004.
- [129] H. Sio, Z. Xiong, T. Trupke, and D. Macdonald, “Imaging crystal orientations in multicrystalline silicon wafers via photoluminescence,” *Appl. Phys. Lett.*, vol. 101, no. 8, p. 082102, 2012.
- [130] T. Buonassisi, A. Istratov, M. Pickett, M. Marcus, T. Cizek, and E. Weber, “Metal precipitation at grain boundaries in silicon: Dependence on grain boundary character and dislocation decoration,” *Appl. Phys. Lett.*, vol. 89, no. 4, p. 042102, 2006.
- [131] M. Winter, D. C. Walter, and J. Schmidt, “Carrier lifetime degradation and regeneration in gallium-and boron-doped monocrystalline silicon materials,” *IEEE J. Photovoltaics*, vol. 11, no. 4, pp. 866-872, 2021.
- [132] W. Kwapil, J. Dalke, T. Niewelt, and M. C. Schubert, “LeTID-and (extended) BO-related degradation and regeneration in B-and Ga-doped monocrystalline silicon during dark and illuminated anneals,” in *37th European Photovoltaic Solar Energy Conference and Exhibition (EUPVSEC)*, 2020.
- [133] T. Mchedlidze and J. Weber, “Location and properties of carrier traps in mc-Si solar cells subjected to degradation at elevated temperatures,” *Phys. status solidi (a)*, vol. 216, no. 17, p. 1900142, 2019.
- [134] M. Binns *et al.*, “Indium-doped mono-crystalline silicon substrates exhibiting negligible lifetime degradation following light soaking,” in *42nd IEEE Photovoltaic Specialists Conference (PVSC)*, 2015.
- [135] J. A. T. De Guzman *et al.*, “Indium-doped silicon for solar cells—light-induced degradation and deep-level traps,” *Phys. status solidi (a)*, p. 2100108, 2021.
- [136] D. Bredemeier, D. Walter, and J. Schmidt, “Light-induced lifetime degradation in high-performance multicrystalline silicon: Detailed kinetics of the defect activation,” *Sol. Energy Mater. Sol. Cells*, vol. 173, pp. 2-5, 2017.
- [137] K. Graff, *Metal impurities in silicon-device fabrication*. Springer Science & Business Media, 2013.
- [138] B. Paudyal, K. McIntosh, and D. Macdonald, “Temperature dependent carrier lifetime studies on Ti-doped multicrystalline silicon,” *J. Appl. Phys.*, vol. 105, no. 12, p. 124510, 2009.

- [139] S. Boughaba and D. Mathiot, "Deep level transient spectroscopy characterization of tungsten-related deep levels in silicon," *J. Appl. Phys.*, vol. 69, no. 1, pp. 278-283, 1991.
- [140] J. Schmidt *et al.*, "Impurity-related limitations of next-generation industrial silicon solar cells," in *38th IEEE Photovoltaic Specialists Conference (PVSC)*, 2012.
- [141] D. Kane and R. Swanson, "Measurement of the emitter saturation current by a contactless photoconductivity decay method," in *18th IEEE Photovoltaic Specialists Conference (PVSC)*, 1985.
- [142] F. M. Schuurmans, "Surface passivation of silicon by PECVD silicon nitride," Utrecht University, 1998.
- [143] S. Rein and S. Glunz, "Electronic properties of the metastable defect in boron-doped Czochralski silicon: Unambiguous determination by advanced lifetime spectroscopy," *Appl. Phys. Lett.*, vol. 82, no. 7, pp. 1054-1056, 2003.
- [144] S. Diez, S. Rein, T. Roth, and S. Glunz, "Cobalt related defect levels in silicon analyzed by temperature-and injection-dependent lifetime spectroscopy," *J. Appl. Phys.*, vol. 101, no. 3, p. 033710, 2007.
- [145] S. Bernardini, T. U. N erland, A. L. Blum, G. Coletti, and M. I. Bertoni, "Unraveling bulk defects in high-quality c-Si material via TIDLS," *Prog. Photovolt.: Res. Appl.*, vol. 25, no. 3, pp. 209-217, 2017.
- [146] Y. Zhu *et al.*, "Electrical characterization of thermally activated defects in n-type float-zone silicon," *IEEE J. Photovoltaics*, vol. 11, no. 1, pp. 26-35, 2020.
- [147] R. A. Sinton, A. Cuevas, and M. Stuckings, "Quasi-steady-state photoconductance, a new method for solar cell material and device characterization," in *25th IEEE Photovoltaic Specialists Conference (PVSC)*, 1996.
- [148] R. Dumbrell, M. K. Juhl, T. Trupke, and Z. Hameiri, "Extracting metal contact recombination parameters from effective lifetime data," *IEEE J. Photovoltaics*, vol. 8, no. 6, pp. 1413-1420, 2018.
- [149] J. Giesecke, B. Michl, F. Schindler, M. Schubert, and W. Warta, "Minority carrier lifetime of silicon solar cells from quasi-steady-state photoluminescence," *Sol. Energy Mater. Sol. Cells*, vol. 95, no. 7, pp. 1979-1982, 2011.
- [150] R. A. Sinton and A. Cuevas, "A quasi-steady-state open-circuit voltage method for solar cell characterization," in *16th European Photovoltaic Solar Energy Conference (EUPVSEC)*, 2000.
- [151] A. C. Killam, J. F. Karas, A. Augusto, and S. G. Bowden, "Monitoring of photovoltaic system performance using outdoor Suns-Voc," *Joule*, vol. 5, no. 1, pp. 210-227, 2021.

- [152] A. H. T. Le *et al.*, “Temperature-dependent performance of silicon solar cells with polysilicon passivating contacts,” *Sol. Energy Mater. Sol. Cells*, vol. 225, p. 111020, 2021.
- [153] S. T. Søndergaard, J. O. Odden, and R. Strandberg, “Temperature dependent Suns-Voc of multicrystalline silicon solar cells from different ingot positions,” in *7th World Conference on Photovoltaic Energy Conversion (WCPEC)(A Joint Conference of 45th IEEE PVSC, 28th PVSEC & 34th EU PVSEC)*, 2018.
- [154] N. Nampalli *et al.*, “Multiple pathways for permanent deactivation of boron-oxygen defects in p-type silicon,” *Sol. Energy Mater. Sol. Cells*, vol. 173, pp. 12-17, 2017.
- [155] R. Dumbrell, M. K. Juhl, T. Trupke, and Z. Hameiri, “Comparison of terminal and implied open-circuit voltage measurements,” *IEEE J. Photovoltaics*, vol. 7, no. 5, pp. 1376-1383, 2017.
- [156] M. A. Green, “Solar cell minority carrier lifetime using open-circuit voltage decay,” *Solar cells*, vol. 11, no. 2, pp. 147-161, 1984.
- [157] F. W. Chen, J. E. Cotter, M. D. Abbott, T.-T. A. Li, and K. C. Fisher, “The influence of parasitic effects on injection-level-dependent lifetime data,” *IEEE Trans. Electron Devices*, vol. 54, no. 11, pp. 2960-2968, 2007.
- [158] F. Feldmann, M. Bivour, C. Reichel, M. Hermle, and S. W. Glunz, “Passivated rear contacts for high-efficiency n-type si solar cells providing high interface passivation quality and excellent transport characteristics,” *Sol. Energy Mater. Sol. Cells*, vol. 120, pp. 270-274, 2014.
- [159] S. De Wolf, A. Descoedres, Z. C. Holman, and C. Ballif, “High-efficiency silicon heterojunction solar cells: A review,” *green*, vol. 2, no. 1, pp. 7-24, 2012.
- [160] Y. Buratti, Q. T. Le Gia, J. Dick, Y. Zhu, and Z. Hameiri, “Extracting bulk defect parameters in silicon wafers using machine learning models,” *Npj Comput. Mater.*, vol. 6, no. 1, pp. 1-8, 2020.